MAGNETIC FIELDS IN ISOLATED NEUTRON STARS

from the interior to the exterior

ANKAN SUR

DOCTORAL THESIS

Magnetic fields in isolated neutron stars:
from the interior to the exterior

Author:
Ankan SUR

Supervisor:
dr. hab. Brynmor HASKELL

A thesis submitted in fulfillment of the requirements
for the degree of Doctor of Philosophy in Physical Sciences (Astronomy)

Astrophysics division II
Nicolaus Copernicus Astronomical Center, Warsaw, Poland

March 2022

Abstract

of the thesis entitled

Magnetic fields in isolated neutron stars:
from the interior to the exterior

in English

Neutron stars are natural laboratories that allow us to study many phenomena under extreme conditions. These compact objects are characterized by strong magnetic fields with non-trivial origins and evolution. It is important to understand the field properties when interpreting observational data. We are able to probe parameters of electro-dynamical processes at scales unavailable in terrestrial laboratories through observations of diverse types of neutron stars. A long-standing challenge is to understand the properties of neutron stars' internal magnetic fields which are poorly constrained by observations at present. Assaying the stability of a given magnetic field geometry is therefore an important step in determining whether the geometry will be stable over multiple Alfven timescales, thus constituting a viable description of neutron star interiors. The simple cases, such as the purely poloidal or purely toroidal fields, have so far been meticulously analyzed through perturbation theory and, most recently, by means of non-linear magnetohydrodynamic simulations. This thesis investigates the different configurations of magnetic fields using both magnetohydrodynamic and general relativistic magnetohydrodynamic simulations and studies the distribution of magnetic energy into poloidal and toroidal components. Our results show that the final configuration, known as the "twisted-torus," has a toroidal field that is 10-20 % of the total magnetic field energy, and is threaded by poloidal field-lines extending into the outer atmosphere. However, our simulations do not consider the effect of the crystalline solid crust that forms when the protoneutron star cools down. In such a scenario, the crust evolves to Hall equilibrium states while the core is composed of superconducting protons, and magnetic equilibria can be determined from solutions of the Grad-Shafranov equation involving two arbitrary functions of the poloidal flux. The equilibria found by using the simple, but physically sound, choices of these functions with adjustable parameters present only a small fraction of the magnetic energy stored in the toroidal component (5%). Identifying these barotropic equilibria points the way to understanding their stability and studying their properties. The evolution of the magnetic field plays a significant role in different emission processes such as flares from magnetars, radio jets, and gravitational waves. In light of the fact that we need extremely strong magnetic fields inside a neutron star to cause significant deformation and produce gravitational waves, we suggest that a newly born magnetar can form columns of matter at the magnetic poles from fallback accretion which may emit detectable gravitational waves. Additionally, the study provides us with information about the survival time ($\sim$ 50s) before the NS collapses to a black hole through the fallback accretion channel.

Abstract in Polish

Gwiazdy neutronowe są naturalnymi laboratoriami, które pozwalają badać wiele zjawisk w ekstremalnych warunkach. Te zwarte obiekty charakteryzują się silnymi polami magnetycznymi o nietrywialnym pochodzeniu i ewolucji. Zrozumienie własności pola magnetycznego jest ważne przy interpretacji danych obserwacyjnych. Dzięki obserwacjom różnych typów gwiazd neutronowych jesteśmy w stanie badać parametry procesów elektrodynamicznych w skalach niedostępnych w laboratoriach naziemnych. Długoletnim wyzwaniem jest zrozumienie własności wewnętrznych pól magnetycznych gwiazd neutronowych, które obecnie są słabo ograniczone przez obserwacje. Ocena stabilności danej geometrii pola magnetycznego jest zatem ważnym krokiem w określeniu, czy geometria ta będzie stabilna w wielu skalach czasowych Alfvena, stanowiąc tym samym realny opis wnętrza gwiazd neutronowych. Proste przypadki, takie jak pola czysto poloidalne lub czysto toroidalne, były do tej pory drobiazgowo analizowane za pomocą teorii perturbacji, a ostatnio za pomocą nieliniowych symulacji magnetohydrodynamicznych. W niniejszej pracy badamy różne konfiguracje pól magnetycznych, stosując symulacje magnetohydrodynamiczne i ogólną relatywistyczną symulację magnetohydrodynamiczną, oraz analizujemy rozkład energii magnetycznej na składową poloidalną i toroidalną. Nasze wyniki pokazują, że ostateczna konfiguracja, znana jako "skręcony torus", ma pole toroidalne, które stanowi 10-20% całkowitej energii pola magnetycznego i jest poprzecinane liniami pól poloidalnych rozciągających się do zewnętrznej atmosfery. Nasze symulacje nie uwzględniają jednak wpływu krystalicznej skorupy stałej, która tworzy się podczas stygnięcia gwiazdy protoneutronowej. W takim scenariuszu skorupa ewoluuje do stanów równowagi Halla, podczas gdy jądro składa się z nadprzewodzących protonów, a równowagi magnetyczne można wyznaczyć z rozwiązań równania Grada-Shafranova obejmującego dwie dowolne funkcje strumienia poloidalnego. Równowagi znalezione za pomocą prostych, ale fizycznie uzasadnionych, wyborów tych funkcji z regulowanymi parametrami prezentują tylko niewielki ułamek energii magnetycznej zmagazynowanej w składowej toroidalnej (5%). Identyfikacja tych równań barotropowych wskazuje drogę do zrozumienia ich stabilności i badania ich własności. Ewolucja pola magnetycznego odgrywa istotną rolę w różnych procesach emisyjnych, takich jak rozbłyski magnetarów, dżety radiowe i fale grawitacyjne. W świetle faktu, że do wywołania znaczącej deformacji i wytworzenia fal grawitacyjnych we wnętrzu gwiazdy neutronowej potrzebne są niezwykle silne pola magnetyczne, sugerujemy, że nowo narodzony magnetar może tworzyć kolumny materii na biegunach magnetycznych w wyniku akrecji zwrotnej, które mogą emitować wykrywalne fale grawitacyjne. Dodatkowo, badania dostarczają nam informacji o czasie przeżycia (50s) zanim NS zapadnie się do czarnej dziury przez awaryjny kanał akrecyjny.

Magnetic fields in isolated neutron stars: from the interior to the exterior

by

Ankan SUR

B.S. *Calcutta University*, M.S. *University of Amsterdam*

Supervisor: **dr. hab. Brynmor HASKELL**

A Thesis Submitted in Partial Fulfilment
of the Requirements for the Degree of
Doctor of Philosophy

at

Nicolaus Copernicus Astronomical Center of the Polish Academy of Sciences
March 2022

Declaration

I, Ankan Sur, declare that this thesis, titled, "Magnetic fields in isolated neutron stars: from the interior to the exterior", which is submitted in fulfillment of the requirements for the Degree of Doctor of Philosophy, represents my own work, except where due acknowledgement have been made. Also, I declare that it has not been included in any thesis, dissertation, or report previously submitted to this University or to any other institution for a degree, diploma, or other qualification.

Signed: _____

Date: _____ March 2022 _____

Dedicated to
My parents Ruby Sur and Debabrata Sur
for their endless love, support, and encouragement,
and
My Teachers
who have inspired me.

Acknowledgements

It is my pleasure to first thank my supervisor, Prof. Brynmor Haskell, whose guidance and mentoring have helped me gain not only an understanding of astrophysics, but also how to handle stressful situations, and to make decisions throughout my PhD. Thanks to his supportive approach and constant guidance, we were able to explore interesting problems and publish articles in reputed journals. He gave me the freedom to think about my own problems, but also showed me which ones could be solved effectively. He encouraged me to participate in international conferences and academic visits. I found that these opportunities not only allowed me to interact with leading scientists in the world, but also to present my work and get feedback.

My thanks go to Dr. Marco Antonelli, Dr. Danai Antonopoulou, Dr. Giovanni Camelio, Lorenzo Gavassino, Dr. Samuel Lander, and Dr. Jonas Pereira for all the discussions, for solving numerical issues related to my simulations, and for holding group meetings. It has definitely made my work progress faster and prevented delays. Thanks to Dr. Miljenko Cemeljic for having the patience to teach me PLUTO and discuss many code-related issues with me.

I would like to thank my friends Saikruba Krishnan, Ruchi Mishra, Dr. Samaresh Mondal, Rajeev Singh Rathour, Tathagata Saha, and Chandra Shekhar Saraf with whom I lived in the CAMK hotel. Cooking dinner together, watching movies, gossiping endlessly, playing cards, pool, badminton, chess, jenga, science talks, career talks, and many more activities have truly given me a joyous experience. I couldn't have asked for better friends. Also thanks to Abinash Adhikari, Suhani Gupta, Ayush Moharana, Dr. Ishika Palit, and my seniors Dr. Deepika Bollimpalli and Dr. Swayamtrupta Panda for bringing us such wonderful days at CAMK.

As a predoctoral fellow at the Flatiron Institute, I spent 5 months in New York City. I am immensely grateful to my mentors Dr. Yajie Yuan and Dr. Sasha Philippov for inspiring me and giving me the opportunity to work on an interesting project. My visit to the United States was an invaluable opportunity that helped me grow as a scientist. I would like to thank the Simons Foundation for supporting me.

Finally, I want to thank my parents for believing in me and supporting me in every possible way. Without their blessings, I would not have achieved what I have today.

Ankan SUR

March 2022

List of Publications

JOURNALS:

[1] **Ankan Sur**, Brynmor Haskell, and Emily Kuhn, "Magnetic field configurations in neutron stars from MHD simulations," *Monthly Notices of the Royal Astronomical Society*, June 2020, Volume 495, Issue 1, pp.1360-1371.

[2] **Ankan Sur**, William Cook, David Radice, Brynmor Haskell, and Sebastiano Bernuzzi, "Long-term GRMHD simulations of magnetic field in isolated neutron stars," *Monthly Notices of the Royal Astronomical Society*, February 2022.

[3] **Ankan Sur**, and Brynmor Haskell, "The impact of superconductivity and the Hall effect in models of magnetised neutron stars," *Publications of the Astronomical Society of Australia*, Volume 38, article id. e043, September 2021.

[4] **Ankan Sur**, and Brynmor Haskell, "Gravitational waves from mountains in newly born millisecond magnetars" *Monthly Notices of the Royal Astronomical Society*, Volume 502, Issue 4, pp.4680-4688, April 2021

Contents

List of Figures

List of Abbreviations and Constants

BBH	**B**inary **B**lack **H**ole
BNS	**B**inary **N**eutron **S**tar
CCO	**C**entral **C**ompact **O**bjects
CCSne	**C**ore **C**ollapsed **S**upernovae
ET	**E**instein **T**elescope
EOS	**E**quation **o**f **S**tate
GS	**G**rad- **S**hafranov
GRMHD	**G**eneral **R**elativistic **M**agneto**H**ydro**D**ynamics
GWs	**G**ravitational **W**aves
HMXB	**H**igh **M**ass **X**-ray **B**inary
LIGO	**L**aser **I**nterferometer **G**ravitational-wave **O**bservatory
LMXB	**L**ow **M**ass **X**-ray **B**inary
MHD	**M**agneto**H**ydro**D**ynamics
MSP	**M**illi **S**econd **P**ulsars
NS(s)	**N**eutron **S**tar(s)
NICER	**N**eutron **S**tar **I**nterior **C**omposition **E**xplorer
PA	**P**osition **A**ngle
PP	**P**iecewise **P**olytrope
PNS	**P**roto **N**eutron **S**tar
PSR	Pulsar
RVM	**R**otating **V**ector **M**odel
SNR	**S**ignal-to-**N**oise **R**atio
TOV	**T**olman **O**ppenheimer **V**olkoff
c	3×10^{8} cm s^{-1} (Speed of light)
G	6.67×10^{-8} cm^{3}g^{-1}s^{-2} (Gravitation constant)

k_B	1.3807×10^{-16} ergK^{-1} (Boltzmann constant)
1 kpc	3.086×10^{19} m
m_e	9.1094×10^{-28} g (Mass of the electron)
m_p	1.6726×10^{-24} g (Mass of the proton)
m_n	1.674×10^{-24} g (Mass of the neutron)
$M_\odot$	1.9891×10^{33} g (Solar mass)
ρ_{ND}	4×10^{11} gm cm^{-3} (Neutron drip density)

Neutron stars: An Introduction

"Not only is the Universe stranger than we think, it is stranger than we can think."
-Werner Heisenberg.

1.1   Historical background

Astronomers have always been very interested in the fate of stars since nuclear physics was developed. When a massive star with a total mass greater than 8 $M_\odot$ but less than 25 $M_\odot$ [Heg+03], where $M_\odot$ is the mass of the Sun, runs out of nuclear fuel, it dies in a type-II supernova explosion, leaving behind a core where neutron degeneracy pressure balances gravity. This object, first predicted theoretically by Landau in 1932 and later by Baade and Zwicky in 1934, was proposed to be very compact and gravitationally bound compared to other stars. The loss of neutrinos during the supernova explosion process causes electrons and protons to combine, creating a neutron-rich core and warming the stellar interior. Initially, the star's core temperature reaches 50 MeV, but after approximately 50 seconds, the temperature begins to decrease as the neutrinos escape. This leaves behind what is today known as a Neutron Star (NS). In general, a massive star with mass in the range 25-100 $M_\odot$ would typically become a black hole, however a NS may be created from such higher masses if the metallicity of the star exceeds the solar metallicity [ST86; HPY07]. It was not until Jocelyn Bell Burnell discovered radio pulsars in 1969 that NSs were confirmed to exist despite being theoretically predicted 35 years prior. By 1967, Pacini had already thought that the Crab Nebula was powered by a rotating NS; however, the detection of radio pulses from CP 1919 revealed it to be driven by a strongly magnetized NS, finally confirming its discovery.

1.2   Classification

A majority of NSs are observed as *pulsars*, which are objects rotating rapidly and emitting coherent radio waves. Pulsars have spin periods ranging from milliseconds to seconds and have surface magnetic field strengths from $B_s \sim 10^8 - 10^{12}$ G. If the spin axis is out of alignment with the magnetic axis, charged particles are accelerated along the magnetic poles, causing pulses of light that are swept around as the star rotates, just like the beams from a lighthouse. These pulses are so precise, that pulsars can be comparable to atomic clocks. The magnetic field in NSs can also amplify and make them become magnetic monsters, which are young and have field strengths million times stronger than ordinary pulsars. These objects are called *magnetars* [DT92; TD93], where the magnetic field lines under the crust are so intense that even a tiny movement releases bursts of electromagnetic radiation [TD95]. In addition to isolated NSs, there are many that exist as binary systems as survivors of supernova explosions and those that have been associated with dense stellar environments like globular clusters through the capture of a companion star. Some NSs are also not observed to pulse, for example, some are seen only in thermal emission and modelling indicates they are NSs [Cac+08; PCC19], and some Low Mass X-ray Binaries (LMXBs) have bursts that suggest a surface (and thus cannot be black holes). The period of these burst oscillations gives the spin period of the NS [in'+02; Bha+05].
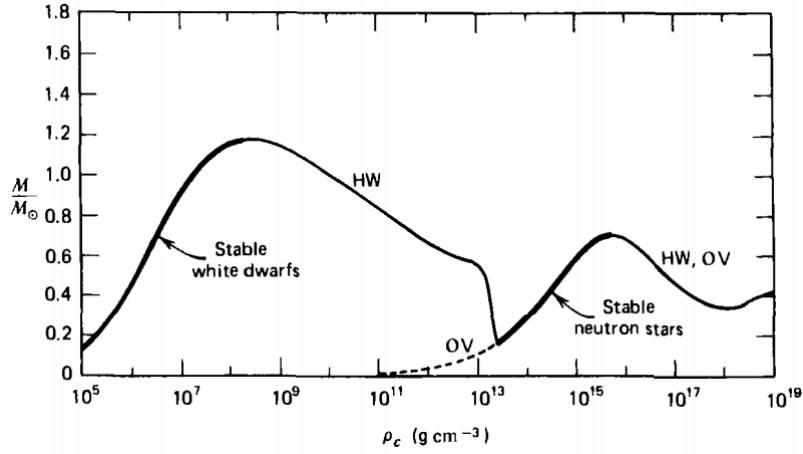
Figure 1.1: Schematic diagram showing the turning points in the mass versus central density diagram for equilibrium configurations of ideal gas equation of state. The stable branch for white dwarfs and neutron stars are marked. Figure taken from openmetric.org.

1.3 Structure of neutron stars

The stellar structure equation for hydrostatic equilibrium describes how the gravitational pressure on a system can be compared with the degeneracy pressure on a static cold Fermi gas. Oppenheimer and Volkoff (OV) were the first to perform stellar structure calculations in General Relativity on NSs in 1939, using the assumption that matter was composed of neutron gas at high density in hydrostatic equilibrium. Richard Tolman analysed the spherically symmetric metric

$$ds^2 = e^{2\phi(r)}dt^2 + e^{2\Lambda(r)}dr^2 + r^2(d\theta^2 + \sin^2\theta d\phi^2) \tag{1.1}$$

where $\phi, \Lambda \to 0$ for $r \to \infty$. These unknown functions in the metric can be found by solving the Einstein equations

$$G^{\alpha\beta} = 8\pi G T^{\alpha\beta} \tag{1.2}$$

Using the stress energy tensor for the perfect fluid,

$$T^{\alpha\beta} = (\rho + p)u^\alpha u^\beta + pg^{\alpha\beta} \tag{1.3}$$

the stellar structure equations in General Relativity (also called the Tolman Oppenheimer Volkoff (TOV) equations) are given by

$$\frac{dP}{dr} = -\frac{G\rho(r)m(r)}{r^2} \frac{\left[1 + \frac{P(r)}{\rho(r)c^2}\right]\left[1 + \frac{4\pi r^3 P(r)}{m(r)c^2}\right]}{\left[1 - \frac{2Gm(r)}{rc^2}\right]} \tag{1.4}$$

$$\frac{dm(r)}{dr} = 4\pi\rho(r)r^2 \tag{1.5}$$

where P, m and ρ are the pressure, mass and density respectively at a distance r from the center. The integration is carried from the $r = 0$ to $r = R$ with the boundary conditions $p(R) = 0$ and $M(R) = M$, where M is the total mass of the star. The TOV equations, given by equation 1.5, are analogues to the Lane-Emden equation which is simply the Newtonian version of the hydrostatic equilibrium condition. Solving these equations with an ideal gas equation of state (EOS) composed of free neutrons, resulted in equilibrium configurations shown in figure 1.1 where the model with maximum mass has the parameters $M_{\mathrm{max}} = 0.7M_\odot$, $R = 9.6$ km, and a central density $\rho_c = 5 \times 10^{15}$ gm cm^{-3}.

Based on the interactions between baryons, hyperons, and quarks, there have been realistic calculations that account for numerous EOSs with different masses and radii. EOSs can also be classified based on their compressibility into soft, moderate, and stiff EOSs, each having a different maximum mass, such as $\sim 1.4M_\odot$ for soft, and $\sim 2.5M_\odot$ for stiff. Figure 1.2 shows how different EOSs based on different interactions produce different maximum masses of the NS.

The maximum mass of NSs have been calculated from observations. For example, the Hulse-Taylor binary pulsar is a well-known system which gives a measurement of $M_{\mathrm{NS}} = 1.44M_\odot$. Clearly, this exceeds the TOV limit of $0.7\,M_\odot$(which considers the ideal gas of free interacting neutrons) suggesting that strong interactions play a significant role in the internal structure of NSs. Similarly, the observation of gravitational waves from the binary neutron star merger GW170817 have put the maximum mass of NSs in the range $2.01\,M_\odot \leq M \leq 2.17\,M_\odot$ [MM17; RMW18]. Furthermore, and most recently, millisecond pulsars have been studied using Shapiro delay to set the TOV limit to approximately $2.14M_\odot$ [Cro+20].

Let us now proceed to a more detailed discussion of the internal structure of NSs, which is depicted in figure 1.3. Broadly, we can classify the different regions as following:

- **Atmosphere**: This thin layer (few millimeters thick) of low density plasma is mostly responsible for the electromagnetic spectrum we observe, and allows us to collect information about chemical composition, surface temperature, surface gravity, and surface magnetic field.
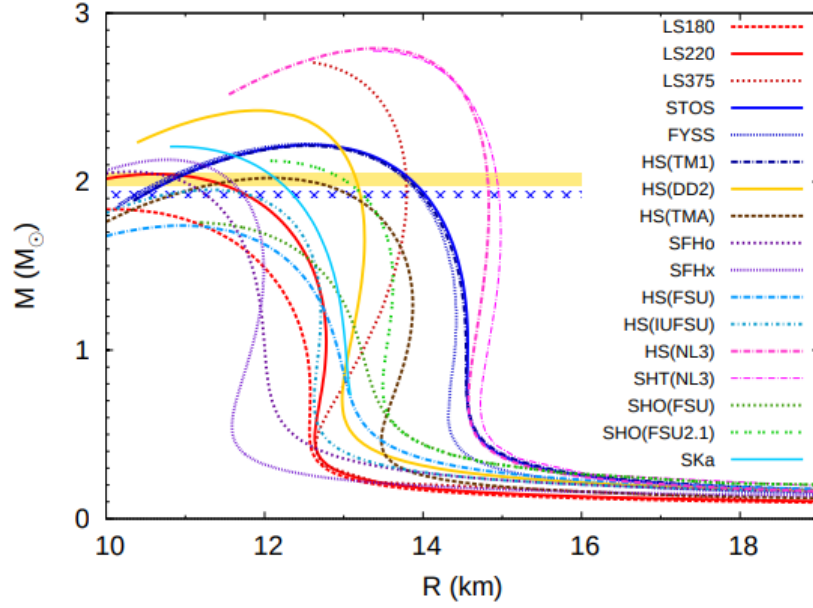
Figure 1.2: Relationships between mass and radius for spherically symmetric NSs covering the full thermodynamic parameter range and including only nucleonic degrees of freedom given in Table III in [Oer+17]. Two horizontal bars show two recent precise NS mass determinations [Dem+10] (hatched blue) and [Ant+13] (yellow). Figure taken from [Oer+17].

- **Outer Crust**: This region has a thickness of few hundred metres with densities varying from $\rho \sim 10^6 \, \mathrm{gm \, cm^{-3}}$ to the neutron-drip density $\rho_{ND} = 4 \times 10^{11} \, \mathrm{gm \, cm^{-3}}$. Matter is composed of degenerate and ultrarelativistic electrons and ions which form a solid crystal. The neutronization process make the nuclei neutron-rich with increasing density. The neutrons start tto drip out of the nuclei to form a neutron gas at the neutron drip density at the bottom of the outer crust.

- **Inner Crust**: This layer is about a km thick and its density varies from $4 \times 10^{11} \, \mathrm{gm \, cm^{-3}}$ to $0.5\rho_0 \sim 1.4 \times 10^{14} \, \mathrm{gm \, cm^{-3}}$, where ρ_0 is the nuclear saturation density. The chemical composition comprises atomic nuclei, electrons and superfluid neutrons.

- **Outer core**: This region extends up to 2 km with densities ranging from $0.5\rho_0 \leq \rho \leq 2\rho_0$. The matter is primarily composed of electrons, protons, neutrons, and possibly muons. The neutrons and protons interact strongly and behave as a superfluid.

- **Inner core**: More than half of the star is contained within this region where densities are well above $\rho \geq 2\rho_0$. Modeling the inner core is challenging as exotic states of matter can exist whose interactions are unknown. Pions, kaons, hyperons as well as quark matter may exist along with new phases of matter favored by first and second-order phase transitions. The EOS of the inner core remains mysterious.
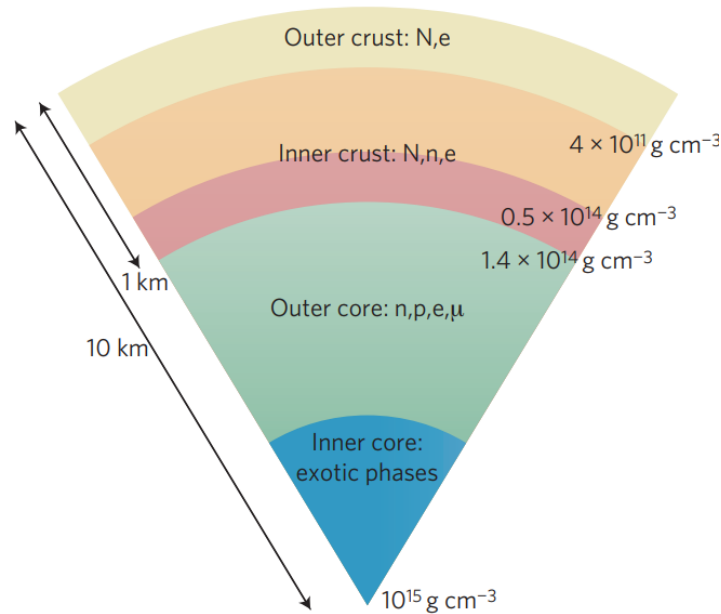
Figure 1.3: The structure of a neutron star showing the compositions at different layers and variations in density as one moves from the outer crust to the inner core. Figure from [New13].

1.3.1   Superfluidity and superconductivity

Initially, a proto-neutron star (PNS) is extremely hot, with an internal temperature of the order of 10^{12} K [HPY07]. About one minute later, the PNS becomes transparent to neutrinos being produced in its interior which carry away energy, and thus rapidly cools down. As the star cools below about a billion degrees, the outer layers of the star crystallize into a solid crust. The star's core is much cooler than its crust at this point due to the escaping neutrinos. It takes several decades, but the interior of the star reaches an equilibrium temperature of about a hundred million degrees (apart from a thin outer layer). After approximately a hundred thousand years, the last cooling stage occurs, as heat from the interior is distributed to the surface, dissipating as radiation. Metallic surfaces, which are made up mostly of iron, are generally surrounded by a thin atmosphere. But below the surface, the matter has been compressed so much that atomic nuclei, which form a regular Coulomb lattice, are fully ionized, and thus co-exist with a quantum gas of electrons. Neutrons start to leak out of nuclei as they move deeper into the star, creating an underground neutron ocean. Unlike the outer crust, whose composition is almost completely determined by atomic masses, the inner crust, where neutrons are unbound, can only be studied theoretically since there is no equivalent on Earth. NSs remain poorly understood in terms of their composition and properties of the core.

Prior to the actual observations of pulsars, it was proposed in 1959 that NSs might contain a neutron superfluid – an anomalous frictionless liquid. Strong short scale repulsive interactions

between fermions provides the necessary pressure to balance the weak attraction. Superfluids (electrically neutral) and superconductors (electrically charged) are expected to form in the interior of a mature NS [Leg08]. At low enough temperatures, nucleons can form pairs of bosons. These bosons can behave coherently on a large scale and the nucleon condensate can flow without viscosity, just like superfluid helium-3. Partial wave analysis of nuclear interactions is a useful tool for understanding patterns of pairing in NSs. Neutron-neutron and proton-proton pairings are caused by S and P wave scattering, while $^3D_2$ wave scattering can only exist between neutrons and protons. There are believed to be three types of superfluids and superconductors within a NS: (i) S wave superfluid permeating the inner region of the crust, (ii) a homogeneous neutron superfluid in the outer core, and (iii) a P wave superfluid along with proton (S wave) superconductor in the core [BPP69]. Like the emergence of these phenomena in terrestrial experiments, neutron superfluidity and proton superconductivity can profoundly alter its dynamics. As the standard reactions and scattering processes suppress the bulk and shear viscosity, superfluid neutrons can flow more freely relative to the 'normal' component of the star [HS18]. Such a phenomena can give rise to mutual friction and freeze the rotation of the star giving rise to pulsar 'glitches' [HM15].

1.4 Magnetic fields in neutron stars

1.4.1 Magnetic field from observations

Magnetic fields in NSs are responsible for a plethora of activities, from flares on the surface to gamma-ray bursts and fast radio bursts. Observation of the Zeeman splitting of spectral lines or measurements of polarization can measure the magnetic fields of non degenerate stars, such as the Sun, and some white dwarfs. In addition, Doppler imaging analysis can reveal cold spots associated with the strongest magnetized regions of the surface by analyzing the time-varying profiles of rotating stars. Such direct measurements are difficult to obtain for a NS and one thus has to rely on more indirect measurements. In some cases, X-ray spectra reveal cyclotron lines, from which one can estimate the magnetic field at their surfaces. In general, NSs have a magnetic field that is primarily characterized by a loss of rotational energy due to the electromagnetic torque which causes them to spin-down. This allows us to estimate the large-scale dipolar magnetic field based on rotational properties. One can infer magnetic field intensities from period and derivatives of period. If we can assume that the exterior magnetic field, to its lowest order, to be approximately a dipole, we can write

$$B = \frac{3n^i(n_j m^j) - m^i}{r^3} \tag{1.6}$$

where $n^i = x^i/r$ and m is the dipole moment. The higher order multipoles fall of as $1/r^{l+2}$ and hence we can intuitively conclude that far off from the stellar surface, the field is mostly dipolar.

The dipole can be presented in terms of the surface poloidal field

$$m = \frac{1}{2} B_s R^3 (e_{||} \cos \alpha + e_{\perp} \sin \alpha \sin(\omega t) + e_{\perp} \sin \alpha \cos(\omega t)) \tag{1.7}$$

where $e_{||}$ and $e_{\perp}$ are the unit vectors parallel and perpendicular to the rotation axis, while α is the angle between m and rotation axis. B_s represents the surface magnetic field strength. The energy carried away by electromagnetic waves:

$$\frac{dE}{dt} = -\frac{2}{3c^3} |\ddot{m}| \tag{1.8}$$

which gives

$$\frac{dE}{dt} = -\frac{1}{6c^3} B_s^3 R^6 \sin^2 \alpha \, \omega^4 \tag{1.9}$$

and if one equals this to the decrease in rotational energy $I\omega\dot{\omega}$ where I is the moment of inertia and ω is the angular frequency, we have

$$\dot{\omega} = -\frac{1}{6c^3} \frac{B_s^2 R^6}{I} \sin^2 \alpha \omega^3 \tag{1.10}$$

There is no spin down when the magnetic axis and rotation axis are aligned. The above calculations are based on considering the dipole in vacuum, however, in reality the NS is surrounded by plasma where charged particles are accelerated along the magnetic field lines and produce the observed emission. In this case, the electromagnetic torque acting on the pulsar is given by [Spi06]

$$\tau_{EM} = \frac{B_s^2 R^6 \omega^3}{c^3} (1 + \sin^2 \alpha) \tag{1.11}$$

By measuring period and period derivative and using the above expressions we can estimate the field strength at the surface. For typical pulsar parameters, the magnetic field strength is given by

$$B_s = 3 \times 10^{11} \sqrt{\frac{P}{10} \frac{\dot{P}}{10^{-14}}} \, G \tag{1.12}$$

1.4.2   The $P - \dot{P}$ diagram and characteristic age

A standard pulsar has a field of the order of $B_s \sim 10^{12}$ G, but accreting systems have weaker inferred fields of the order of $B_s \sim 10^8$ G , and magnetars have fields of the order of $B_s \sim 10^{15}$ G, which are necessary to generate their high energy emission, which is too energetic to be
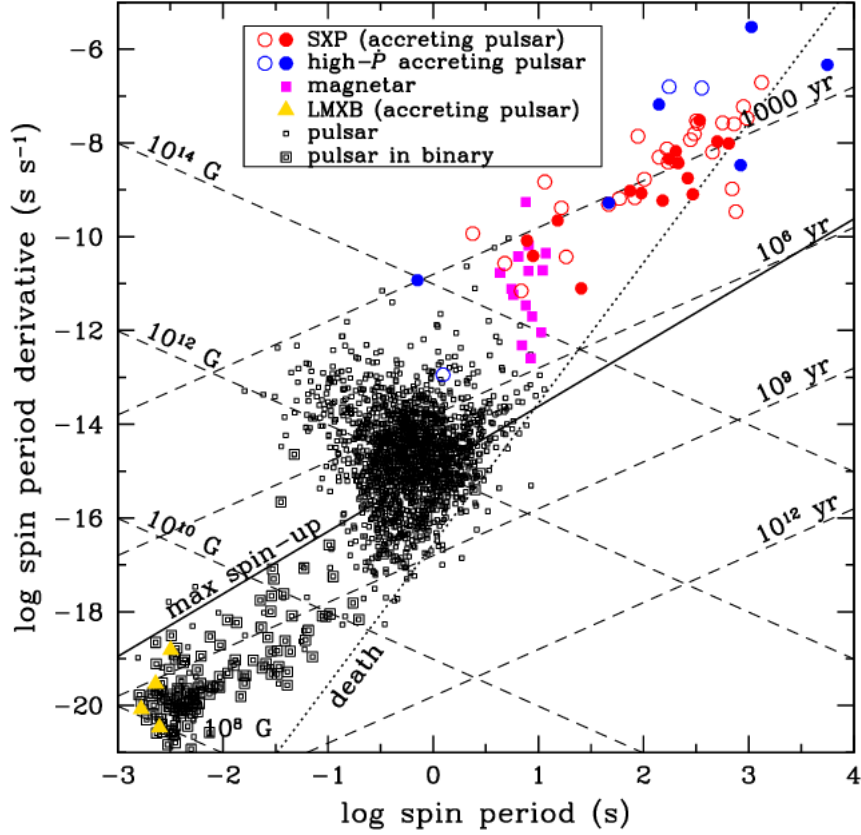
Figure 1.4: Pulsar spin period (P) versus time derivative of spin-period ($\dot{P}$). Open squares are pulsar values from the ATNF Pulsar Catalogue [Man+05], while solid squares denote magnetars. Accreting sources that have $\dot{P} < 0$ are denoted by open circles while closed circles denote $\dot{P} > 0$. Figure taken from [Ho+14]

.

produced by rotation alone. Based on a constant magnetic field, we can integrate equation 1.10 to get an estimate of the age of the pulsar, the so-called characteristic age. Thus, rewriting equation 1.10 in terms of the period, we have

$$\dot{P} = \frac{8\pi^2 R^6 B^2 \sin^2 \alpha}{3c^3 I} P^{-1} \tag{1.13}$$

Assuming the star to be rapidly rotating at its birth, we can assume $P(t = 0) \ll P(t)$. Integrating equation 1.13, characteristic age (τ_c) is given by

$$\tau_c = \frac{P}{2\dot{P}} \tag{1.14}$$

This is only a rough estimate of the age. The magnetic field strength, age, spin, and spin-down rate are well represented in the $P - \dot{P}$ diagram shown in figure 1.4. The young and strongly magnetised NSs (and also magnetars) are located on the top right hand corner while old weakly

magnetised stars are in the bottom left. It is generally believed that the star starts out highly magnetised and spinning rapidly, and spins down due to electromagnetic emission, while the field decays due to Hall dissipation in the crust, as we will discuss later, and then on a slower timescale due to resistive effects in the core. Millisecond pulsars (located at the bottom left corner in the $P - \dot{P}$ diagram) are thought to be old pulsars that are recycled from the graveyard (where the field and rotation rate are too low for radio emission to occur) by accretion [Bv91]. Another important parameter is the braking index (n) defined as:

$$\dot{\nu} \propto \nu^n = C\nu^n \tag{1.15}$$

where C is a constant of proportionality and $\nu = \omega/2\pi$ is the spin frequency. The braking index can be obtained if the second derivative of the spin frequency is measured which eliminates the constant C from equation 1.15. Thus,

$$n = \frac{\nu\ddot{\nu}}{\dot{\nu}} \tag{1.16}$$

As we noted before, if the dipolar radiation is solely responsible for spindown (see equation 1.9), the spin frequency of the pulsar varies as $\dot{\nu} \propto \nu^3$ (see also equation 1.10). Reliably measured braking indices lie in the range $1.4 < n < 3$ [Lyn+96; Lyn+15; Arc+16] and can be used to investigate alternative spin-down mechanisms, e.g. winds ($n = 1$) or gravitational-wave emission ($n = 5$ for a quadrupolar 'mountain'), and make more sophisticated estimates of pulsar ages and initial spin periods.

1.4.3 Magnetic field geometry and NICER observations

For rotating NSs, observational and theoretical evidence supports the presence of higher-order multipole moments at the stellar surface [Jon80; GMG03; Aru+18], though the multipole component is expected to be much weaker than its dipole component higher up in the magnetosphere (i.e. at larger radii). This is because the dipole falls off as $1/r^3$ while all higher multipoles of moment $l \geq 2$ falls off as $1/r^{(l+2)}$. Generalizations in the form of distorted or offset dipoles have also been explored both for pair production [Aro98; HM01] and for modeling thermal pulsations from recycled pulsars [Bog13]. The pulsar magnetopshere contains regions with narrow gaps where the plasma is not present. In these regions, the unscreened electric field accelerates charged particles which then produce electron-positron pairs. These gaps are either present above the polar caps or near the light cylinder close to the current sheets. Particles streaming outward produce the observed radio, γ-ray, and non-thermal X-rays. As opposing charged particles are accelerated downward, they hit the NS polar caps and heat the surface. Radiation from the heated spots causes X-ray pulsations as the star rotates. It is not only the temperature profile across the hot regions that determines how the pulsations look (the pulse profile) but also the properties of the NS atmosphere. A detailed model of X-ray spectral-timing data from NICER was carried out by [Ril+19] for the millisecond pulsar PSR J0030+0451 based on pulse-profile

measurements. A canonical global-scale centered dipolar magnetic field configuration cannot explain the location, shape, and size of these hot regions. Using these results, [Bil+19] explored previous attempts to constrain the magnetospheric configuration of PSR J0030+0451. There was no direct observational evidence that PSR J0030+0451 has a centered dipole field, but the results required development of nondipolar (or offset-dipolar) magnetic field configurations for rotation-driven pulsars and including them in existing models of pair cascade production, magnetospheric current distribution, and surface heating. Global non-dipolar (or offset-dipolar) magnetic field configurations may have a profound impact on many aspects of pulsar research, including pulsar braking, birth velocities, detectability, and interpretation of multiwavelength magnetospheric emission. NICER was also successful in constraining the dense matter equation of state from mass-radius relation for PSR J0740+6620. By combining information from multimessenger observations such as radio timing, GW events, and mass-radius estimate of PSR J0030+0451 [Mil+19], the radius of a $1.4 \, M_\odot$ NS was constrained to 95% credible ranges $12.33^{+0.76}_{-0.81}$ km (using Piecewise Polytropic (PP) EOS model) and $12.18^{+0.56}_{-0.79}$ km (speed of sound EOS model) [Raa+21]. See [Mil+19] for similar conclusions. NICER is also expected to measure radius by doing precise pulse profile modelling (to measure GR corrections) in the coming future.

1.4.4 Magnetic field from theory

The origin of magnetic field in NSs still remain a mystery. The presence of high magnetic field strengths can be explained by the conservation of magnetic flux from the progenitor star. For example, let us consider a star with typical magnetic field strength $B_i = 10^2$ G (solar value) and radius $R_i = 10^6$ km, and it ends up being a NS with radius $R_f = 10$ km. According to conservation of magnetic flux, we have

$$B_i R_i^2 = B_f R_f^2 \tag{1.17}$$

the final magnetic field of the NS can be estimated to be:

$$B_f = \frac{B_i R_i^2}{R_f^2} = 10^2 \left(\frac{10^6}{10} \right)^2 G \sim 10^{12} \, G \tag{1.18}$$

We can therefore reach such high magnetic field strengths, but this calculation isn't capable of explaining much higher magnetic field strengths (e.g. $B_s \sim 10^{15}$ G as seen in magnetars). It is generally thought that some kind of a dynamo operates in the PNS phase.

A NS's magnetic configuration is theorized using magnetohydrodynamical equilibrium calculations. However, these solutions are not unique and it is unclear whether they are stable, and therefore the magnetic field configuration is an open question. The long-term magnetic evolution is another important aspect. The magnetic field in the solid crust evolves as a result

of Ohmic dissipation and Hall drift. During the first few days after birth, protons in the core of NSs transition to a type II superconducting state, when a magnetic field is confined to flux tubes and is no longer locked to the plasma. Understanding the dynamics of flux tubes, coupled to the motion of superfluid neutron vortices, is an extremely challenging problem that makes the magnetic field evolution in the core formally difficult to face [Gra+15; GAS11; GA11].

1.4.5 Magnetohydrodynamics (MHD)

To understand the magnetic field evolution in NSs, we must solve Maxwell's equations in the highly conducting stellar interior given by

$$\text{Gauss' Law} \qquad \nabla \cdot \vec{E} = \frac{\rho}{\varepsilon_0} \tag{1.19a}$$

$$\text{Gauss' Law (} \vec{B} \text{ Fields)} \qquad \nabla \cdot \vec{B} = 0 \tag{1.19b}$$

$$\text{Faraday's Law} \qquad \nabla \times \vec{E} = -\frac{\partial \vec{B}}{\partial t} \tag{1.19c}$$

$$\text{Ampere's Law} \qquad \nabla \times \vec{B} = \mu_0 \vec{J} + \mu\varepsilon \frac{\partial \vec{E}}{\partial t} \tag{1.19d}$$

where $\vec{J}$ is the current and the force acting on the particle is called the Lorentz force given by

$$\vec{F} = q\vec{E} + \frac{\vec{J} \times \vec{B}}{c} \tag{1.20}$$

To describe the complete evolution, we must also look at the evolution of the fluid. Since there is no external source of matter flow, the mass of the fluid remains constant within the volume *V* of the star. Thus, conservation of mass gives

$$\frac{\partial \rho}{\partial t} + \nabla \cdot (\rho \vec{v}) = 0 \tag{1.21}$$

We focus here on inviscid flow since extending to a viscous fluid can be accomplished similarly as in ordinary fluid mechanics. Next, we move on to obtain the equation of motion of the fluid whose total linear momentum must be conserved. Considering the Lorentz force, pressure (*p*) force, and the force of gravity, the conservation of momentum equation gives the time evolution of the fluid's velocity (also known as the Euler equation) as:

$$\frac{\partial \vec{v}}{\partial t} + \vec{v} \cdot \nabla \vec{v} + \frac{1}{4\pi\rho} \vec{B} \times (\nabla \times \vec{B}) + \frac{1}{\rho} \nabla p = -\nabla \Phi_g \tag{1.22}$$

where Φ_g is the gravitational potential. Let us now look into the evolution of the magnetic field. We first consider the Ohm's law

$$\vec{J} = \sigma\left(E + \frac{\vec{v} \times \vec{B}}{c}\right) \tag{1.23}$$

Neglecting the Electric field, we can use equation 1.23 in equation 1.20 which gives

$$\vec{F} = -\frac{\vec{B} \times (\nabla \times \vec{B})}{4\pi} \tag{1.24}$$

From equation 1.23, the electric field can be written

$$\vec{E} = \frac{\vec{J}}{\sigma} - \frac{\vec{v}}{c} \times \vec{B} = \frac{\eta}{c}\nabla \times \vec{B} - \frac{\vec{v}}{c} \times \vec{B} \tag{1.25}$$

Therefore, using equation 1.25 in Ampere's law gives us the so called *induction* equation:

$$\frac{\partial \vec{B}}{\partial t} = \nabla \times \left(\vec{v} \times \vec{B}\right) - \nabla \times \left(\eta \nabla \times \vec{B}\right) \tag{1.26}$$

And, lastly the pressure can be obtained using the sound speed c_s as:

$$\frac{\partial p}{\partial t} + \vec{v} \cdot \nabla p + \rho c_s^2 \nabla \vec{v} = 0, \tag{1.27}$$

Thus, the MHD equations, which are essentially a reduction of fluid mechanics equations with Maxwell's equations, are 1.21, 1.22, 1.26, 1.27. MHD is a strongly reduced theory as compared to plasma physics where the plasma is electrically neutral. Another important thing to note in MHD is that the electric field vanishes only in the frame of reference in which the fluid is moving; it is therefore present in all other frames. If we boost to the frame moving with velocity v we have

$$\vec{E}' = \vec{E} + \frac{\vec{v}}{c} \times \vec{B} \tag{1.28}$$

From the conservation of magnetic flux,

$$\frac{\partial \Psi_m}{\partial t} = \int_S \vec{B} \cdot d\vec{S} = 0 \tag{1.29}$$

$$\frac{\partial \Psi_m}{\partial t} = \int_S \frac{\partial \vec{B}}{\partial t} + \oint_C \vec{B} \cdot \vec{v}d\vec{l} = \oint_C (-c\vec{E} - \vec{v} \times \vec{B})d\vec{l} = \oint_C \vec{E}'d\vec{l} = 0 \tag{1.30}$$

$$\tag{1.31}$$

Given $\vec{J} = \sigma\vec{E}'$, we have $\vec{E}' \to 0$ when the conductivity $\sigma \to \infty$.

1.4.6   General Relativistic Magnetohydrodynamics (GRMHD)

There are several aspects of NS structure and evolution that General Relativity affects, including radiation from the surface, magnetic field models, and evolution of compact binaries. It is widely used for mass measurements of NS and to study properties of superdense matter. Consequently, we must model our NS based on GRMHD simulations.

Many authors, for example [Kom05; KSK99; GMT03; Ant+06] have adopted a conservative scheme to integrate the GRMHD equations. These equations are of the form:

$$\partial_t \mathbf{U}(\mathbf{P}) = -\partial_i \mathbf{F}(\mathbf{P}) + \mathbf{S}(\mathbf{P}) \tag{1.32}$$

where $\mathbf{U}$ is a vector of conserved variables (such as energy, momentum, and particle number density), $\mathbf{F}^i$ are the fluxes, and $\mathbf{S}$ is a vector of source terms. $\mathbf{P}$ is a vector of "primitive" variables such as rest-mass density, velocity and magnetic components, and internal energy density.

In GR, the fluid is described by its four velocity u^μ, rest-mass density ρ, internal energy per unit volume $\in_{\text{int}}$, and pressure p. The normal observer's four-velocity is given by $n_\mu = (-\alpha, 0, 0, 0,)$ in the coordinate basis with metric components $g_{\mu\nu}$ and independent variables t, x_1, x_2, x_3. α is known as the lapse function such that $\alpha^2 = -1/g_{tt}$. The electromagnetic field tensor $F^{\mu\nu}$ has six components (three electric field and three magnetic field), however, the ideal MHD condition eliminates 3 of them by:

$$u_\mu F^{\mu\nu} = 0 \tag{1.33}$$

because the Lorentz force vanishes in the rest-frame of the fluid. The magnetic field four-vector is more convenient to describe the field which is given by

$$\mathcal{B}^\mu = -n_\nu{}^* F^{\mu\nu} \tag{1.34}$$

where $^*F^{\mu\nu}$ is the antisymmetric field tensor. The magnetic field variables are given by

$$B^i = \frac{\mathcal{B}^i}{\alpha} \tag{1.35}$$

The governing equations for the GRMHD are conservation of stress-energy (1.36), conservation of particle number (1.37) , and the Maxwell equations ((1.38), given by:

$$\nabla_\mu T^\mu_\nu = 0 \tag{1.36}$$

$$\nabla_\mu (\rho u^\mu) = 0 \tag{1.37}$$

$$\nabla_\nu {}^*F^{\mu\nu} = 0 \tag{1.38}$$

1.5 Magnetic equilibria

The fluid can be approximated as the sum of the non-magnetised background plus a perturbation, i.e. density $\rho \sim \rho_0 + \delta\rho$, and pressure $P \sim P_0 + \delta P$, wehere $|\delta\rho|/\rho_0 \sim |\delta P|/P_0 \sim B^2/(8\pi P_0) \leq 10^{-6}$ [Rei14]. Chandrasekhar & Fermi [CF53] had showed that magnetized stars are not spherically symmetric. The perturbed quantities satisfy the hydromagnetic equilibrium

$$\nabla \delta P + \delta\rho \nabla \Phi_g = \frac{1}{c} \vec{J} \times \vec{B} \tag{1.39}$$

Assuming the star to be a perfectly conducting fluid in ideal MHD, the dynamical equilibrium of the fluid can also be written in terms of the fluid pressure, mass density, magnetic field, and currents. Thus, in addition to equation 1.39, we also have:

$$\nabla P + \rho \nabla \Phi_g = \frac{1}{c} \vec{J} \times \vec{B} \tag{1.40}$$

In axial symmetry, the magnetic field can be decomposed into poloidal and toroidal components as

$$\vec{B} = B_p + B_t = \nabla \alpha(r,\theta) \times \nabla \phi + \beta(r,\theta) \nabla \phi \tag{1.41}$$

where α and β are arbitrary functions known as the poloidal and toroidal flux functions respectively, and $\nabla \phi = \hat{\phi}/r$. Therefore, the perturbed quantities will only be a function of (r,θ), implying that the azimuthal component in equation 1.39 must be zero. This gives us

$$\frac{\nabla \alpha \times \nabla \beta}{4\pi r^2 \sin^2 \theta} = 0 \tag{1.42}$$

This implies that the quantities $\nabla \alpha$ and $\nabla \beta$ are parallel to each other [Cha56]. The azimuthal component of the current ($\frac{c}{4\pi} \nabla \times B_p$) itself is given by

$$\vec{J}_\phi = -\frac{c}{4\pi} \frac{\Delta^\star \alpha}{r} \tag{1.43}$$

where

$$\Delta^\star = \frac{\partial^2}{\partial r^2} + \frac{\sin\theta}{r^2}\frac{\partial}{\partial\theta}\left(\frac{1}{\sin\theta}\frac{\partial}{\partial\theta}\right) \tag{1.44}$$

is known as the *Grad-Shafranov* operator. The Lorentz force can be written in terms of the poloidal and toroidal field as

$$\frac{\vec{J}\times\vec{B}}{c} = -\frac{1}{r^2\sin^2\theta}\left[\frac{\Delta^2\alpha}{4\pi}\nabla\alpha + \beta\nabla\beta - ((\nabla\beta\times\nabla\alpha)\cdot\hat{\phi})\hat{\phi}\right] \tag{1.45}$$

Axial symmetry implies that $\nabla\beta\times\nabla\alpha = 0$. Using this in equation 1.45a long with the static Euler equation 1.22, we get

$$\left[\frac{\Delta^\star\alpha}{4\pi}\nabla\alpha + \beta\nabla\beta\right] = -r^2\sin^2\theta\rho\nabla\chi \tag{1.46}$$

where $\nabla\chi = \vec{J}\times\vec{B}/c\rho$ is an arbitrary function of α. Therefore, the equilibrium equation of the magnetic field also known as the *Grad-Shafranov* equation is given by

$$\Delta^\star\alpha = -4\pi\beta\frac{d\beta}{d\alpha} - 4\pi r^2\sin^2\theta\rho\frac{d\chi}{d\alpha} \tag{1.47}$$

Note that we can also derive the Grad-Shafranov using the unperturbed equation 1.40. Using Ampere's law, the current density can be written as:

$$\frac{4\pi}{c}\vec{J} = \nabla\beta\times\nabla\phi - \Delta^\star\alpha\nabla\phi \tag{1.48}$$

Calculating the Lorentz force term ($\vec{J}\times\vec{B}$) and approximating the fluid to be barotropic (such that the Lorentz force can be expressed in terms of a gradient of a scalar potential), we can similarly arrive at equation 1.47.

1.5.1   Dissipation in the crust

Modeling the magnetic field evolution in the crust had gained significant interest within the NS community since the first estimate of its decay was performed by [BPP69]. However, a complete theoretical model that would explain all the observations coherently does not exist. It is generally agreed that the magnetic field in magnetars decays on timescales of $10^3 - 10^5$ years [WT06; HL06]. Such a decay can effectively heat an isolated NS [Pon+07], thus measuring the surface temperatures can give us information about the magnetic field strength. Additionally, evidence of braking indexes significantly larger than 3, which are inferred for an ensemble of a dozen pulsars in an active age of a few 10^5 years, indicates that relatively young NSs may experience periods of rapid decay [JG99; GR02].

Conversely, population synthesis studies indicate that old pulsars show no significant magnetic field decay over their lifetimes, i.e. the decay period is longer than 10 Myr [Har+97]. By assuming that the large-scale dipolar field and spin down are maintained by two current systems, these contradictory facts can be satisfactorily resolved. Long-lived currents are responsible for sustaining the large-scale dipolar field and spin down of old pulsars. Fields anchored in the crust decay between 10^5 and 10^7 years, depending on conductivity, thickness, and strength and structure of the original field. According to estimates of how fast a core-anchored field would dissipate in the crust, it would take over 100 Myr for a field to be expelled and dissipated [KG01].

Aside from the Ohmic diffusion, which occurs rapidly in low-density crustal regions and during the early hot phase of the life of a NS, another process that changes the crustal field structure, both quantitatively and qualitatively, is the Hall drift. Numerous studies have been conducted over the past two decades [Rei+07; WH09; PG10; KK12; Gou+13; GC14a; Mar+14; GP19; GDI22] on the effects of Hall drift on the evolution of magnetic fields in isolated NSs. As a result of the density profile, Hall currents are capable of forming current sheets, which are places of very efficient dissipation. In the case of current sheets just below the surface, the effect is dramatic, but even when the drift is directed towards the highly conductive inner crust, the small scale of the locally intense field results in a significantly faster dissipation of magnetic energy than the purely Ohmic diffusion estimate. Goldreich and Reisenegger [GR92] developed the theory of the Hall cascade for NSs, according to which magnetic energy is transferred from the largest to smallest scales until a critical scale length is reached below which Ohmic decay takes place. However, there seem to exist equilibrium states called "Hall equilibria" which do not modify the magnetic field configuration.

In the crystalline crust of NS, the full evolution of the magnetic field is given by the induction equation

$$\frac{\partial \vec{B}}{\partial t} = -\nabla \times \left(\frac{c}{4\pi n_e} [\nabla \times \vec{B}] \times \vec{B} \right) - \nabla \times \left(\eta \nabla \times \vec{B} \right) \tag{1.49}$$

where the first term corresponds to the Hall effect and the second is the Ohmic dissipation term on the right hand side. The quantities n_e and η are the electron density and electrical resistivity respectively. The relative importance of these two effects depend on the timescale at which these processes operate:
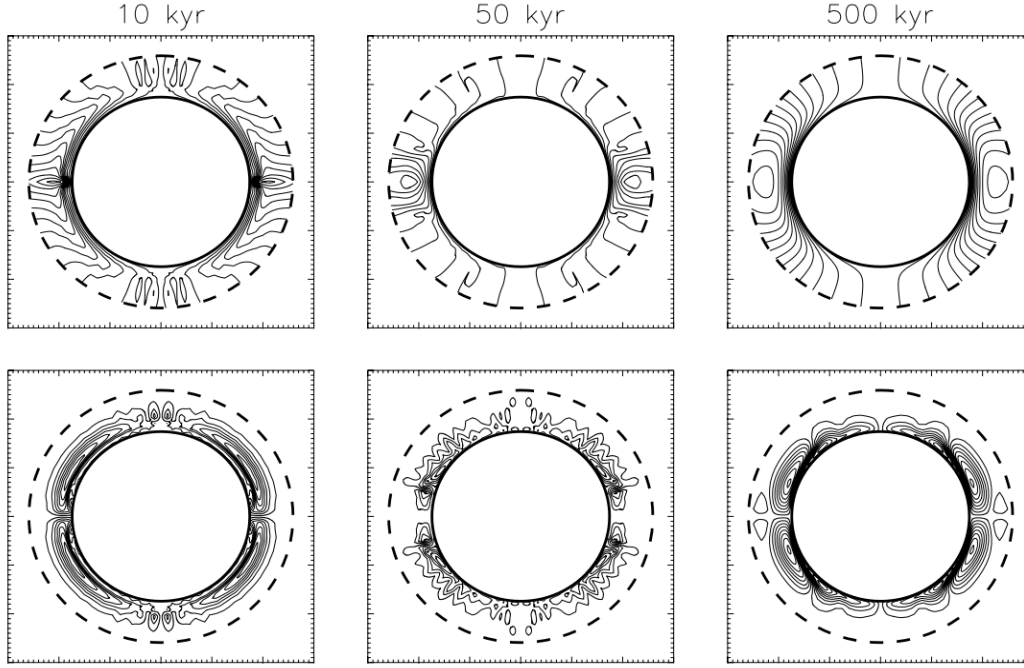
Figure 1.5: (top) Poloidal magnetic field lines in the crust at three different evolutionary stages (t = 10, 50, and 500 kyr as marked in the title of the individual frames) with Hall drift. (bottom) contours of constant toroidal mangetic field lines in the crust. Figure taken from [PG07]

$$t_{\text{Ohm}} \sim \frac{4\pi\sigma L^2}{c^2} = 13.5\,\text{Myr}\left(\frac{L}{1\text{km}}\right)^2\left(\frac{\sigma}{10^{24}\,\text{s}^{-1}}\right) \tag{1.50}$$

$$t_{\text{Hall}} \sim \frac{4\pi e L^2 n_e}{cB} = 1.6\,\text{Myr}\left(\frac{L}{1\text{km}}\right)^2\left(\frac{n_e}{2.5\times 10^{36}\text{cm}^{-3}}\right)\left(\frac{10^{14}\,G}{B}\right) \tag{1.51}$$

For $B \geq 10^{13}$ G, the Hall timescale is shorter and the evolution of the field is dominated by the Hall effect while the Ohmic dissipation mostly occurs in current sheets. There have been a number of studies exploring these effects in different contexts but we highlight some of the major findings. First, the Ohmic dissipation can cause the magnetic field to decay by a factor of $10^3 - 10^4$ for NSs in binaries due to heating effects caused by accretion. The internal temperatures also increase with accretion rate and its distribution may be non-uniform leading to thermomagnetic effects [GU94]. In all cases, varying the accretion rate or crustal temperature results in an initial rapid decay, followed by a slow decay which finally freezes, and explains many observations [KB97; KB99]. The concept of Hall equilibrium was extended to a state called the "Hall attractor" [GC14b] which consists of a dipole and an octupole component accompanied by an energetically negligible quadrupole toroidal component in an initially dominated dipolar field. This was also observed for long-term evolution of the 2 dimensional field which

underwent damped oscillations at Ohmic timescales [Mar+14].

1.6 Emission signatures : connecting theory to observations

Astronomical measurements are not numerous and precise enough for direct observation of the evolution of magnetic fields in NSs. Furthermore, the computed poloidal dipolar magnetic field B_p depends on the same quantities as characteristic age. Nonetheless, observations of energy release (bursts or constant activity), spin parameters, and properties of surface emission support the theory of field decay and its evolution. Furthermore, one can study different objects and its associated phenomena such as magnetar bursts, Central Compact Objects, radio pulsars with growing external field, High Mass X-ray binaries, millisecond radio pulsars, etc, for understanding the magnetic field dynamics [IPH21]. Our discussion will be focused on two main characteristics of magnetic field effects in NSs:

1.6.1 Gravitational waves

Gravitational waves (GWs) are the disturbances in spacetime travelling at the speed of light like a wave first predicted by Albert Einstein as part of his theory of General Relativity. Most recently, the discovery of GWs from binary systems has revolutionized our understanding of the universe since its announcement, for example, it has helped constrain the Hubble constant [Abb+21a; Abb+17a], the population of binary black holes and NSs [Abb+21d], test of General Relativity [Abb+21h], kilonova and short gamma-ray bursts [Abb+17b; CVF21], heavy metals, etc. However, with the current sensitivity of the Advanced LIGO and Advanced Virgo, we have not yet detected GWs from isolated NSs which are expected to emit long-lived monochromatic continuous waves, but have put constraints on their deformation from upper limits on the GW strain [Abb+21b; Abb+21c; Abb+21e; Abb+22; Abb+21g; Abb+21f], which would have been detected.

$$\epsilon \approx 4.5 \times 10^{-7} \left(\frac{B_p}{10^{14}\text{G}} \right) \left(1 - \frac{0.389}{\Lambda} \right) \tag{1.52}$$

A detailed discussion of the different ways a rotating NS can emit GWs is given in [Las15], but the simplest way is to form a "mountain" sustained by shear stresses. As the star rotates, it possesses a time-varying quadrupole which allows GWs to be emitted at twice the stellar frequency. Let us therefore describe the kind of signal that a deformed NS would emit. Denoting the principle moments of inertia by I_x, I_y, I_z along the axes x, y, z respectively, any asymmetric mass distribution in the NS structure will imply $I_x \neq I_y$. The rotation matrix used in transforming the moments of inertia from the lab frame to the rotating frame of the star is given
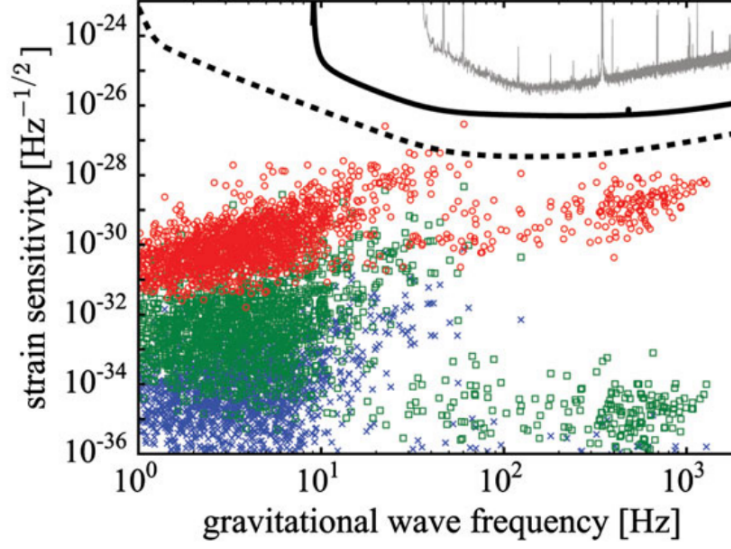
Figure 1.6: GW strain for the population of pulsars: blue crosses have $\Lambda = 1$; green crosses have $\Lambda = 0.01$; red circles assume NSs with colour-flavour-locked phase having $\Lambda = 0.1$. The definition of Λ is given by equation 1.52 which represents the fraction of poloidal energy to the total magnetic energy. The solid line represents the detector sensitivity for the Advanced LIGO while the dashed line is for the Einstein Telescope. Figure taken from [Las15].

by

$$R_z = \begin{pmatrix} \cos\phi & \sin\phi & 0 \\ -\sin\phi & \cos\phi & 0 \\ 0 & 0 & 0 \end{pmatrix} \tag{1.53}$$

In the inertial frame, we have $I_{\text{inertial}} = R_z^T I_{\text{body}} R_z$. Thus,

$$I_{xx} = -I_{yy} = \frac{1}{2}(I_x - I_y)\cos 2\phi \, I_{xy} = I_{yx} = \frac{1}{2}(I_x - I_y)\sin 2\phi \tag{1.54}$$

With the proper time derivates, we get the luminosity of the GWs as

$$\frac{dE}{dt} = \frac{G}{5c^5}\langle \dddot{I}_{xx}^2 + \dddot{I}_{xx}^2 + \dddot{I}_{xx}^2 \rangle = \frac{32G}{5c^5}(I_x - I_y)^2 \omega^6 \tag{1.55}$$

For a triaxial ellipsoid, the deformation, in general, is quantified by the ellipticity parameter defined as

$$\epsilon = \frac{|I_x - I_y|}{I_z} \tag{1.56}$$

and the gravitational wave strain for typical NS parameters is given by [SB19]

$$h_0 = \frac{4\pi^2 G}{c^4} \frac{I_z f_{GW}^2 \epsilon}{d} = 4.2 \times 10^{-26} \left(\frac{\epsilon}{10^{-6}}\right) \left(\frac{P}{10\text{ms}}\right)^2 \left(\frac{d}{1\text{kpc}}\right)^{-1}$$

(1.57)

Deformations can also be sustained by elastic strains in the crust [Bil98; UCB00], and strong magnetic fields in the core of the star [BG96]. In the latter case, the ellipticity scalse with the square of its volume-averaged magnetic field [Has+08], implying the characteristic GW strain also scales as $h_0 \sim \langle B \rangle^2$. Therefore, we must not only have a thorough understanding of the different configurations of magnetic field which can exist within a NS, but also focus on what can be inferred about the magnetic field from GW observations. As we will see in chapters 1 and 2, a purely poloidal field is unstable (and for that matter a purely toridal field as well), but the long term stability of the magnetic field is a challenging problem. The most accepted model is that of the *twisted-torus* configuration in which the toroidal component threads the closed field region of the poloidal field [BS06; CFG10; Akg+13]. These solutions can either lead to an axisymmetric field [Bra07; Bra09] or a non-axisymmetric structure [Bra08; Las+11; Cio+11; CR12]. There is uncertainty in GW predictions due to the possibility of different magnetic field configurations. The relative strengths of poloidal and toroidal components strongly affect stellar ellipticity, which is important for GW detection [Has+08; Cio+09; Mas+11]. The standard models suggest (e.g. [Mas+11]):

where Λ is the ratio of the poloidal field strength to the total magnetic field strength. Therefore, a detection is only possible for magnetar type field strengths. These objects also have spin periods from $P \sim 1 - 10$ s that would emit GWs at frequencies lower than the current sensitivities of the Advanced LIGO and Advanced Virgo detectors (see figure 1.6) but could be interesting for future observatories like the Einstein Telescope.

1.7 Outline of this thesis

The plan of the thesis is as following:

- **Chapter 2**: We performed MHD simulations of an isolated NS starting from two initial magnetic conditions: one purely poloidal field, and the other a mixed poloidal-toroidal field with a stronger toroidal component. The system was evolved for 40 ms to determine what the poloidal and toroidal energies settled to. The instability and its relation to turbulence, as well as the transfer of magnetic helicity at various length scales are discussed. We also report the effect of resistivity on our simulations.

- **Chapter 3**: In the continuation of simulations presented in chapter 1, we have performed the longest GRMHD simulations for the isolated NS, starting with the same initial conditions, but with an increased simulation box to have a maximum resolution of 512^3 in Cartesian coordinates. After evolving the system for 880 ms, we studied the long-term behavior of poloidal and toroidal energies, dissipation of magnetic energy, and calculated energy spectra.

- **Chapter 4**: In this chapter, we obtain equilibrium solutions to the magnetic field present in a standard pulsar population with a superconducting core and crust in Hall equilibrium. Additionally, we investigate MHD equilibrium in the entire star, by solving the Grad-Shafranov equation, for which a new numerical scheme based on the Gauss-Seidel method is implemented with linearising the source term. We also calculated the deformation due to the toroidal field inside the star.

- **Chapter 5**: We show how a newly born millisecond magnetar born after core-collapse supernova or a binary neutron star mereger, forms columns of matter from fallback accretion, enabling them to possess large ellipticities, and emit GWs. During this period, we also study the evolution of the NS's spin and calculate the maximum mass of the NS before it collapses into a black hole.

- **Chapter 6**: Conclusions and future work related to the main subject matter of this thesis are discussed.

Magnetic field configurations of neutron stars from MHD simulations

"Truth is ever to be found in the simplicity, and not in the multiplicity and confusion of things"

-Issac Newton.

Magnetic field configurations in neutron stars from MHD simulations

Ankan Sur [1][★] Brynmor Haskell[1] and Emily Kuhn[2]

[1]*Nicolaus Copernicus Astronomical Center, Polish Academy of Sciences, Bartycka 18, PL-00-716 Warsaw, Poland*
[2]*Department of Physics, Yale University, New Haven, CT 06520, USA*

ABSTRACT

We have studied numerically the evolution of magnetic fields in barotropic neutron stars, by performing non-linear magnetohydrodynamical simulations with the code PLUTO. For both initially predominantly poloidal and toroidal fields, with varying strengths, we find that the field settles down to a mixed poloidal–toroidal configuration, where the toroidal component contributes between 10 and 20 per cent of the total magnetic energy. This is, however, not a strict equilibrium, as the instability leads to the development of turbulence, which, in turn, gives rise to an inverse helicity cascade, which determines the final 'twisted torus' setup. The final field configuration is thus dictated by the non-linear saturation of the instability, and is not stationary. The average energy of the poloidal and toroidal components, however, is approximately stable in our simulations, and a complex multipolar structure emerges at the surface, while the magnetic field is dipolar at the exterior boundary, outside the star.

Key words: instabilities – MHD – turbulence – methods: numerical – stars: neutron.

1 INTRODUCTION

Neutron star(s) (NS(s)) are extremely dense compact objects bearing the strongest magnetic fields known to date in the universe. The surface field strength for ordinary NSs ranges from 10^{12} to 10^{13}G while for magnetars, it goes well beyond 10^{15}G. Despite such estimates for the strength of the magnetic field, its structure is not completely known to us. Polarimetric studies of radio emission from pulsars have been used to probe the geometry of pulsar magnetospheres. Such observations favour a predominantly dipolar magnetic field, although there is evidence for higher multipoles (Chung & Melatos 2011a,b; de Lima et al. 2020). Recent observations in X-rays by the NICER mission have confirmed that the field at the surface is far from an aligned dipole, but rather an intricate multipolar structure is present (Bilous et al. 2019).

The internal field topology is even more difficult to probe directly with observations, but is thought to play a fundamental role in determining the nature and strength of electromagnetic and gravitational wave emission of the star (Thompson & Duncan 1996; Cutler 2002; Güver, Göğüş & Özel 2011). As the field of gravitational wave astronomy advances, it may, in fact, be possible to use gravitational-wave signatures to discriminate between different magnetic field topologies (Lasky & Melatos 2013). It is thus of great importance to obtain a theoretical understanding of the interior field and use numerical simulations to explore its nature.

Several studies have been carried out to investigate the equilibrium configuration of magnetic main-sequence stars and white dwarfs, in which the Lorentz force is balanced by pressure and gravity; e.g. for the axisymmetric case by Braithwaite & Spruit (2006), Braithwaite & Nordlund (2006), Braithwaite (2007), Armaza, Reisenegger & Valdivia (2015) and a similar non-axisymmetric study by Braithwaite (2008). For the NS case, equilibrium solutions in Newtonian gravity were obtained by Haskell et al. (2008), Lander & Jones (2009), Lander, Jones & Passamonti (2010), Lander & Jones (2011), Herbrik & Kokkotas (2017), Frederick, Kuchera & Thompson (2020) and in general relativity by Kiuchi & Yoshida (2008), Ciolfi, Ferrari & Gualtieri (2010), Ciolfi & Rezzolla (2013), Pili, Bucciantini & Del Zanna (2014), Pili, Bucciantini & Del Zanna (2017) and the role of stratification was investigated by Glampedakis, Andersson & Lander (2012), Reisenegger (2009). Finding equilibrium and stability conditions for the magnetic field in stars has been an important long-standing question that dates back to earlier studies by Chandrasekhar & Fermi (1953), Tayler (1957), Tayler (1973), Wright (1973), Markey & Tayler (1973), Markey & Tayler (1974), and Flowers & Ruderman (1977). A purely poloidal field undergoes the so-called 'Taylor instability' and is thus unstable (Ferraro 1954; Monaghan 1965; Bocquet et al. 1995). In NSs, this instability has been studied numerically, in general, relativity by Ciolfi et al. (2011), Lasky et al. (2011), and Ciolfi & Rezzolla (2012), who confirm that an initially poloidal field is unstable on the order of an Alfvén crossing time-scale and toroidal components of the field are generated. The equilibrium configuration is often approximated as a twisted-torus configuration where a toroidal component stabilizes the poloidal field (Braithwaite & Nordlund 2006; Braithwaite 2007) or a tilted-torus configuration with the magnetic axis tilted with respect to the rotation axis (Lasky & Melatos 2013), as the inclination angle between the two grows

★ E-mail: ankansur@camk.edu.pl

(Lander & Jones 2018, 2019). An initial purely toroidal field is also unstable to the azimuthal wavenumber $m = 1$ mode of oscillation, which is independent of the field strength but instead depends on the geometry (Roxburgh 1966; Tayler 1973) and can lead to strong poloidal components developing.

Several open questions remain, however, as to the exact configuration the field will settle down to. Specifically, while it is clear that a mixed field is required for stability, the relative strength of the components cannot be obtained directly from the study of equilibrium configurations that generally allow a degree of freedom in tuning this parameter (see Glampedakis & Lasky 2016 for an in depth discussion of this issue). It is thus possible to obtain models in which the toroidal field strength ranges from a few per cent of (Lander & Jones 2009) to more than an order-of-magnitude higher (Ciolfi & Rezzolla 2013) than the strength of the poloidal component.

In fact, the stability of barotropic stars has been questioned by Lander & Jones (2012) and Mitchell et al. (2015), who hypothesize that all barotropic models are unstable, while Reisenegger (2009) and Akgün et al. (2013) suggest that stratification plays an important role in stabilizing the field, and non-barotropic models of magnetized stars are stable. Since most hydromagnetic instability studies have focused on building equilibrium configurations starting with a specific choice of geometry, fully non-linear time evolution for NSs for a range of initial topologies and a barotropic EOS need to be carried out, to determine not only whether the field is unstable, but also, crucially, what the final state determined by the non-linear saturation of the instability is. It is also important to understand how magnetic helicity is generated and transferred in the star as the instability proceeds. Both superfluid and standard MHD turbulence are expected in NS interiors, and the evolution of the field, especially soon after birth when the star is still differentially rotating, is likely linked to the action of a dynamo in the interior (Thompson & Duncan 1993).

It is crucial to obtain an understanding of these issues, as the field configuration of an NS plays an important role in attempts to determine the mass and radius of the star from X-ray observations (Miller et al. 2019; Riley et al. 2019), and in determining the gravitational wave emission properties of the system (Lasky 2015).

To address the problem in this paper, we perform non-linear magnetohydrodynamical (MHD) simulations of magnetized NSs to characterize the instability, the global evolution, and the final configuration of the magnetic field. We neglect effects due to superfluidity and superconductivity in the core and do not model the crust of the star. These choice are partly due to numerical convenience, but also reflect the fact that we are modelling instabilities on dynamical time-scales, which will determine the configuration of the field shortly after the NS is born. After birth, the star cools down and there is a window during the first few hours of life, where differential rotation has likely been dissipated, but the crust has not yet formed and matter is not yet superfluid, thus justifying an ideal MHD description. Our simulation is relevant in such a scenario, as one would expect this setup to be 'frozen' in (Ciolfi et al. 2010). This field configuration to which the star settles can thus be used as initial conditions for evolution on longer time-scales of 10^3–10^5 yr, over which the Hall effect, ambipolar diffusion, and Ohmic dissipation will affect the magnetic field (Goldreich & Reisenegger 1992; Pons & Geppert 2007). We work in Newtonian gravity as general relativity generally does not affect the qualitative nature of the magnetic instabilities (Siegel et al. 2013), and this allows us to explore a larger portion of parameter space. We explore different setups, both in resistive and ideal MHD, and different initial

conditions, which allow for fields with initially stronger poloidal or toroidal components. The initial field generally goes unstable on an Alfvén crossing time-scale and we follow the development of the instability, which leads to the development of turbulence in the system, which, in turn, seeds the growth of magnetic helicity.

Our results show that, in general, the system reaches turbulent equilibrium, in which the average field strengths settle down to a stable ratio. In all our final field configurations, including those with initially stronger toroidal fields, the field is predominantly poloidal, but a weaker toroidal component ($\lesssim 20$ per cent of the total magnetic energy) is present.

This paper is arranged as follows: In Section 2, we discuss our numerical setup; in Section 3, we discuss our results for the different setups considered in our simulations; Section 4 discusses the effect of resistivity; and Section 5 the onset of turbulence. The convergence of our results is discussed in Section 6, and finally conclusions and discussions are presented in Section 7.

2 PHYSICAL SYSTEM AND NUMERICAL SETUP

We use the publicly available code PLUTO[1] by Mignone et al. (2007) to solve the MHD equations (1–4):

$$\frac{\partial \rho}{\partial t} + \nabla \cdot (\rho \boldsymbol{v}) = 0, \tag{1}$$

$$\frac{\partial \boldsymbol{v}}{\partial t} + \boldsymbol{v} \cdot \nabla \boldsymbol{v} + \frac{1}{4\pi\rho} \boldsymbol{B} \times (\nabla \times \boldsymbol{B}) + \frac{1}{\rho}\nabla p = -\nabla\Phi, \tag{2}$$

$$\frac{\partial \boldsymbol{B}}{\partial t} + \boldsymbol{B}(\nabla \cdot \boldsymbol{v}) - (\boldsymbol{B} \cdot \nabla)\boldsymbol{v} + (\boldsymbol{v} \cdot \nabla)\boldsymbol{B} = 0, \tag{3}$$

$$\frac{\partial p}{\partial t} + \boldsymbol{v} \cdot \nabla p + \rho c_\text{s}^2 \nabla \boldsymbol{v} = 0, \tag{4}$$

where c_s is the sound speed. The above set of equations are closed with a barotropic EOS given by $p = p(\rho)$, which we take to be an $n = 1$ polytrope. Although the initial parameters are defined in terms of primitive variables (p, ρ, $\boldsymbol{v}$, $\boldsymbol{B}$), computations are done using conservative variables (ρ, $\rho\boldsymbol{v}$, E, $\boldsymbol{B}$), where $E = \rho\epsilon + \rho\boldsymbol{v}^2/2 + \boldsymbol{B}^2/2$. The above set of equations are solved, except for equation (4), where the pressure is calculated using the EOS and the density (helping to maintain the barotropy of the system), in a spherical coordinate system in three dimensions using a static grid, which is divided into a number of points with N_r in the radial direction r, N_θ in the polar direction θ, and N_ϕ in the azimuthal direction ϕ. However, our r-grid is non-uniform having a resolution ($\Delta r \sim$ 0.19 km) inside the star as compared to the atmosphere (where $\Delta r \sim 0.25$ km). Interpolations are done with a piece-wise parabolic function, which is accurate to second order in space. A Runge Kutta 3 time-stepping is used and we set the Courant–Friedrichs–Lewy limit to 0.3. We use a Harten–Lax–van Lee Riemann solver for computing the fluxes. The solenoidal constraint $\nabla \cdot \boldsymbol{B} = 0$ is maintained using the hyperbolic divergence cleaning method. The code does not solve the Poisson equation. We analytically solve for the gravitational potential in different regions of the star and provide it as an input. Our gravitational field does therefore not evolve with time. The density distribution of the star is, however, only very weakly affected by the magnetic field and this is generally a good approximation (Haskell et al. 2008).

---

[1] http://plutocode.ph.unito.it/

2.1 Initial conditions

We consider a non-rotating star that is modelled by solving the Lane–Emden equation with $n = 1$ polytrope such that[2] $P = k_\star \rho^2$, where $k_\star = 4.25 \times 10^4 \, \text{gm}^{-1}\text{cm}^{-5}\text{s}^{-2}$.[3] We choose a background star with a total mass of $1.4 \, \text{M}_\odot$, radius $R_\star = 10$ km, and central density $\rho_c = 2.17 \times 10^{15} \, \text{gm cm}^{-3}$. The density of the star only has radial dependence given by

$$\rho = \rho_c \frac{\sin y}{y}, \tag{5}$$

where $y = \frac{\pi r}{R_\star}$. As in most numerical MHD studies, it is necessary to replace the vacuum outside the stellar surface with an atmosphere of low-density fluid, in order to avoid computational difficulties due to diverging Alfvén velocities as the density falls to zero. Equation (5) shows that ρ falls rapidly and vanishes while approaching the edge of the star. Since the atmosphere has a non-zero density ρ_{atm}, this would cause a sharp gradient across the boundary of the star. In order to prevent such unrealistic jumps in density at the surface, we cut the star at a radius of $r = 0.975R_\star$ so that $\rho(r < =R) > \rho_{atm}$. We set $\rho_{atm} = 10^{12} \, \text{gm cm}^{-3}$ and explore two different setups, one in which the atmosphere extends up to a distance of $1.2R_\star$ with no resistivity while another which extends up to $2R_\star$ and includes a resistive layer in the atmosphere of the star, which we will discuss in detail in the following sections. We start our simulation with two different initial conditions. The first is obtained by introducing a purely poloidal field (Haskell et al. 2008),

$$B_r = \frac{B_p \cos \theta}{\pi(\pi^2 - 6)}[y^3 + 3(y^2 - 2)\sin y + 6y \cos y], \tag{6}$$

$$B_\theta = \frac{B_p \sin \theta}{2\pi(\pi^2 - 6)}[-2y^3 + 3(y^2 - 2)(\sin y - y \cos y)], \tag{7}$$

$$B_\phi = 0.0, \tag{8}$$

inside the star and

$$B_r = \frac{B_p R^3 \cos \theta}{r^3}, \tag{9}$$

$$B_\theta = \frac{B_p R^3 \sin \theta}{2r^3}, \tag{10}$$

$$B_\phi = 0, \tag{11}$$

outside the star, where B_p is the surface poloidal magnetic field strength, which we set to be $B_p = 10^{17}$ G. Such a strong magnetic field reduces the time-scales allowing us to explore greater possibilities within a shorter run of the simulation. To accelerate the development of the instability, we add a small perturbation to the velocity of the fluid elements located at $(60° \leq \theta \leq 120°)$ and $(7 \leq r \leq 9 \, \text{km})$, given by

$$v_\theta = \sqrt{\frac{15}{8\pi}} \sin \theta \sin 2\phi, \tag{12}$$

$$v_\phi = \sqrt{\frac{15}{8\pi}} \sin \theta \sin 2\phi \cos \theta. \tag{13}$$

We confirm that this has no other effects apart from triggering the instability, which still grows but takes longer to develop without the perturbation. Additionally, we also test another initial condition,

with the same poloidal field, but a stronger toroidal component $(B_t = 2 \times 10^{17})$ inside the star given by

$$B_\phi = B_t \frac{\sin y \sin \phi}{\pi}, \tag{14}$$

and study its evolution with time.

2.2 Time-scales

The two important time-scales in our simulation are the sound crossing time (τ_{c_s}) and the Alfvén time (τ_A). τ_A is defined by

$$\tau_A = \frac{2R_\star \sqrt{4\pi \langle \rho \rangle}}{\langle B \rangle}, \tag{15}$$

where $\langle .. \rangle$ represent volume-averaged quantities. The field evolution depends on the Alfvén time-scale while the hydrostatic equilibrium depends on the shorter sound crossing time. We chose B_p such that $\tau_{c_s} \sim 0.1\tau_A$. The Alfvén time is not a constant throughout the entire run of the simulation, instead, it varies with the change in magnetic field. Initially, the magnetic field rearranges and its density becomes higher in the core of the star. Thus, τ_A changes in subsequent times and does not remain constant. In our simulations with $B_p = 1 \times 10^{17}$ G, we obtain an average $\tau_A = 1.3$ ms.

2.3 Boundary conditions

Our objective is to understand the interior field strength and configuration of an NS if the exterior dipolar field has a given strength, inferred from observations. With this physical picture in mind, we set the exterior boundary condition of our simulation by setting the magnetic field in the r and the θ directions according to equations (9)–(11). At the outer ghost cells, we evaluate B_r and B_θ at $r = r[\text{END}] + \delta r$. Here, $r[\text{END}]$ is the radial value corresponding to the end of the atmosphere, and δr is the difference in radial grid spacing. We use periodic boundaries for the magnetic field along the ϕ direction. The velocities are all set to zero at the boundaries.

Note that to correspond to the physical prescription described above, the exterior boundary should be far from the star, where the dipolar component provides the dominant contribution to the spin-down torque. Due to numerical limitations, we are far more restricted and, in practice, have to place our exterior boundary close to the star. As already mentioned, we have studied two setups, with the exterior boundary at $1.2R_\star$ and another which extends up to $2R_\star$. We find that our results do not depend significantly on the location of the outer boundary. Extending the atmosphere farther out, in regions where higher multipoles of the field fall off much more rapidly than the dipolar component, will, thus not alter our conclusions.

At the inner boundary in the radial direction, we set the density of the star to follow the profile given by equation (5), while at the outer boundary we set the density to be ρ_{atm}.

3 RESULTS

We now move on to discuss the results of our simulations. In this section, we will first present the results of our non-resistive setup, and then discuss all the results corresponding to the resistive atmosphere, in detail, in Section 4. Nevertheless the main conclusions are not affected by the choice of setup. All setups, both resistive and non-resistive, are initially unstable, independently of whether we choose a purely poloidal field as an initial condition or a twisted torus with a stronger toroidal component. In all cases, we find that
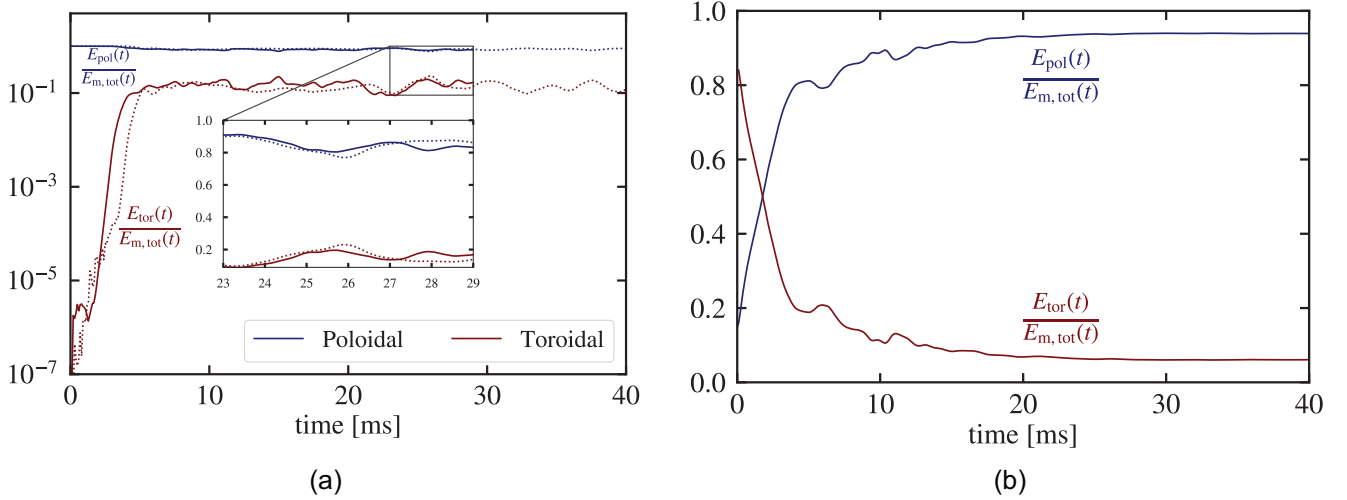
---

[2]PLUTO does not have an inbuilt barotropic EOS. We have suitably modified the ISOTHERMAL EOS such that the proportionality constant $k_\star$ remains fixed.

[3]All our work is carried out using CGS units.

Figure 1. (a) A comparison of the poloidal (E_{pol}) and toroidal (E_{tor}) field energies normalized by the total magnetic field energy $E_{m, tot}$ at each time t for our model with $\{B_p = 10^{17}$ G, $B_t = 0\}$. The atmosphere extends up to 12 km (represented by solid lines), whereas the dotted lines represent a model with an extended atmosphere till 16 km. The inset in the figure shows a linear scale comparison between the two components. (b) Evolution of the field energies starting with an initially stronger toroidal field with $\{B_p = 10^{17}$ G, $B_t = 2 \times 10^{17}$ G.$\}$ We find $E_{tor} \leq 20$ per cent $E_{m,tot}$ in both the cases.

turbulence develops and the field settles to a state which is not strictly an equilibrium, but in which the non-linear saturation of the instability determines a stable average of the field strengths, such that the energy of the toroidal component is roughly $10-20$ per cent of the total magnetic energy.

3.1 Field configurations and strengths

Let us analyse in detail the evolution of the relative strengths of the poloidal and toroidal field components for our non-resistive setup. Fig. 1(a) shows the evolution of poloidal and the toroidal magnetic field energies normalized by the total magnetic field energy at each time for the entire run of a simulation in which the initial condition was a purely poloidal field. The toroidal component initially gains strength from the initial perturbation we gave. After 3 ms, the poloidal field becomes unstable and the toroidal component undergoes an exponential growth with its strength becoming comparable to the poloidal component. This period of exponential growth corresponds to 1 Alfvén crossing time during which the toroidal component fully develops close to the neutral line. After $t = 5$ ms, the field reaches pseudo-equilibrium and the evolution becomes less dramatic. However, the toroidal part remains weaker (≤ 20 per cent of the total magnetic energy) than its poloidal counterpart. Even with a mixed-field initial condition with a stronger toroidal component ($B_t = 2 \times 10^{17}$ G as compared to a poloidal strength of $B_p = 10^{17}$ G), we see that the final configuration settles to a weaker toroidal field as compared to the poloidal field (see Fig. 1b).

Fig. 2 shows snapshots of the formation of the toroidal component in the meridional (x–z) plane and the equatorial (x–y) plane, for an initially poloidal field. The colours show the strength of B_ϕ only. The region inside the star, where the field lines close, moves in and out during the initial stage when the fluid starts readjusting to the changing magnetic field. The null line seems to move outwards during the evolution. As pointed out by Glampedakis & Lasky (2015), closed field lines in the core of the star cause it to be magnetically decoupled with the rest of the star by developing a velocity lag between these regions. During the initial stage, the

field can be treated as a linear perturbation on top of a stationary background field. The non-linear terms start to dominate after the onset of the 'kink'-instability at $t \sim 3$ ms. The dynamics thereafter change rapidly, breaking the axisymmetry and the field inside the star attends a complex geometry with the mixed-field configuration. However, there is a caveat. The non-linear terms may have an initially stronger role because of our strong field. The instability is, however, inherently non-linear, and will, in general, grow until these non-linear terms block it. The toroidal component creates vortex-like structures (shown in the lower panel of Fig. 2) in order to conserve the magnetic helicity (Ciolfi et al. 2011), which is initially zero due to our choice of a purely poloidal field as initial condition. These structures show higher order modes (see Fig. 2 at $t = 3.3$ ms) which are replaced by lower order modes at later stages during the evolution. The presence of the kink-instability is visible in our simulation in Fig. 3(a), where the absolute value of the magnetic field strength is plotted on the equatorial plane of the star. The deep blue line feature at $r \sim 8$ km at $t = 1.5$ ms shows the location of the neutral line. This gets distorted and small lumps are seen at $t = 3$ ms, which evaporate thereafter. Similarly, we plot the kinetic energy of the star on the equatorial plane (Fig. 3b) and note the different modes of oscillations present in our simulation. Higher order modes are visible at $t = 2.5$ ms, and start coupling with each other at later stages as seen at $t = 20$ ms.

The magnetic helicity H_m measures the amount of 'twist' in the magnetic field and is given by

$$H_m = \int_V \boldsymbol{A} \cdot \boldsymbol{B} \, dV, \tag{16}$$

where $\boldsymbol{A}$ is the magnetic vector potential. The helicity in equation (16) is a conserved quantity in ideal MHD, with a non-zero value generally linked to non-ideal effects such as reconnections. Fig. 4(a) shows the time evolution of the quantity $H_m/\bar{H}_m$, where the magnetic helicity is normalized by $\bar{H}_m = 0.5 \times E_{m, tot} \times 0.8R_\star$, where $E_{m,tot}$ is the volume integrated total magnetic energy. We remark that the choice of gauge for $\boldsymbol{A}$ is irrelevant in this case. Initially, the helicity remains zero until there is axisymmetry in our simulation. However, as the star tries to reach an equilibrium, the helicity becomes non-zero.
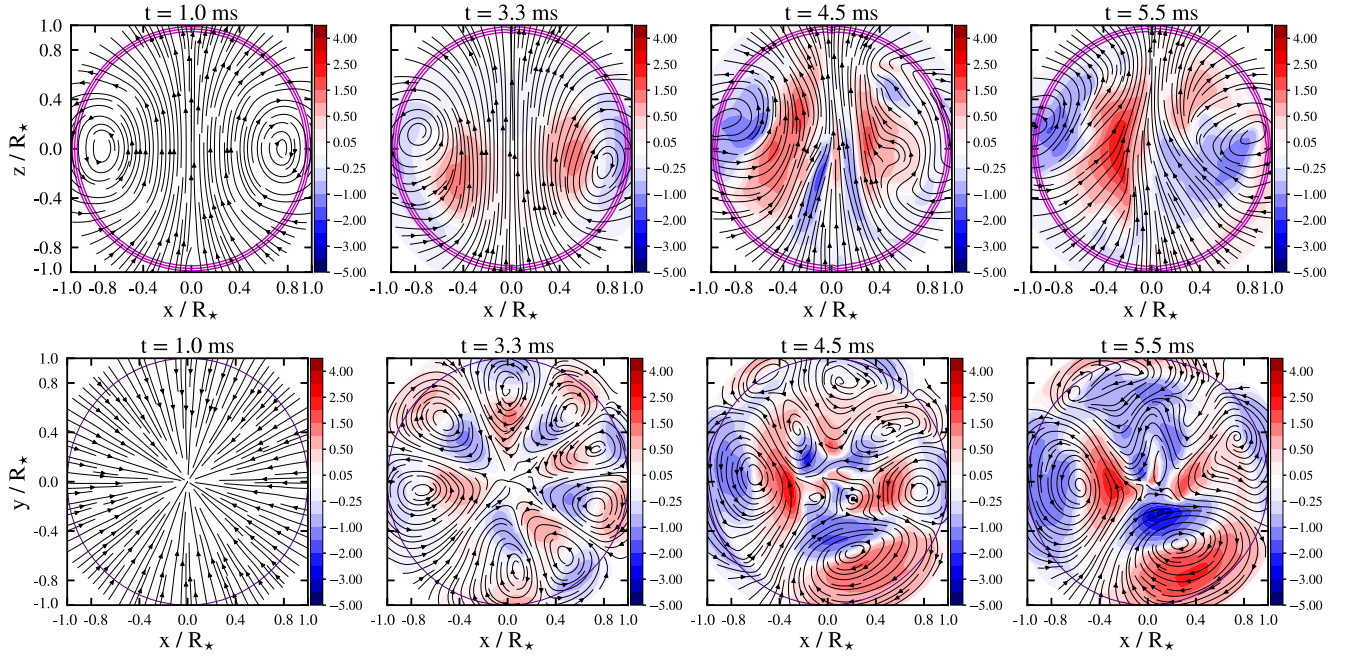
Figure 2. Snapshots of the star from meridional view (top panel) and equatorial view (bottom panel) showing the development of a toroidal field (colour scale indicates strength of B_ϕ normalized by 2×10^{16} G). In the top row, the purple lines show equidensity contours $\rho \in (10^{13}, 5 \times 10^{13}, 10^{14})$ gm cm^{-3}. The streamlines shown are the poloidal field lines that thread through the main body of the star. In the bottom row, the streamlines show the toroidal field lines and the violet contour shows the location of $R_\star$. Times of the snapshots are given as figure titles.
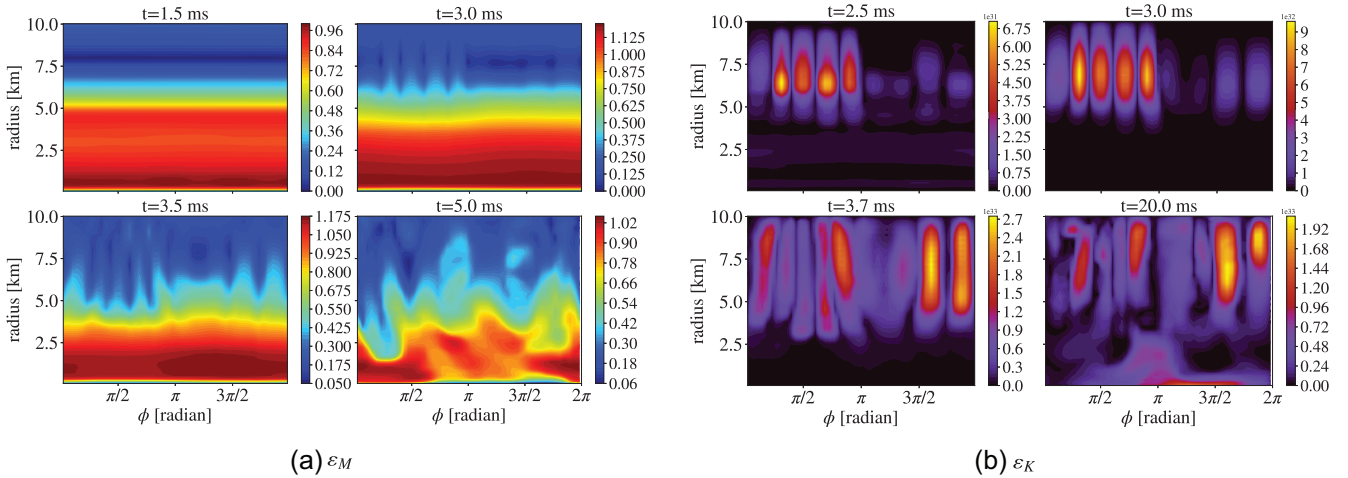

Figure 3. Energy densities plotted in the equatorial plane of the star, i.e. at $\theta = 90°$ for different times t in our simulation. At $t = 3$ ms, we see that the neutral line gets disrupted showing the formation of a strong toroidal component.

We will see in detail Section 5 that this is linked to the development of turbulence, in which following the initial development of kinetic helicity after the instability, an inverse cascade takes helicity from the resistive small scales to larger scales. This is expected as the system attempts to conserve helicity by transferring it from the small-scale turbulent field to the larger scale field, thus moving it further from the resistive scale (Biskamp 2003).

The atmosphere also plays a role in governing the internal dynamics of the field. We explore its effect by running simulations with different values of $\rho_{\rm atm}$ and find that an atmosphere with higher density fluid (which allows the star to lose more magnetic energy) causes a relatively weaker toroidal field as compared to an atmosphere with lower density fluid. Extending the atmosphere

up to a larger distance also does not influence much the overall growth of field-energies. This is shown as dotted lines in Fig. 1(a). As the influence of higher order multipoles is stronger close to the surface, the fact that the results are mostly unaffected by the position of the boundary within a few stellar radii gives us a degree of confidence that these are a good approximation to the physically realistic situation, in which the dipolar field component is inferred further out at the light cylinder.

Fig. 4(b) shows the variation of the volume-averaged magnetic energy density ($\varepsilon_M = (B_r^2 + B_\theta^2 + B_\phi^2)/8\pi$) and the volume-averaged kinetic energy density ($\varepsilon_K = \rho(v_r^2 + v_\theta^2 + v_\phi^2)/2$) with time. A peculiar feature of our evolutions is the initial rearrangement of the poloidal field, due to our choice of initial condition in which
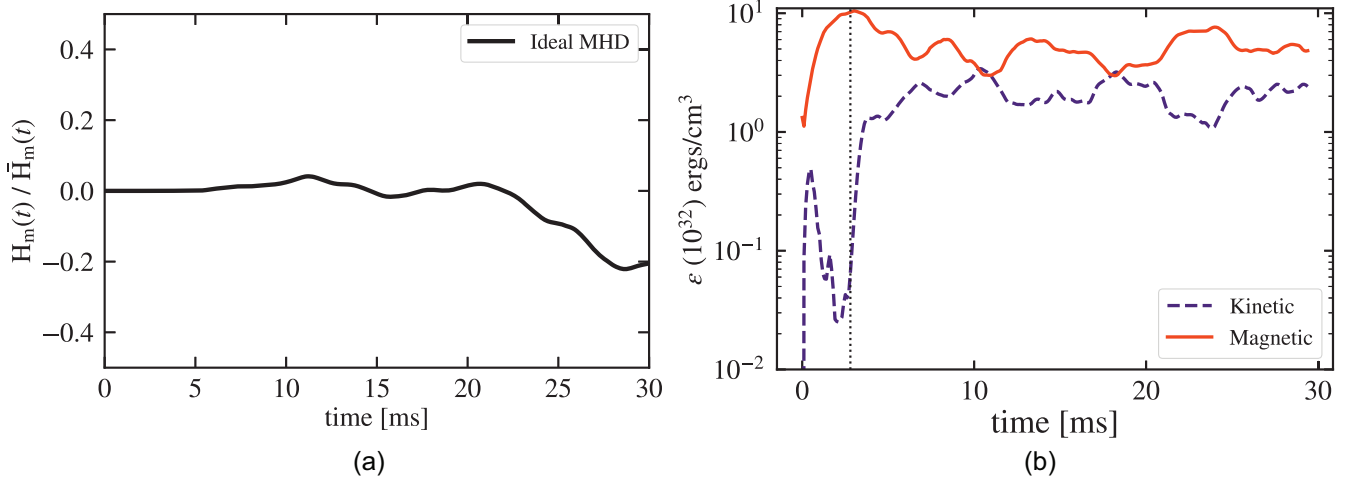
Figure 4. (a) Time evolution of the magnetic helicity for ideal-MHD setup (i.e. resistivity $\eta_0 = 0$). (b) Average magnetic field energy density (ε_M) and the average kinetic energy density (ε_K) normalized by 10^{32} erg cm^{-3} plotted as a function of time. After an initial transient, the onset of instability is seen at $t = 3$ ms (represented by the dotted line) when the there is a sharp rise in the kinetic energy of the system.

the field is stronger in the outer core. This leads to a rapid initial readjustment which takes it to a more stable configuration in which stronger near the centre of the star and weaker in the exterior regions. As a consequence at $t \sim 1$ ms, there is a small peak in ε_K that the fluid gains in response to the initial readjustment of the magnetic field. Furthermore, when we take a volume average of the field, this rearrangement is visible as a sudden rise in ε_M, as the field becomes stronger in the interior region over which we integrate, as seen in the first few milliseconds (Fig. 4(b)). Following this initial transient the field settles down, until it is affected by the onset of the 'kink' instability at $t = 3$ ms (after ~ 1 Alfvén crossing time) when the magnetic energy falls and the kinetic energy rises sharply. This is ascribed to the conversion of magnetic energy to kinetic energy (see also Lasky, Zink & Kokkotas 2012). Finally, we note that the presence of the varicose mode, in which the flux tube near the neutral line undergoes a change in cross-sectional area, is difficult to observe in three-dimensional (3D) visualization of our simulation (see Fig. 5) because our Alfvén crossing time is small and the instability growth time is thus too rapid. However, the kink instability is somewhat visible at $t = 3$ ms.

3.2 Growth times

We Fourier-decompose B_ϕ and ρ into different modes m and calculate the complex weighted averages, as prescribed in Zink et al. (2007) and Lasky et al. (2011), given by

$$C_m(f) = \int_0^{2\pi} f(\bar{\omega}, \phi, z = 0)e^{im\phi}d\phi, \tag{17}$$

where $\bar{\omega} = \sqrt{x^2 + y^2} = 0.8R_\star$ lies in the equatorial plane of the star, and $f \in (\rho, B_\phi)$. Since equation (17) results in a complex number, we take the modulus to obtain $C_m(f)$. Fig. 6 shows the modal structure of the instability. All the different modes $m \in (1, 2, 3, 4)$ considered show the presence of the instability as each one grows exponentially by three to four orders of magnitude in one Alfvén crossing time before settling down to a pseudo-equilibrium state. For $C_m(\rho)$, visually, the lower order modes grow faster, i.e. $m = 1$ mode grows faster than $m = 2$, and so on, whereas for B_ϕ,

we see that the higher order modes grow faster, i.e. $m = 3$ mode grows faster than $m = 2$, and so on.

Following Lasky et al. (2011), the instability growth time for a particular m during the exponential phase is defined by

$$\tau_g = \frac{\Delta t}{\Delta \ln[C_m(B_\phi)]}. \tag{18}$$

Fig. 7 shows the growth times for the different modes with varying surface magnetic field strength. In calculating equation (18), we do not adopt a single point, rather we take different realizations during the exponential phase and then calculate the mean and standard deviation of growth times. We find that the τ_g for the various modes are not significantly different from each other unlike the prediction by Tayler (1957) where higher order modes have a shorter growth time. It should be noted that our field strength B_p corresponds to a weaker $\langle B \rangle$, which is otherwise used in the literature to calculate τ_A. From Fig. 7, we find that the growth time-scales approximately with the chosen range of magnetic field, although the large error bars do not allow to accurately test the scaling.

3.3 Power spectrum

We use the `healpy` modules to calculate the angular power spectrum of B_r. Any scalar function defined on a sphere can be expanded into spherical harmonics. Given a map, the angular power spectrum is calculated using

$$C_\ell = \frac{1}{2\ell + 1} \sum_{m=-\ell}^{\ell} \langle |a_{\ell m}|^2 \rangle, \tag{19}$$

where

$$a_{\ell m} = \int d\boldsymbol{u} \, B(\boldsymbol{u}) Y_{lm}^\star(\boldsymbol{u}). \tag{20}$$

$B(\boldsymbol{u})$ is a scalar field depending on the angular coordinates $\boldsymbol{u}$ and $Y_{lm}^\star$ is the complex conjugate of the spherical harmonics. Fig. 8(a) shows that $\ell = 1$ contributes maximum to the total power in B_r, followed by $\ell = 2$ and 4, respectively. In Fig. 8(b), we decomposed the magnetic field into vector spherical harmonics and calculated the power according to equation (19) for multipoles $\ell \in (0, 1, 2, 3)$. In this case, the $a_{\ell m}$'s were calculated using the definition of
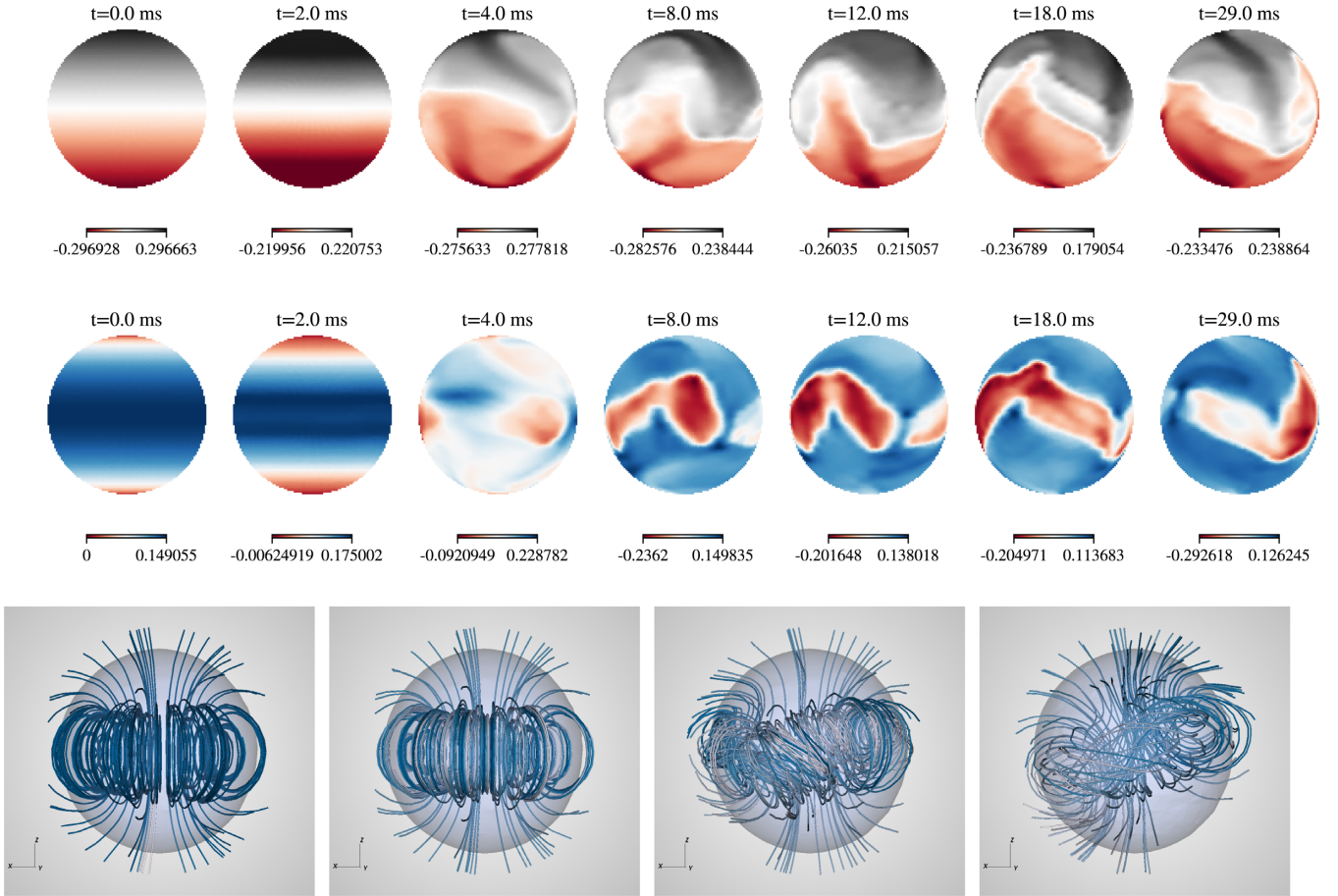
Figure 5. Surface distribution of B_r (top panel) and B_θ (middle panel) at various times t, given as figure titles. The colour scale (normalized by 10^{17} G) shows the strength of the field. The bottom panel shows 3D visualization of the magnetic field configuration at times $t = 0$, 3, 10, 20 ms (from the left- to right-hand panel).
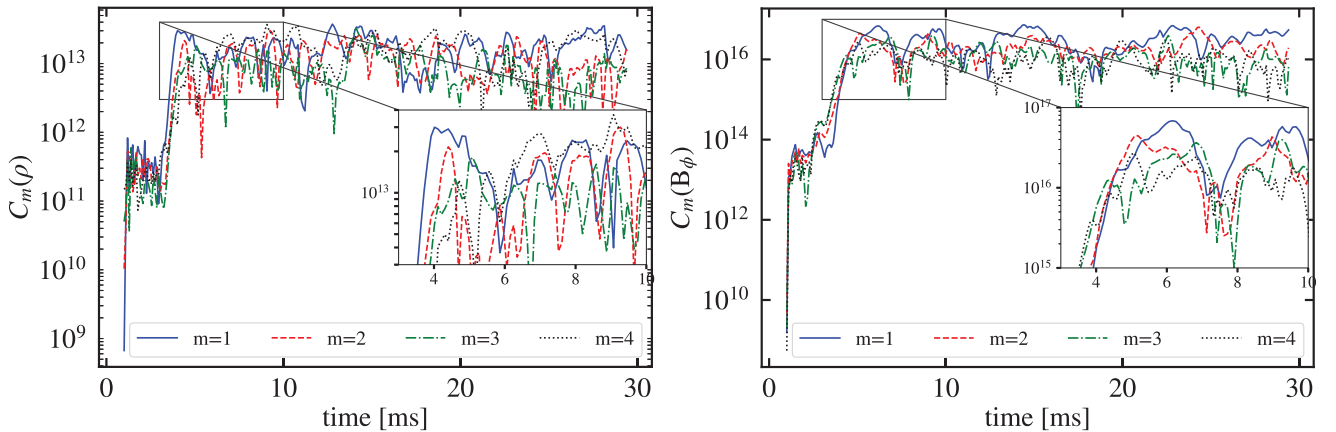

Figure 6. Fourier decomposition of ρ (left-hand panel) and B_ϕ (right-hand panel) into different azimuthal modes $m \in (1, 2, 3, 4)$, as a function of time for $B_p = 10^{17}$ G. The inset shows that the lower order modes for ρ grow faster compared to the higher order modes, however, the reverse is observed for B_ϕ where the higher order modes grow faster. An exponential growth is seen in both the quantities, which saturates after few Alfvén crossing times when the star attends a pseudo-equilibrium state.

vector multipole moments (see for e.g. Barrera, Estevez & Giraldo 1985). Initially, the field is dipolar. However, the higher order multipoles gain power with time and the field structure becomes complex. This can be approximately seen in Fig. 5 where the

field configuration evolves, and the neutral line migrates. We note, however, that the time-scale on which this tilt occurs is dictated by numerical dissipation, and faster than would be expected in a realistic NS.
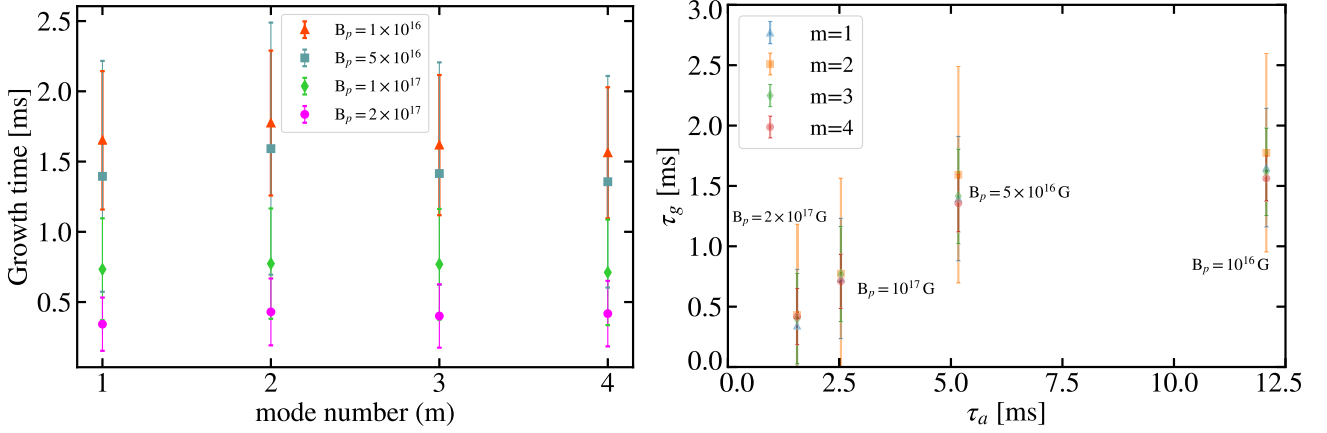
Figure 7. The left-hand panel shows the growth times for different modes with varying surface magnetic field strengths. The right-hand panel shows correlation between the growth times and the Alfvén crossing time. Our results are consistent with the expected linear relation between two quantities, but given that our error bars are large we do not present a fit to the data.
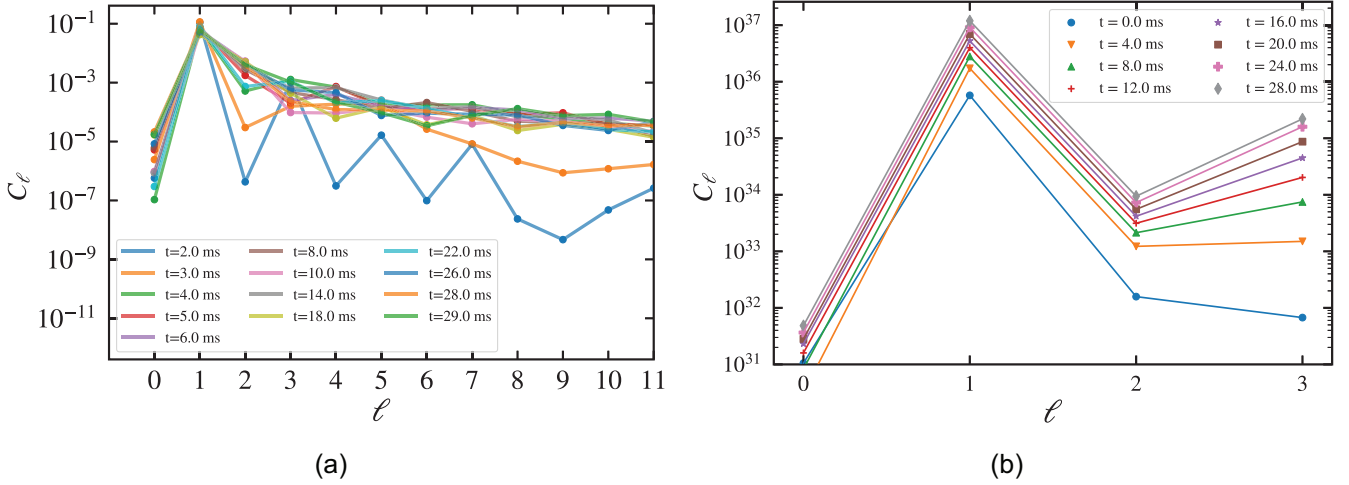

Figure 8. (a) Angular power spectrum for the scalar field B_r calculated at $r = R_\star$ plotted as a function of multipoles. (b) Power spectrum calculated for the magnetic field by decomposing it into vector spherical harmonics. The colours show different times in our simulation.

4 EFFECT OF RESISTIVITY

In the previous section, we have considered a non-resistive setup in ideal-MHD, which reflects the expectation that the NS interior is a highly conductive medium (at least for young NSs and on the dynamical time-scales we are interested in, over which mechanisms such as the Hall effect or Ohmic dissipation do not have time to act). In practice, however, this approximation breaks down close to the surface of the NS as the density decreases, and resistive effects play an important role in the long-term evolution of the magnetic field (for a recent review see Pons & Viganò 2019). As one moves further towards the exterior, a low-density plasma is thought to surround the NS, in which now the tenuous fluid is tied to the magnetic field and the force-free approximation is generally used to understand the dynamics of the magnetosphere and the emission properties of the star (Goldreich & Julian 1969; Spitkovsky 2006; Philippov & Spitkovsky 2018).

In practice, most numerical studies of fields in NS interiors have approximated the exterior plasma in terms of an atmosphere with a resistivity, mostly to prevent shocks at the stellar boundary,

which otherwise lead to numerical instabilities. Although our non-resistive setup is stable for a dense enough atmosphere, we none the less explore the effects of resistivity on the simulation, in order to investigate if any substantial differences arise. We use a profile given by $\eta(r) = 0$ if $r < 0.9R_\star$, otherwise, $\eta(r) = \eta_0$ if $r \geq 0.9R_\star$, where η_0 is a constant.

The diffusion time-scale, defined as $\tau_d = R_\star^2/\eta$, is larger than the Alfvén crossing time ($\tau_d \geq 10\,\tau_A$). We choose a value of η_0 such that this condition is satisfied. This leads us to the following relation $\eta_0 \leq R_\star\langle B\rangle/\sqrt{4\pi\langle\rho\rangle} = 10^{12}$ cm^2 s^{-1}. We set $\eta_0 = 10^8$ cm^2 s^{-1} in our simulation. The above choice of the profile maintains the ideal-MHD condition in the bulk of the star. We explore different values of $\eta_0 \in \{10^8, 10^{10}, 10^{12}\}$. Additionally, we extend our atmosphere up to 20 km ($= 2R_\star$). Fig. 9(a) shows the long-term evolution of the poloidal and toroidal field energies (both normalized by the total magnetic field energy at each time) for a model with $\eta_0 = 10^8$ cm^2 s^{-1}. Here again, we find that $E_{B_\phi} \leq 20$ per cent of $E_{\mathrm{m,\,tot}}$. The value of η_0 mostly modifies the time-scales in our simulation as the onset of instability changes as illustrated in Fig. 9(a).
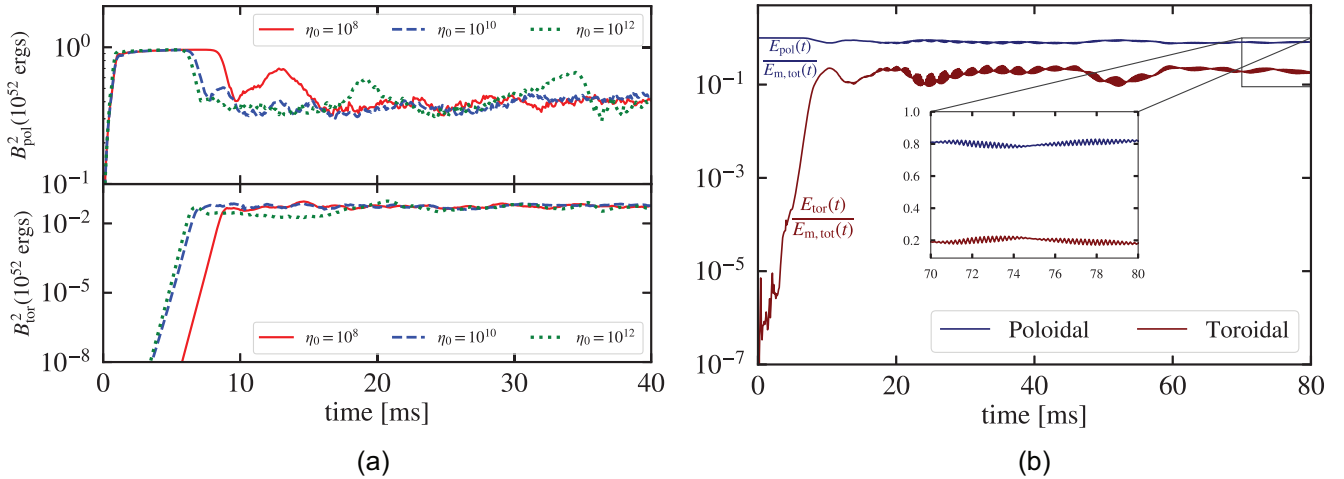
Figure 9. (a) Poloidal and toroidal magnetic field energies as a function of time for three different values of η_0. (b) Long-term evolution for the poloidal and toroidal field energies, normalized by the total magnetic energy, for the resistive atmosphere setup. The inline plot shows that $E_{\rm tor} \sim 20$ per cent $E_{\rm m,tot}$.

5 TURBULENCE

The presence of turbulence, which drives the evolution and properties of the systems in the presence of an embedded magnetic field, is very prominent in astrophysics, e.g. in accretion discs, interstellar medium, stellar winds, etc. In fact, X-ray observations reveal that the magnetic field of the sun is in a turbulent state (Lites et al. 2008). We expect NSs to be turbulent soon after their birth where the heat and the escaping neutrinos provide the energy source. The turbulence decays after a short time-scale (~ 1 d) as this energy source disappears, but is likely to play a role in the development of the field on the short time-scales of hours we are examining, before the crust solidifies. Furthermore, even as the star evolves, difference in angular velocity between the superfluid and the rest of the star is likely to lead to turbulence (Peralta et al. 2006; Andersson, Sidery & Comer 2007). Our simulations show that initial magnetic and kinetic energy drives the turbulence and the star reaches a turbulent 'equilibrium', where average quantities can be studied, but in which the field is far from a stationary dipole. The non-linear saturation of the initial instabilities, lead, through the action of a small-scale dynamo, to a turbulent mixed toroidal–poloidal field configuration, in which the ratio, averaged over the volume, of the energies in the two components reaches an equilibrium. When the Hall effect starts to dominate, this will also contribute to the development of turbulence (Wareing & Hollerbach 2009).

To quantify this statement, we start by studying the distribution of kinetic energy over different length-scales. We plot the spectra for the kinetic and magnetic energies, as a function of wavenumbers (k) in Fig. 10(a). As expected, the system shows higher dissipation of energy for smaller scale eddies through viscosity. Thus, the dynamics inside the star is turbulent. The classical Kolmogorov theory (Kolmogorov 1941) predicts that the turbulent energy spectrum in incompressible[4] hydrodynamic turbulence follows $E(k) \propto k^{-5/3}$, where k is the modulus of the wave vector $\left(k = \sqrt{k_x^2 + k_y^2 + k_z^2}\right)$. In order to calculate the energy spectrum, we convert each velocity component into Cartesian space and Fourier transform them

according to

$$\boldsymbol{u}(\boldsymbol{k}) = \iiint_{\boldsymbol{R}^3} \boldsymbol{u}(\hat{\boldsymbol{x}}) e^{i\boldsymbol{k}.\boldsymbol{x}} d^3 \boldsymbol{x}. \tag{21}$$

In Fig. 10(b), we plot the Kolmogorov spectrum for kinetic energy for our resistive setup. Our spectra are consistent with a Kolmogorov like dependence, however, in MHD turbulence, where the main interaction happens within wave packets moving with Alfvén velocities, the scaling relation follows $E(k) \propto k^{-3/2}$ (Iroshnikov 1964; Kraichnan 1965). While previous numerical work has revealed the presence of a Kolmogorov spectrum also in MHD turbulence (Biskamp 2003), consistently with our interpretation, it is not possible to exclude $k = -3/2$ and determine the exact scaling relation with our limited resolution. Future high-resolution studies are required to determine the exact nature of the turbulence in the NS problem. We note that the magnetic Reynolds number in MHD turbulence is $R_{\rm m} = Lv/\eta_0 = 10^6$, and since, $R_{\rm m} >> 1$, the magnetic field lines are advected with the fluid flow and diffusion is unimportant.

5.1 Cascade directions

As discussed before, the magnetic helicity ($H_{\rm m}$) is an ideal MHD invariant and as such its spectral density is conserved in non-linear interactions. Fig. 11(a) shows the variation of $H_{\rm m}$ with time for two different values of η_0. However, as turbulence is excited by the magnetic instabilities, $H_{\rm m}$ is created on the resistive scale on which non-ideal effects (dictated in our case by numerical resistivity) act, i.e. its value becomes non-zero, and it is scattered to different length-scales. This transfer proceeds from larger to smaller wavenumbers showing an inverse cascade (Frisch et al. 1975), as the system attempts to conserve $H_{\rm m}$ by moving it to scales much larger than the resistive scale. With increasing time, the peak of the magnetic helicity spectrum shifts to smaller k showing the inverse cascade phenomenon, as seen in Fig. 11(b).

This confirms the picture that turbulence plays a key role, by allowing to generate helicity in the system at small scales, and transfer it from the turbulent small scale structures to the larger scale magnetic field, thus creating a twisted-torus structure.

We note that at the end of our simulations turbulence has not decayed, but the average quantities, such as the average field
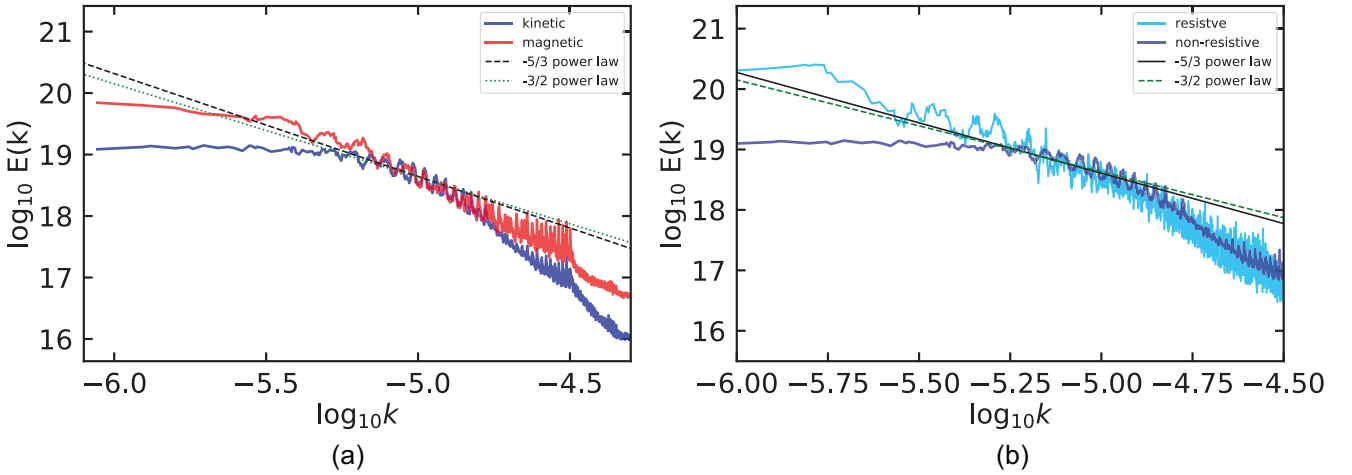
---

[4]Given the high speed of sound in NSs, we expect most eddies to be subsonic, and the effects of compressibility to be negligible.

Figure 10. (a) Kinetic and magnetic energy spectra for our non-resistive setup. (b) A comparison of the kinetic energy spectrum between our resistive and non-resistive setups. In both the plots, the black-dashed line shows $-5/3$ power law (Kolmogorov), while the green-dotted line shows $-3/2$ power law (Iroshnikov–Kraichnan). We do not have a sufficiently high resolution to distinguish between the two spectra, but our results are consistent with a Kolmogorov spectrum, as found by previous MHD simulations, as described in the text.
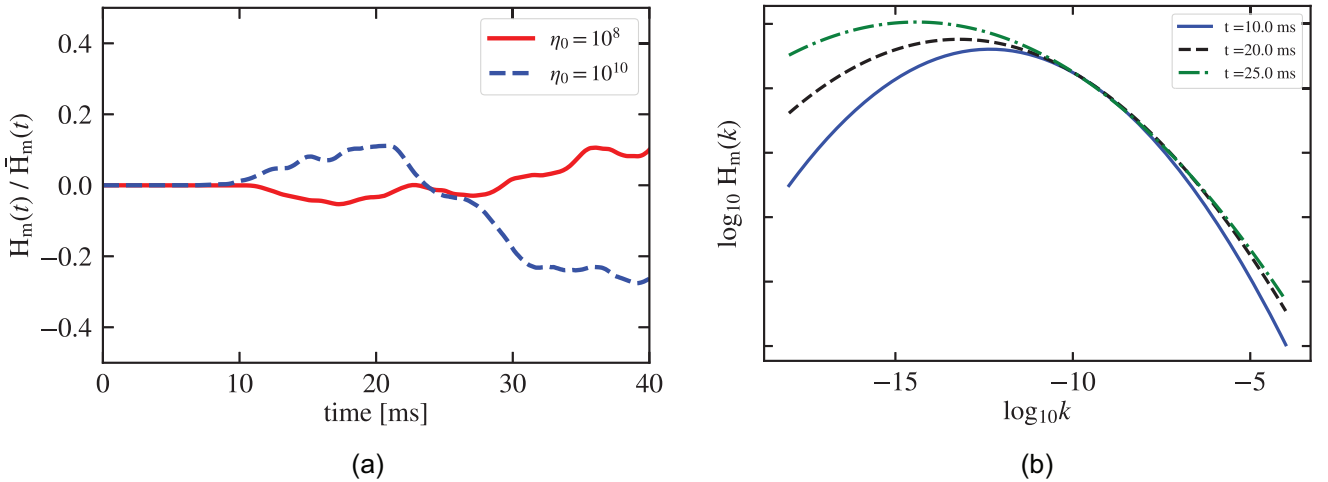

Figure 11. (a) Magnetic helicity plotted as a function of time for two different values of η_0 for a setup with $\tau_A \sim 10$ s. The helicity becomes nonzero as the instability sets in after one Alfvén crossing time. (b) The magnetic helicity spectrum at different times showing the phenomenon of an inverse cascade from the resistive small scales to larger scales.

strengths and magnetic energies have reached an equilibrium, which is roughly constant over many Alfvén time-scales. Longer simulations are needed to study the decay of turbulence, and understand whether in this case additional instabilities will appear also in our barotropic setup, as suggested by Mitchell et al. (2015).

6 CONVERGENCE

In this section, we present our convergence tests focusing, in particular, on the non-resistive setup. Fig. 12(a) shows the variation in error of the total mass of the star with time and number of points in our grid, respectively.

The mass of the star as a function of time was calculated assuming spherical symmetry. However, the poloidal field makes the star oblate and pushes material out which causes the loss of spherical symmetry. This effect is not taken into account in our calculation, as it is expected to deform the spherical profile of the star by less than ≈ 0.01 per cent for a field of $B = 10^{16}$ G (Haskell et al. 2008). In

fact, we see that the highest resolution has the least error in the total mass. We find that the error reduces with an increase in the number of grid-points, and the mass determination appears to converge.

We also analyse the energy in the toroidal field, which is one of our key observables. In this case point-wise, convergence is almost certainly lost, as turbulence develops. If the code is converging, we expect the difference in energies for our middle-lowest resolution setup (defined as 'top') to be higher than the difference in energies for the highest middle resolution (defined as 'bottom'). This is illustrated in Fig. 12(b) where $B = B_\phi$. Although the plots are oscillating, the expected trend is seen, and at later times, when turbulence is fully developed, convergence is worse and at times lost.

As turbulence affects the dynamics of the field, and affects the convergence of our results, we use the spectrum of the turbulence itself as a diagnostic for convergence. We have already analysed the spectrum for our higher resolution simulations in the previous sections, and found it to be consistent with a Kolmogorov spectrum.
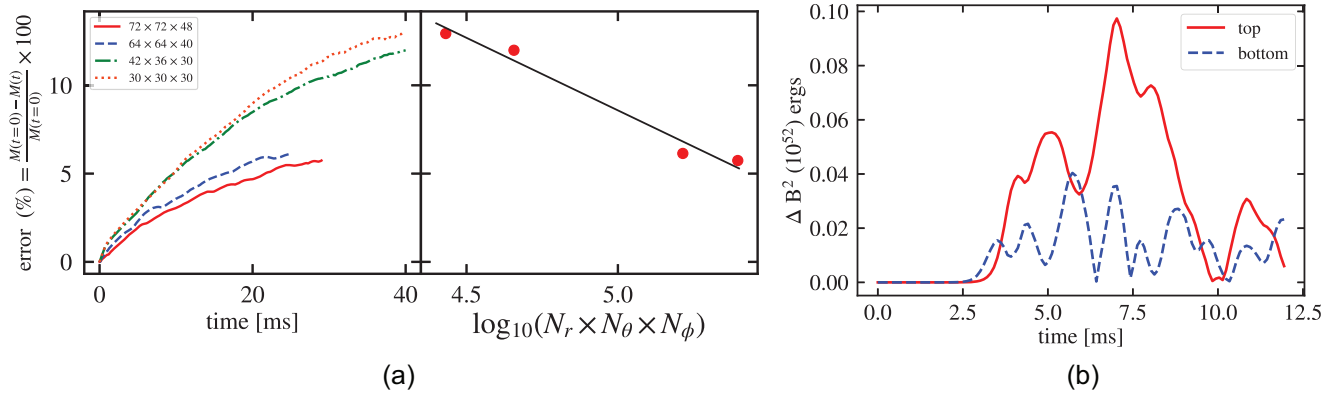
Figure 12. (a) Error in the total mass of the star as a function of (left-hand panel) time, and (right-hand panel) resolution for our purely poloidal setup with $B_{\rm p} = 10^{17}$ G. The curves are incomplete for higher resolution setups as the simulation hit the wall clock time. (b) Difference in B_ϕ^2 plotted as a function of time. The red curve (top panel) shows the difference in energies between our setups with resolution $64 \times 64 \times 40$ and $30 \times 30 \times 30$. The blue curve (bottom panel) shows the difference in energies between our setups with resolution $72 \times 72 \times 48$ and $64 \times 64 \times 40$.
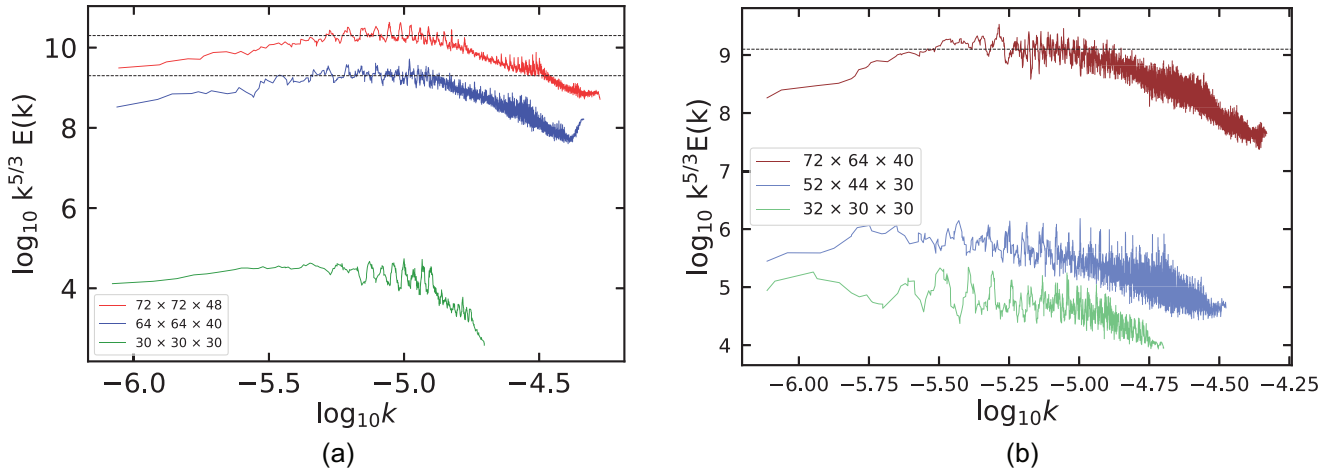

Figure 13. (a) Kolmogorov spectrum plotted for our non-resistive setup with varying resolution. According to Classical Kolmogorov theory, the spectrum follows $E(k) \propto k^{-5/3}$ in the inertial range, and deviate for high and low values of k where energy is injected and dissipated. We multiply $E(k)$ by $k^{5/3}$ and therefore expect to obtain a flat spectrum in the inertial range for the Kolmogorov case. This is seen in the region between $k = (10^{-5.25}, 10^{-4.9})$ for our highest resolution simulation (the black dotted lines are for reference). (b) Kolmogorov spectrum plotted for different resolutions for resistive atmosphere setup. Although the spectra are noisy, a Kolmogorov like dependence is visible in both the setups.

In Figs 13(a) and (b), we plot the kinetic energy spectrum for varying resolutions as a sanity check of the convergence of the code. As can be seen, the spectrum extends to smaller scales as expected, and is consistent with the scaling of

$$E(k) \propto k^{-5/3} \qquad (22)$$

over a larger portion of parameter space, indicating that our higher resolution simulations are increasingly capturing the true dynamics of the system.

7 CONCLUSIONS AND DISCUSSIONS

In this paper, we have presented the results of 3D MHD simulations of magnetic field configurations in NSs. We have considered both ideal MHD and a setup with a resistive atmosphere, and assume the field to be dipolar at the exterior boundary far from the star. We do not consider the effect of the crust, or of superfluidity in the interior. Our results are thus applicable to the first few hours of life of the star, after differential rotation is dissipated. The field configurations we obtain are then 'frozen in' as the star cools, and may be sued

as initial conditions for longer term simulations, on time-scales of 10^3–10^5 yr, where the evolution of the field is driven by effects such as the Hall effect in the crust, Ohmic decay, and ambipolar diffusion.

We have studied the evolution of both initially purely poloidal and mixed poloidal–toroidal fields with stronger toroidal components, and find that in all cases the initial configuration is unstable, with the instability developing on the order of an Alfvén crossing time-scale. As the instability develops it gives rise to turbulence, and drives a small scale dynamo, which transfers helicity to the large-scale field. The field attends a complex geometry with the toroidal component contributing $E_{\rm tor} \leq 20$ per cent of $E_{\rm m, tot}$ in all setups, and while this is not a strict equilibrium, the ratio of the poloidal to toroidal energies in the field is approximately stable. The turbulence is not observed to decay during our simulations.

We find that stronger resistivity triggers the instability faster, but does not impact its non-linear saturation, thus modifying only the time-scales in our simulation. We also found that the extent of the atmosphere does not play any role in the overall equilibrium of the system, and the results do not change if we push the boundary of our

simulation farther out, from 1.2 to 2 stellar radii. Our results show that the field does not decay unlike the works of Braithwaite & Spruit (2006) and Mitchell et al. (2015). Our choice of fixed boundary conditions could play a major role here and thus future studies will be aimed at understanding this scenario better.

Overall, we find that an NS with a given inferred dipolar field strength far from the surface, is likely to harbour an interior toroidal component with an average energy of roughly 25 per cent of the poloidal component, but that stronger toroidal fields are unstable and cannot be sustained. The overall geometry of the field is, however, complex, with higher multipoles growing closer to the surface, and moreover non-stationary over the lifetime of our simulations. We find rather a turbulent quasi-equilibrium, in which only average quantities are roughly constant. Further studies will focus on the decay of the turbulence and on quantifying the impact of these results on attempts to measure the mass and radius of an NS with X-ray observations from NICER, for which the background field configuration is an important ingredient (Bilous et al. 2019; Miller et al. 2019; Riley et al. 2019).

ACKNOWLEDGEMENTS

REFERENCES

Akgün T., Reisenegger A., Mastrano A., Marchant P., 2013, MNRAS, 433, 2445

Andersson N., Sidery T., Comer G. L., 2007, MNRAS, 381, 747

Armaza C., Reisenegger A., Valdivia J. A., 2015, ApJ, 802, 121

Barrera R. G., Estevez G. A., Giraldo J., 1985, Eur. J. Phys., 6, 287

Bilous A. V. et al., 2019, ApJ, 887, L23

Biskamp D., 2003, Magnetohydrodynamic Turbulence. Cambridge University Press, Cambridge

Bocquet M., Bonazzola S., Gourgoulhon E., Novak J., 1995, A&A, 301, 757

Braithwaite J., 2007, Astron. Astrophys., 469, 275

Braithwaite J., 2008, MNRAS, 386, 1947

Braithwaite J., Nordlund A., 2006, Astron. Astrophys., 450, 1077

Braithwaite J., Spruit H. C., 2006, Astron. Astrophys., 450, 1097

Chandrasekhar S., Fermi E., 1953, ApJ, 118, 116

Chung C. T. Y., Melatos A., 2011a, MNRAS, 411, 2471

Chung C. T. Y., Melatos A., 2011b, MNRAS, 415, 1703

Ciolfi R., Rezzolla L., 2012, ApJ, 760, 1

Ciolfi R., Rezzolla L., 2013, MNRAS, 435, L43

Ciolfi R., Ferrari V., Gualtieri L., 2010, Mon. Not. Roy. Astron. Soc., 406, 2540

Ciolfi R., Lander S. K., Manca G. M., Rezzolla L., 2011, Astrophys. J., 736, L6

Cutler C., 2002, Phys. Rev. D, 66, 084025

de Lima R. C. R., Coelho J. G., Pereira J. P., Rodrigues C. V., Rueda J. A., 2020, ApJ, 889, 165

Ferraro V. C. A., 1954, ApJ, 119, 407

Flowers E., Ruderman M. A., 1977, ApJ, 215, 302

Frederick S. G., Kuchera M. P., Thompson K. L., 2020, preprint (arXiv: 2002.02619)

Frisch U., Pouquet A., Léorat J., Mazure A., 1975, J. Fluid Mech., 68, 769

Glampedakis K., Lasky P. D., 2015, MNRAS, 450, 1638

Glampedakis K., Lasky P. D., 2016, MNRAS, 463, 2542

Glampedakis K., Andersson N., Lander S. K., 2012, MNRAS, 420, 1263

Goldreich P., Julian W. H., 1969, ApJ, 157, 869

Goldreich P., Reisenegger A., 1992, ApJ, 395, 250

Güver T., Göğüş E., Özel F., 2011, MNRAS, 418, 2773

Haskell B., Samuelsson L., Glampedakis K., Andersson N., 2008, Mon. Not. Roy. Astron. Soc., 385, 531

Herbrik M., Kokkotas K. D., 2017, MNRAS, 466, 1330

Iroshnikov P. S., 1964, Soviet Ast., 7, 566

Kiuchi K., Yoshida S., 2008, Phys. Rev. D, 78, 044045

Kolmogorov A., 1941, Akademiia Nauk SSSR Doklady, 30, 301

Kraichnan R. H., 1965, Phys. Fluids, 8, 1385

Lander S., Jones D., 2009, MNRAS, 395, 2162

Lander S., Jones D., 2011, MNRAS, 412, 1730

Lander S. K., Jones D. I., 2012, MNRAS, 424, 482

Lander S. K., Jones D. I., 2018, MNRAS, 481, 4169

Lander S. K., Jones D. I., 2019, MNRAS, 494, 4838

Lander S., Jones D., Passamonti A., 2010, MNRAS, 405, 318

Lasky P. D., 2015, PASA, 32, e034

Lasky P. D., Melatos A., 2013, Phys. Rev. D, 88, 103005

Lasky P. D., Zink B., Kokkotas K. D., Glampedakis K., 2011, Astrophys. J., 735, L20

Lasky P. D., Zink B., Kokkotas K. D., 2012, preprint (arXiv:1203.3590)

Lites B. W. et al., 2008, ApJ, 672, 1237

Markey P., Tayler R. J., 1973, MNRAS, 163, 77

Markey P., Tayler R. J., 1974, MNRAS, 168, 505

Mignone A., Bodo G., Massaglia S., Matsakos T., Tesileanu O., Zanni C., 2007, Astrophys. J. Suppl., 170, 228

Miller M. C. et al., 2019, ApJ, 887, L24

Mitchell J. P., Braithwaite J., Reisenegger A., Spruit H., Valdivia J. A., Langer N., 2015, MNRAS, 447, 1213

Monaghan J. J., 1965, MNRAS, 131, 105

Peralta C., Melatos A., Giacobello M., Ooi A., 2006, ApJ, 651, 1079

Philippov A. A., Spitkovsky A., 2018, ApJ, 855, 94

Pili A. G., Bucciantini N., Del Zanna L., 2014, MNRAS, 439, 3541

Pili A. G., Bucciantini N., Del Zanna L., 2017, MNRAS, 470, 2469

Pons J. A., Geppert U., 2007, A&A, 470, 303

Pons J. A., Viganò D., 2019, Living Rev. Comput. Astrophys., 5, 3

Reisenegger A., 2009, A&A, 499, 557

Riley T. E. et al., 2019, ApJ, 887, L21

Roxburgh I. W., 1966, MNRAS, 132, 347

Siegel D. M., Ciolfi R., Harte A. I., Rezzolla L., 2013, Phys. Rev. D, 87, 121302

Spitkovsky A., 2006, ApJ, 648, L51

Tayler R. J., 1957, Proc. Phys. Soc. B, 70, 31

Tayler R. J., 1973, MNRAS, 161, 365

Thompson C., Duncan R. C., 1993, ApJ, 408, 194

Thompson C., Duncan R. C., 1996, ApJ, 473, 322

Wareing C. J., Hollerbach R., 2009, A&A, 508, L39

Wright G. A. E., 1973, MNRAS, 162, 339

Zink B., Stergioulas N., Hawke I., Ott C. D., Schnetter E., Müller E., 2007, Phys. Rev. D, 76, 024019

This paper has been typeset from a TeX/LaTeX file prepared by the author.

Author contributions statements

Contributions:

Ankan Sur: I have performed all simulations, produced analysis scripts, produced figures, and contributed to writing the paper. My contribution to this article is 75%.

Ankan Sur
_____
Ankan Sur

Brynmor Haskell: I have guided the work and made important contributions to the writing and interpretation of results. My contribution to this article is 20%.

Byra
_____
Brynmor Haskell

Emily Kuhn: I worked on implementing the equation of state used in the simulations and proofread the manuscript. My contribution to this article is 5%.

Emily Kuhn
_____
Emily Kuhn

Long-term general relativistic magnetohydrodynamics simulations of magnetic field in isolated neutron stars

"When you change the way you look at things, the things you look at change."

-Max Planck.

Long-term general relativistic magnetohydrodynamics simulations of magnetic field in isolated neutron stars

Ankan Sur [,1]★ William Cook,[2] David Radice,[3,4,5] Brynmor Haskell[1] and Sebastiano Bernuzzi [2]

[1]*Nicolaus Copernicus Astronomical Center, Polish Academy of Sciences, Bartycka 18, PL-00-716 Warsaw, Poland*
[2]*Theoretisch-Physikalisches Institut, Friedrich-Schiller-Universität Jena, D-07743 Jena, Germany*
[3]*Institute for Gravitation and the Cosmos, The Pennsylvania State University, University Park, PA 16802, USA*
[4]*Department of Physics, The Pennsylvania State University, University Park, PA 16802, USA*
[5]*Department of Astronomy and Astrophysics, The Pennsylvania State University, University Park, PA 16802, USA*

ABSTRACT

Strong magnetic fields play an important role in powering the emission of neutron stars. Nevertheless, a full understanding of the interior configuration of the field remains elusive. In this work, we present general relativistic magnetohydrodynamics (MHD) simulations of the magnetic field evolution in neutron stars lasting $\sim$880 ms ($\sim$6.5 Alfvén crossing periods) and up to resolutions of 0.1155 km using ATHENA++. We explore two different initial conditions, one with purely poloidal magnetic field and the other with a dominant toroidal component, and study the poloidal and toroidal field energies, the growth times of the various instability-driven oscillation modes, and turbulence. We find that the purely poloidal setup generates a toroidal field, which later decays exponentially reaching 1 per cent of the total magnetic energy, showing no evidence of reaching equilibrium. The initially stronger toroidal field setup, on the other hand, loses up to 20 per cent of toroidal energy and maintains this state till the end of our simulation. We also explore the hypothesis, drawn from previous MHD simulations, that turbulence plays an important role in the quasi-equilibrium state. An analysis of the spectra in our higher resolution setups reveals, however, that in most cases we are not observing turbulence at small scales, but rather a noisy velocity field inside the star. We also observe that the majority of the magnetic energy gets dissipated as heat increasing the internal energy of the star, while a small fraction gets radiated away as electromagnetic radiation.

Key words: instabilities – magnetic fields – methods: numerical – stars: neutron.

1 INTRODUCTION

Harbouring the strongest magnetic fields in the universe with core densities exceeding that of nuclear matter, neutron stars (NSs) provide a laboratory for studying physics at extreme conditions, which are not reproducible with the current available technologies on Earth. The surface magnetic field (B_s) of NSs is generally inferred from the dipole spin-down using radio astronomical data (Chung & Melatos 2011a,b) and has allowed us to classify these systems into old recycled pulsars with $B_s \sim 10^8$ G, ordinary pulsars with $B_s \sim 10^{12}$ G, and magnetars with $B_s \sim 10^{15}$ G. Alternatively, the geometry of the magnetic field and its strength had been derived from X-ray emitting hotspots in pulsar PSR-J001X (Bilous et al. 2019). This study (see also de Lima et al. 2020) suggests that the field is far from the conventional dipolar geometry, but rather favours a multipolar magnetic field or an offset dipole.

The magnetic field of pulsars plays an important role in accelerating charged particles in the magnetospheres, which emit electromagnetic radiation, and allows us to study its properties, for example, spin-down due to magnetic dipole radiation. The energy from differential rotation can be converted to a large-scale

magnetic field, which in turn can help in launching powerful jets from newly formed NSs (Moiseenko, Bisnovatyi-Kogan & Ardeljan 2006; Shibata et al. 2006; Burrows et al. 2007; Mösta et al. 2014). It has been observed that this magnetic field remains stable on a longer time-scale comparable to the lifetime of NSs except that of magnetic flares emitted by magnetars, which operate on a very short time-scale. This provokes the quest to understand what leads to the magnetic field stability. Although there is evidence of an exponential decay of the field through Ohmic dissipation, the time-scale responsible for this mechanism (Ostriker & Gunn 1969) is greater than the Hubble time. In other words, there is no significant decay that changes the magnetic field effectively (Kraav, Gusakov & Kantor 2021).

An arbitrary magnetic field is generally not in equilibrium when the Lorentz force and pressure forces do not balance one another. It had been long established that certain equilibrium configurations, like a purely poloidal or a purely toroidal field, are unstable and subjected to 'kink' instability acting within a few Alfvén time-scales (Tayler 1957, 1973; Markey & Tayler 1973, 1974; Wright 1973; Flowers & Ruderman 1977). Analytical (Haskell et al. 2008; Ciolfi et al. 2009; Ciolfi, Ferrari & Gualtieri 2010; Gusakov, Kantor & Ofengeim 2017; Ofengeim & Gusakov 2018) and numerical simulations including Newtonian magnetohydrodynamics (MHD; Braithwaite & Nordlund 2006; Braithwaite & Spruit 2006; Braithwaite 2007; Lander & Jones 2009, 2011; Lander, Jones & Passamonti 2010; Herbrik & Kokkotas

---

★ E-mail: ankansur@camk.edu.pl

2017; Frederick, Kuchera & Thompson 2020; Sur, Haskell & Kuhn 2020) and general relativistic (GR) MHD (Kiuchi & Yoshida 2008; Ciolfi et al. 2011; Lasky et al. 2011; Ciolfi & Rezzolla 2013; Pili, Bucciantini & Del Zanna 2014, 2017) have confirmed this explicitly where a stable stellar field needs both poloidal and toroidal components. The instability gives rise to various azimuthal oscillation modes responsible for driving gravitational radiation from the system. Estimating the relative strength of the poloidal and toroidal components is also important in virtue of studying continuous gravitational waves (GWs) emitted by NSs, caused by magnetic deformation (Bonazzola & Gourgoulhon 1996; Cutler 2002; Frieben & Rezzolla 2012), as it depends sensitively on the amount of magnetic field energy stored in each of its components.

The most favoured magnetic field geometry pertinent to NSs is that of a 'twisted torus' where the poloidal field lines thread the interior of the star and close inside. Outside the star, the field lines extend until infinity with the field being continuous at the stellar surface. This implies the absence of surface currents. The toroidal field is concentrated as a flux tube within this closed poloidal field line located at approximately 0.8 times the stellar radii. This geometry had been found by time-evolving random initial configurations from MHD simulations (Braithwaite & Nordlund 2006).

Understanding equilibria requires us to solve the so-called Grad–Shafranov equation, which yields various magnetic field configurations with varying poloidal and toroidal field energies (Lander & Jones 2009; Ciolfi & Rezzolla 2012, 2013; Gourgouliatos et al. 2013; Armaza, Reisenegger & Valdivia 2015; Sur & Haskell 2021). However, these solutions do not tell us anything about the stability of the magnetic field with time. Studies with an axisymmetric field in the crust have been performed to show the presence of Hall equilibrium states (Hollerbach & Rüdiger 2002; Cumming, Arras & Zweibel 2004; Gourgouliatos & Cumming 2014a,b). The Hall effect leads to the formation of small-scale magnetic features, which dissipates to power the thermal radiation, e.g. in magnetars, when a toroidal magnetic field of strength 10^{16} G is present inside the crust (Pons & Perna 2011; Geppert & Viganò 2014; Gourgouliatos, Wood & Hollerbach 2016). The Hall effect also leads to the growth of dipole moment of a quadrupolar toroidal component in the NS crust, which could explain the observed braking indices of young pulsars (Gourgouliatos & Cumming 2015). Further, long-term evolution of the magnetic field in the crust of NSs under the Hall effect and Ohmic dissipation has shown the presence of a 'Hall attractor' state, which for an initially dipole dominated field also has an octupolar component and an energetically negligible quadrupole toroidal field.

Due to the lack of direct observational evidence of the internal magnetic field topology, our knowledge on the distribution of magnetic energy in the poloidal and toroidal components is limited to simulations. It had been shown that about 80–90 per cent of the total magnetic energy is stored within the poloidal component from MHD simulations with either a purely initial poloidal field or from a mixed field with a stronger toroidal component (Sur et al. 2020). However, equilibrium calculations by Ciolfi & Rezzolla (2013) have shown to produce a toroidal field energy 90 per cent of the total internal magnetic energy with a suitable choice of the azimuthal currents. Whether these models are realistic demands future studies not only to validate their stability, but also for a better understanding of emission properties from NSs. Another interesting finding by Sur et al. (2020) is that NSs experience turbulence triggered by the initial perturbations to the field. It had been shown that this turbulence gives rise to an inverse cascade in magnetic helicity (H_m), which determines the 'twist' of the magnetic field lines. Thus, energy is transferred from small resistive scales to large eddies. Further, the conservation of H_m

is broken as the field rearranges and attends stability. It was found that the energy spectra followed Kolmogorov's law with a scaling $-5/3$, but the data were noisy owing to limited resolution using the spherical coordinate system. These simulations studied the first 40 ms of magnetic field evolution. We try to understand turbulence at late times $t > 100$ ms for which we need longer simulations with higher resolution. Moreover, the magnetic field geometry can be used as various background models in other studies like post-merger Binary Neutron Star (BNS) simulations in which the magnetic field is either responsible for a strong baryonic wind (Ciolfi & Kalinani 2020) or responsible for jet formation, powering kilonova transients and GW emission (Ciolfi 2020).

In this study, we perform non-linear GRMHD simulations for a fiducial NS of mass $1.4\,M_\odot$ using the code ATHENA++ as described in Section 2. The results of the simulations are presented in Section 3, which are some of the longest in terms of evolution time and hence give us further insights on what happens to the magnetic field energy and its structure at later times. We also investigate the relativistic effects of turbulence and energy cascades and seek answers to the question on whether the turbulent feature persists in NS simulations. Finally, the conclusions and discussions are presented in Section 4.

2 METHOD

To study the evolution of the magnetized star, we perform numerical simulations using the GRMHD code ATHENA++ (Stone et al. 2020). We evolve the GRMHD equations without resistivity on a fixed background metric (i.e. in the Cowling approximation) of a non-rotating star. ATHENA++ uses a constrained transport algorithm to evolve the magnetic field, detailed in White, Stone & Gammie (2016). Evolutions are performed using the local Lax–Friedrichs flux, with reconstruction performed in the primitive variables following an implementation of the piecewise parabolic method detailed in Felker & Stone (2018). During the simulation, primitive variables are recovered from the conservative variables by implementing the conservative to primitive inversion algorithm described in Noble et al. (2006).

Initial data for the geometry and matter are constructed by the numerical solution of the Tolmann–Oppenheimer–Volkoff equations for a spherically symmetric fluid distribution for the interior of the star coupled with an equation of state (EOS) in the form $p(\rho)$ that connects the pressure to the rest-mass density. The exterior is set to the Schwarzschild metric. The fiducial NS has a mass of $1.4\,M_\odot$ and a radius of $R \sim 10$ km. The initial data EOS is set to

$$p = K\rho^\Gamma \tag{1}$$

with $K = 100$, $\Gamma = 2$; the Γ-law EOS,

$$p = (\Gamma - 1)\rho\epsilon, \tag{2}$$

where ϵ is the specific internal energy, is used during the evolution.

The initial poloidal magnetic field configuration is given by the vector potential

$$A_x = -y A_\varphi \tag{3}$$

$$A_y = x A_\varphi \tag{4}$$

$$A_z = 0 \tag{5}$$

$$A_\varphi = A_b \max(p - p_{thr}, 0) \tag{6}$$

$$p_{thr} = 0.04 p_{max} \tag{7}$$

following Liu et al. ([2008](#)), where p_{max} is the maximum value of the pressure within the star. The parameter A_b controls the magnitude of the magnetic field and is set to obtain a maximum value of 3.54×10^{16} G inside the star. The initial toroidal magnetic field is initialized directly on the magnetic field components to be

$$B_x = -\hat{y} B_{tor} \max(p - p_{thr}, 0), \tag{8}$$

$$B_y = \hat{x} B_{tor} \max(p - p_{thr}, 0), \tag{9}$$

$$B_z = 0. \tag{10}$$

In the case of the toroidal simulations in this paper, B_{tor} is set to give the same maximum field strength as in the poloidal case. In addition, a weak poloidal field is superimposed on top of this toroidal field, with parameter A_b set 50 times smaller than in the purely poloidal case. Evolutions are performed in unigrid without symmetry, with an outer boundary set at 30 km. We use outflow boundary conditions, which do not affect the dynamics in the interior of the star; however, it affects the dynamics at the outer edge of our simulation box. We perform runs at four resolutions corresponding to 64^3, 128^3, 256^3, and 512^3 grid points across the computational domain. These give grid spacings of 0.923 , 0.462, 0.231 , and 0.115 km, respectively. Our highest resolution run 512^3 has an evolution time of 89 ms, whereas the setup ps256 has an evolution time of 880 ms. In the exterior of the star, an atmosphere is set with rest-mass density $\rho_{atm} = 10^{-10} \max(\rho)$. Any cells with density falling below a threshold value of $\rho_{thr} = 100 \rho_{atm}$ are identified as atmosphere and set to ρ_{atm}, with the fluid velocity set to 0 and the pressure fixed using the EOS. In the atmosphere, the magnetic field components remain unrestricted. We use the following nomenclature when referring to the different resolution setups. The initially purely poloidal magnetic field setup is denoted by pS???, where ??? represents the number of grid points. Thus, the setup pS256 corresponds to a purely poloidal initial field run with a numerical box of 256^3 grid points. Similarly, the initially stronger toroidal field setup is denoted by tS???, where again ??? represents the number of grid points.

3 RESULTS

The evolution of the magnetic field occurs on a characteristic time-scale associated with the system, called the Alfvén crossing time, which is given by

$$\tau_A = \frac{2R\sqrt{4\pi\langle\rho\rangle}}{\langle B \rangle}, \tag{11}$$

where $\langle \dots \rangle$ represents volume-averaged quantities. For $\langle B \rangle \sim 4.5 \times 10^{15}$ G, we obtain $\tau_A \sim 12$ ms. Theoretically, we should expect the field to rearrange itself at this time, as we shall see it indeed does in our simulations. As $\langle B \rangle$ evolves with time, the time-scale defined in equation (11) will vary. Because of this, we use the following definition of Alfvén crossing period:

$$T_A = \int_0^t \frac{dt}{\tau_A(t)}. \tag{12}$$

The above definition means that we are rescaling our evolution time with the Alfvén crossing time. Hence, a value of $T_A = 1$ means an evolution time equivalent to $1\tau_A$, $T_A = 2$ is equivalent to $2\tau_A$, and so on. An evolution time of 880 ms corresponds to $\sim 6.5\, T_A$ for our setup pS256; however, T_A changes for the different resolution setups depending on how much magnetic energy is lost and how the density changes with time.

3.1 Magnetic field lines and energies

We discuss the purely poloidal initial field first. The *neutral* line corresponds to the region where the magnetic field vanishes inside the star. Snapshots of the three-dimensional (3D) view of the magnetic field lines are shown in Fig. [1](#) at different times 2.0 (left-hand panel), 12 (middle panel), and 49 ms (right-hand panel), respectively. We also show 2D projections of the field lines on the *x–y* plane (equatorial view) and the *x–z* plane (meridional view) in Fig. [2](#) with the title representing different time stamps. The colour scale gives the strength of the toroidal component in Gauss. During the start of evolution, the field lines first change their cross-sectional area, which corresponds to the so-called varicose mode. This is followed by the transverse displacement of the fluid along the neutral line, which leads to the development of the 'kink' instability (Lander & Jones [2011](#); Lasky et al. [2011](#); Lasky, Zink & Kokkotas [2012](#)) as shown in Fig. [1](#) (bottom row, centre image).

The saturation of this instability modifies the magnetic field as expected: The initial axisymmetry in the system is replaced by a non-axisymmetric structure. The toroidal field initially starts appearing on the boundary of the star along the $x = 0$ and $y = 0$ axes. This is an artefact of the Cartesian grid and the presence of sharp density gradients across the stellar surface at $R = 10$ km. Similar features have also been noted in past studies (Lasky et al. [2011](#)) and depend strongly on the resolution of our setup, since these toroidal areas become considerably smaller with higher resolution. The toroidal field grows exponentially from the initial state until $t \sim 12$ ms ($T_A \sim 1$) appearing not only within the closed field regions inside the star, but also outside it, which might be caused by the aforementioned artefact. The toroidal field strength at this point is comparable to the poloidal field (see the middle panel of Fig. [2](#)). From the equatorial view, we see that the field lines create vortex-like structures (see the right-hand panel) owing to the conservation of magnetic helicity. From $t = 12$ ms, the evolution proceeds with non-linear rearrangement of the field, where not only the closed field lines are involved, but also the whole star and the open field lines. The equatorial 3D view (right-hand panel) shows the already formed toroidal component. The evolution of the field occurs slowly in which the interior closed field lines move outwards losing energy in the toroidal component. We shall see this in more detail when discussing the energies of the poloidal and toroidal components later in this section. The modifications of the field also expel matter from the star; however, the change in rest mass ($\Delta M_{rest} \approx 10^{-5}$ M$_\odot$) is much slower as compared to the changes in magnetic field energy during the first Alfvén crossing time. The extent to which the field modifies obviously depends on the magnetic field strength with stronger fields having more violent dynamics and vice versa (Ciolfi & Rezzolla [2012](#)). From the end state of our simulation, we conclude that the geometry of the magnetic field is significantly different and has left no trace of its initial configuration. Although we do not have resistivity, there is numerical dissipation from our grid, and it is difficult to understand whether the post-instability configuration is stable. However, the time-scale on which other quantities such as the rest mass of the star are changing is much longer than the instability of the magnetic field. We can conclude that this configuration is not a 'strict' equilibrium but rather a 'quasi-stationary' equilibrium.

The magnetic flux decays in the interior as well as in the exterior of the star due to the rearrangement of the field, which is a physical effect and not a numerical artefact as also seen in Braithwaite & Spruit ([2006](#)). We recall that our setup includes an MHD fluid ball with an atmosphere with no solid crust being present. This has important consequences for the magnetic field evolution both inside
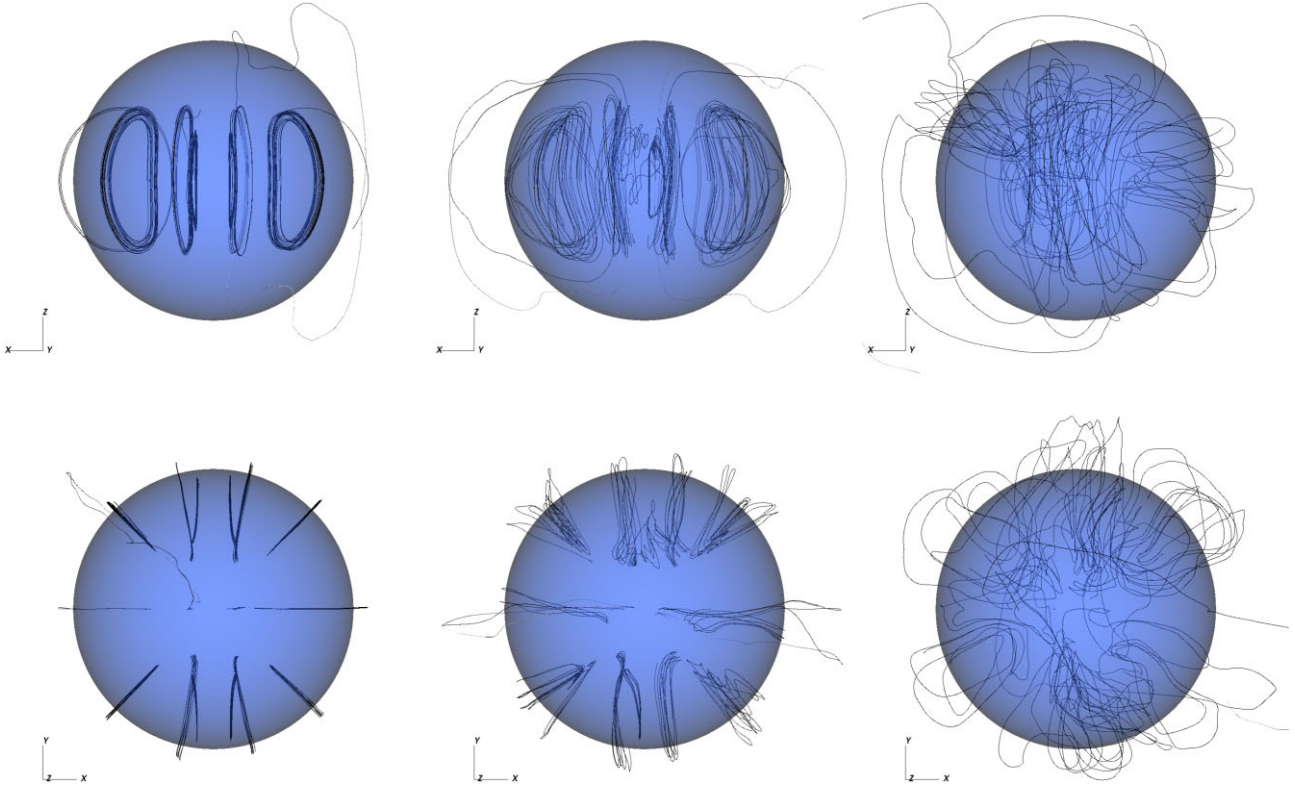
Figure 1. 3D view of the magnetic field for ps256 at three different times, $t = 2$ ($T_A \sim 0.1$), 12.7 ($T_A \sim 0.8$), and 49 ms ($T_A \sim 2$). The definition of T_A is given by equation (12). The top row shows the meridional view, while the bottom row shows the equatorial view.
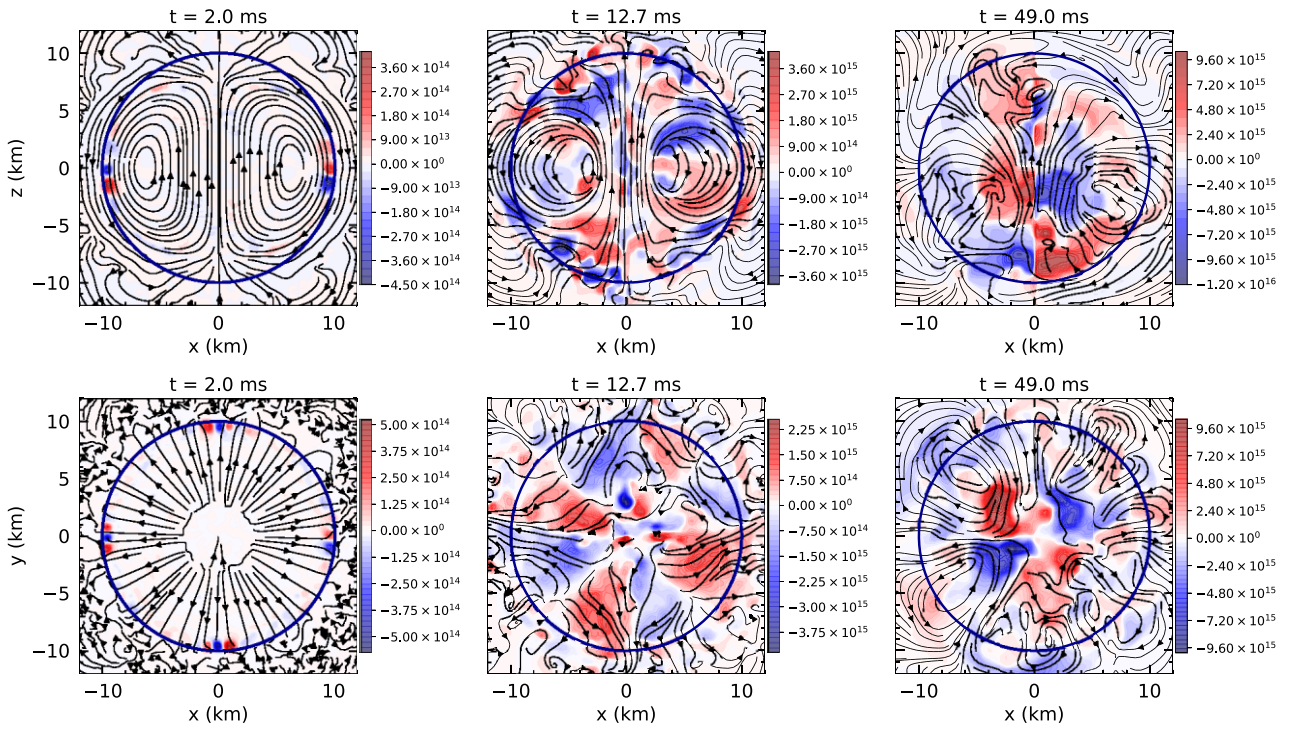

Figure 2. 2D projection of the field lines for the setup pS256 on the *x*–*z* plane (top row) and the *x*–*y* plane (bottom row) at the three different times, $t = 2$ ($T_A \sim 0.1$), 12.7 ($T_A \sim 0.8$), and 49 ms ($T_A \sim 2$), as shown in Fig. 1. The colour scale represents the strength of the toroidal field in Gauss.
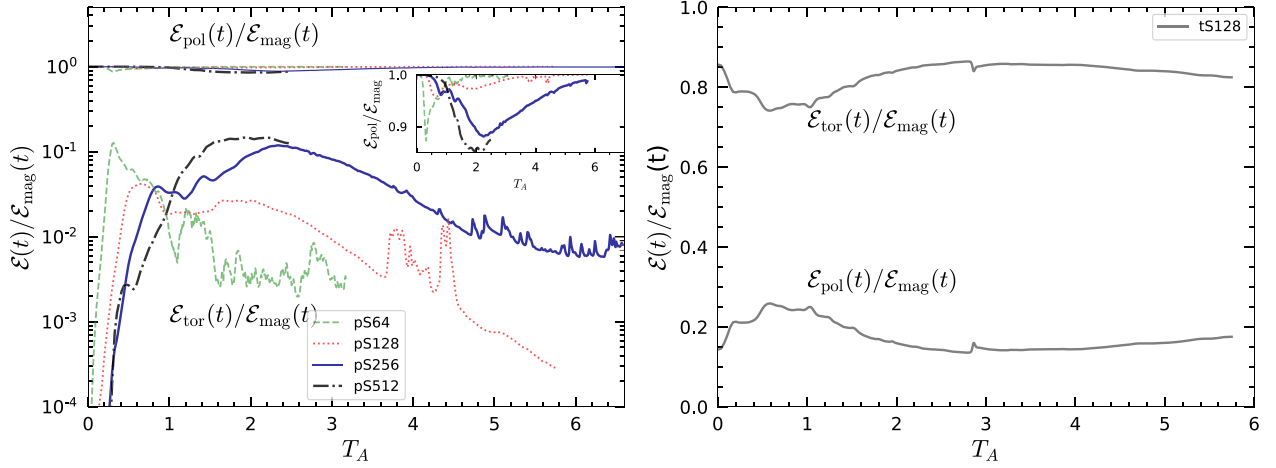
Figure 3. Ratio of poloidal and toroidal energies to the total magnetic energy at each Alfvén time for purely poloidally dominated initial condition (left-hand panel) and toroidally dominated initial condition (right-hand panel).

and outside the star. We also do not have resistive MHD effects such as magnetic reconnection. Including these effects, we would expect powerful outbursts from the atmospheric emission originating from sudden rapid rearrangement of the field. Thompson & Duncan (1995) proposed that a large-scale reconnection/interchange instability of the magnetic field caused the 1979 March 5 burst event and that cracking of the NS crust produced soft gamma repeaters. Magnetic field decay could also build stresses in the NS crust and cause it to break due to a strong toroidal field, resulting in crustquakes. Magnetar giant flares may likely be explained by such a phenomenon (Lander et al. 2015).

Fig. 3 shows the time evolution of the poloidal ($\mathcal{E}_{pol}$) and toroidal energies ($\mathcal{E}_{tor}$) calculated over the volume of the star defined as

$$\mathcal{E}_{pol} = \int_{star} (b_P^2 u_\mu u^\nu + \frac{b_P^2}{2} g_\mu{}^\nu) \delta_t^\mu n_\nu d^3 \boldsymbol{x} \sqrt{-g}, \tag{13}$$

$$\mathcal{E}_{tor} = \int_{star} (b_T^2 u_\mu u^\nu + \frac{b_T^2}{2} g_\mu{}^\nu) \delta_t^\mu n_\nu d^3 \boldsymbol{x} \sqrt{-g},$$

where $b_P^\mu + b_T^\mu = b^\mu$ is magnetic field components projected into a space normal to the fluid four-velocity u^μ, n_μ is the normal observer's four-velocity, $g_{\mu\nu}$ is the metric, and $\sqrt{-g} = \alpha\sqrt{\gamma}$ is the determinant of the metric tensor. The magnitude of the toroidal field is given by

$$b_T = \sqrt{g_{xx}} \frac{(xb^y - yb^x)}{\sqrt{x^2 + y^2}}, \tag{14}$$

where x, y are the Cartesian axes.

We compute various energy integrals whose definitions are given in Appendix A, while the definitions of the different physical variables can be found in Noble et al. (2006). Initially, at $t = 0$, we have the entire magnetic energy stored within the poloidal component. For pS256, we find that the toroidal energy rises at $t = 60$ ms ($\sim 2T_A$) where $\mathcal{E}_{tor} \sim 0.2\mathcal{E}_{mag}$ (left-hand panel of Fig. 3). However, as the system loses magnetic energy, the toroidal component gets weaker, and at much later times $t \sim 880$ ms ($\sim 6.5T_A$), it approximately becomes 1 per cent of $\mathcal{E}_{mag}$. The evolution shows that the toroidal field attains a quasi-stable equilibrium with energies similar to the ones obtained from solving the Grad–Shafranov equation (see e.g. Lander & Jones 2009; Armaza et al. 2015; Sur & Haskell 2021), which gives equilibrium solutions but does not say anything about the stability of these equilibrium fields. The star continues to lose energy till the end of our simulation, but the ratio of poloidal and toroidal

energies to the total magnetic energy is seen to settle at a quasi-equilibrium value for pS64 and pS256 but not in pS128 (left-hand panel of Fig. 3). In our setup, pS512, we have a shorter evolution time, $T_A \sim 2.5$, and need a much longer evolution to understand if it reaches equilibrium. The toroidal field in this case grows up to 20 per cent of the total magnetic energy, which is achieved at $2T_A$. From this point, although we do not have results for further evolution, its strength seems to decrease and we may fail to achieve convergence as also seen in our different setups in the later stages of evolution. For tS128 (see the right-hand panel of Fig. 3), we initially have a larger toroidal component, which at first loses some energy and increases the strength of the poloidal component. However, this soon becomes stronger with time and the poloidal component also stabilizes at $\mathcal{E}_{pol} \approx 0.2\mathcal{E}_{mag}$. Note that this is different than what was observed in Sur et al. (2020), where the toroidal energy decayed to get stabilized at 10 per cent of $\mathcal{E}_{mag}$. This may be caused due to the implementation of the boundary conditions of the magnetic field. In Sur et al. (2020), we used a periodic boundary in the azimuthal direction, while the radial and angular boundaries were fixed at their dipolar poloidal values. Since we have a free boundary in this setup, the toroidal field gets stabilized by a weaker poloidal component.

Let us now discuss the dynamics at the initial stage of the evolution. The poloidal field energy remains unchanged up until 12 ms ($\sim 1T_A$). During this time, the toroidal field undergoes an exponential growth, and after $\sim 1T_A$, the instability saturates and the field continues to evolve less dramatically. This behaviour depends on the initial strength of the magnetic field (Ciolfi & Rezzolla 2012) and the resolution of our numerical grid; however, it is evident that the poloidal energy undergoes this sharp decrease when the instability saturates and the non-linear rearrangement of the field starts. The poloidal and toroidal energies (normalized by the initial magnetic energy at $t = 0$) shown in the left-hand panel of Fig. 4 are in good agreement with Ciolfi & Rezzolla (2012) till the end of their simulation time $t \sim 60$ ms. We have much longer runs in which we see that the component energies continue to decay, both for the poloidally dominated setup (left-hand panel in Fig. 4) and the toroidally dominated setup (see the middle panel of Fig. 4). The ratio of toroidal to poloidal energies (right-hand panel of Fig. 4) also shows that for pS128 and pS64, the field oscillates and dissipates more energy when compared to pS256, where the energy loss is more continuous. This ratio for the setup pS512 reaches 20 per cent at
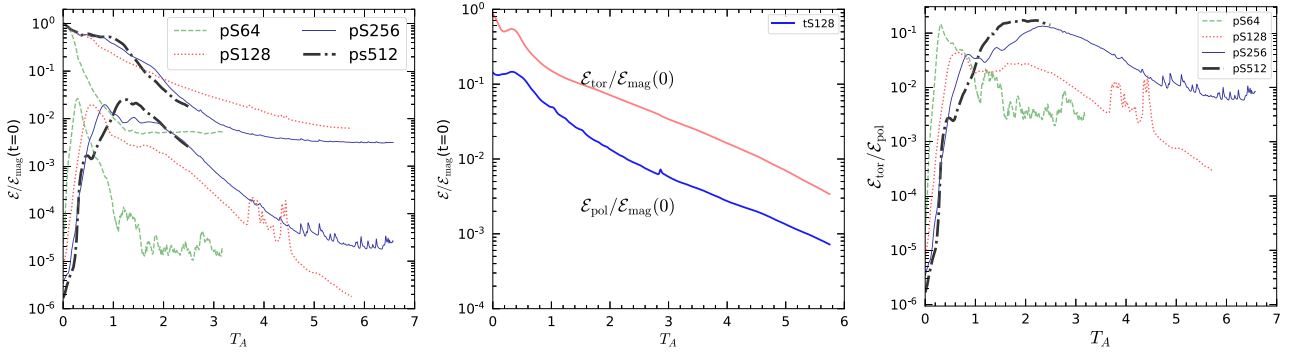
Figure 4. Evolution of poloidal and toroidal energies normalized to the initial magnetic energy (in log scale) for the poloidally dominated initial condition (left-hand panel), toroidally dominated initial condition (middle panel), and ratio of toroidal to poloidal energies (right-hand panel) for the runs `pS512`, `pS256`, `pS128`, and `pS64`.
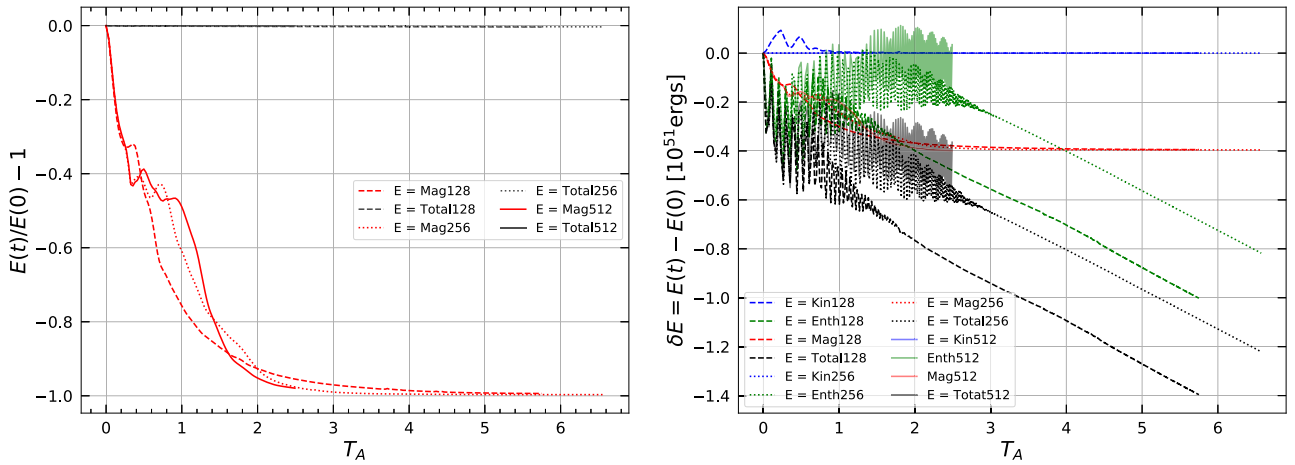

Figure 5. Left-hand panel: difference in $E(t)$ and $E(t = 0)$ normalized by $E(t = 0)$ for the total energy (black) and magnetic energy (red). Right-hand panel: difference in kinetic energy (blue), magnetic energy (red), total energy (black), and enthalpy (green) to its initial value for the different setups `pS128`, `pS256`, and `pS512` with respect to T_A.

$\sim 2T_A$, while the setup `pS256` reaches 10 per cent at $\sim 2.5T_A$. Again, we lack convergence in our simulations; however, at later stages at $6.5T_A$, the toroidal field for `pS256` settles at 1 per cent of the poloidal energy.

To study the energetics, we decompose the total energy of the star into four different components following Noble et al. (2006): kinetic, magnetic, rest mass, and the enthalpy (see Appendix A of this paper for the mathematical expressions). In the left-hand panel of Fig. 5, we show the change in magnetic and total energies to its initial value (δE) normalized by the initial value. We see that the total energy remains conserved; however, the magnetic energy decays. To understand the loss of magnetic energy, we plot δE for the individual energy components (except the rest mass as it remains conserved in our simulations) inside the star for the setups `pS128`, `pS256`, and `pS512`, and look at their behaviour with T_A. First, the change in kinetic energy from its initial value is negligibly small, which means that the fluid almost remains static and experiences only small variations in movement due to the presence of the instability that we notice at $\sim 0.5T_A$. Secondly, the magnetic energy decreases, and this loss is independent of the resolution of our simulations. More than 90 per cent of the initial magnetic energy is lost, which either gets radiated away to infinity or gets dissipated as heat inside the star. We calculated the Poynting flux over the surface of the star and found that $\sim 6.84 \times 10^{44}$ erg of the total magnetic energy gets converted

to radiation outside. However, a major portion goes into heating the interior of the star as we can see from the rise in enthalpy till $\sim 2T_A$. The enthalpy loss is dependent on the grid resolution and reduces by a factor of 2 when the resolution is increased by the same factor. Higher resolutions than those considered here would be needed to minimize numerical dissipation effects. These results strongly depend on the outflow boundary conditions used in our simulations; however, a realistic NS has a crystalline-solid crust, which would prevent any dissipation of magnetic energy outside the star and can significantly influence our simulation results.

3.2 Growth

Following Zink et al. (2007) and Lasky et al. (2012), we study the magnetic field dynamics in terms of the Fourier modes

$$C_m = \int_0^{2\pi} B_\phi(\bar{\omega}, \phi, z = 0) e^{im\phi} \, d\phi, \qquad (15)$$

where $\bar{\omega} = \sqrt{x^2 + y^2} = 0.8R$ is a contour in the equatorial plane of the star. We compute C_m for $m \in [1, 2, 3, 4]$ and show them in Fig. 6.

The inset gives a closer look at the initial stage of the evolution. As a first observation, we can see that all the different modes are excited and each one grows exponentially. Secondly, this growth saturates
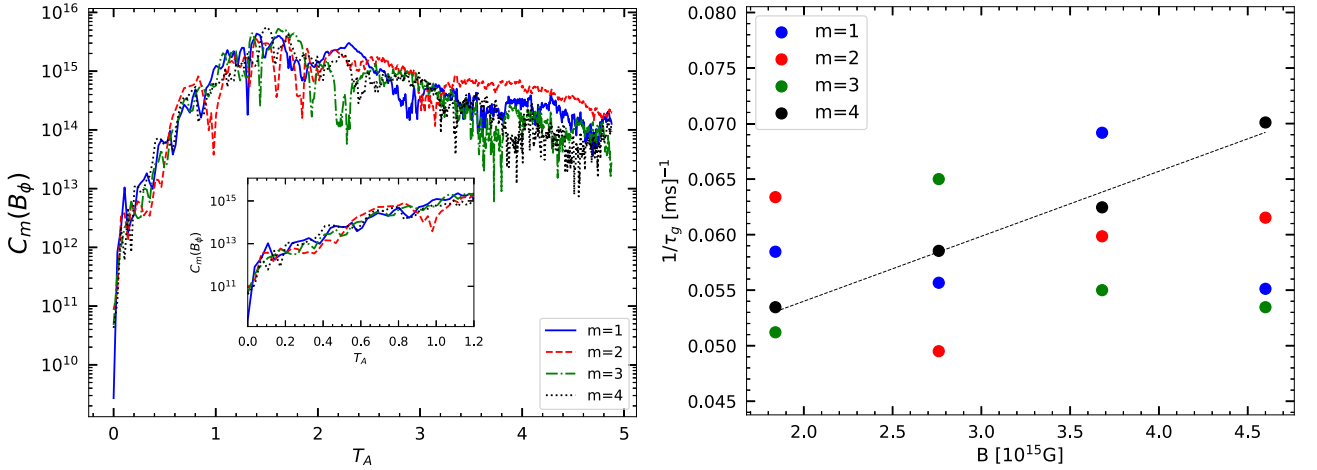
Figure 6. Left-hand panel: Fourier decomposition of B_ϕ for the setup pS256 and complex weighted averages for the different modes $m \in (1, 2, 3, 4)$ shown till $5T_A$. The inset shows the first $1.2T_A$ of the evolution, where we can see that the $m = 2$ grows the fastest till 1 Alfvén crossing time. Right-hand panel: linear relationship between the Alfvén times calculated for the different magnetic field strengths in pS128.

after a few Alfvén periods from which the different modes evolve less dramatically. Thirdly, the loss of magnetic energy causes these modes to lose strength. And lastly, all the different modes grow closely (as seen from the inset of Fig. 6, left-hand panel); however, the $m = 2$ mode remains strongest followed by $m = 1$, 4, and 3, respectively. We calculate the growth times (τ_g) for the various modes defined by the following:

$$\tau_g = \frac{\Delta t}{\Delta \ln(C_m)}. \tag{16}$$

The strength of the volume-averaged magnetic field is varied in our simulations using the setup pS128 since it is computationally less expensive to run each simulation than pS256. By using the modes (1, 2, 3, 4), we calculated the growth times for each case. We plot the inverse of τ_g as a function of B in Fig. 6 (right-hand panel). There are some errors introduced when computing τ_g during the exponential phase as it is difficult to select an interval of time where this growth happens, and one should take different realizations and report the mean and standard deviation of these data. Since we are only qualitatively interested in the behaviour of τ_g, we take the time interval between the minimum and maximum values of C_m. It is difficult to establish a linear relationship between τ_g and the inverse field strength predicted by perturbation theory, but we found one only for the mode $m = 4$ and presented the best-fitting dashed line in Fig. 6 (right-hand panel). The values of τ_g for the field strengths $\{4.5, 3.6, 2.7, 1.8\} \times 10^{15}$ G are, respectively, the following: $\{18.1, 14.4, 17.9, 17.1\}$ ms for the mode $m = 1$; $\{16.2, 16.7, 20.2, 15.7\}$ ms for the mode $m = 2$; $\{18.7, 18.1, 15.4, 19.5\}$ ms for the mode $m = 3$; and $\{14.2, 16.0, 17.0, 18.7\}$ ms for the mode $m = 4$. The growth time for the strongest magnetic field setup should be shortest for all modes considered, but this is observed only for $m = 3$ and 4. A majority of these modes have abrupt erratic growth times, with the shortest mode being $m = 3$ for the field strength of 3.6×10^{15} G, while the longest mode was $m = 2$ for the field strength of 2.7×10^{15} G.

3.3 Turbulence

The magnetic field in young NSs experiences turbulence after their birth during a period when the neutrinos have not fully escaped and provide heat as energy[1] (Mabanta & Murphy 2018). In old NSs, curvature contributions to mutual friction also cause differences in angular velocity between the superfluid and the rest of the star, which can also cause superfluid turbulence in the core of the NS (Peralta et al. 2006; Andersson, Sidery & Comer 2007). It is expected that the magnetic field should break in smaller eddies and dissipate most of its energy as the star ages, but observations show that a certain fraction of the NS population has stronger fields. Longer time-scale (∼1 Myr) simulations have shown that the magnetic field in the crust attends a state known as 'Hall attractor' after driven by the Hall effect (Gourgouliatos & Cumming 2014a). Even though this equilibrium stage is achieved only at much later times, the magnetic field evolves more rapidly in the initial phase in the lives of NSs. As a result of the initial instability and reconnection, turbulence can be driven by the magnetic field in NSs.

On simulating magnetic field evolution in NSs, it was observed that the system exhibited turbulence when the Kolmogorov spectra were calculated for both the kinetic and magnetic energies (Sur et al. 2020). This was speculated to be caused by the initial perturbation of the fluid velocity, which was used to trigger the instability quickly. However, the signals obtained were noisy, owing to the limited resolution of the simulations, and this caused the spectra to be indistinguishable for the power-law scaling of $-5/3$ (predicted by the classical Kolmogorov theory; Kolmogorov 1941) from other MHD turbulence spectra (Boldyrev et al. 2011; Beresnyak 2019; Schekochihin 2020). The fact that the poloidal and toroidal energies in the simulations presented in Sur et al. (2020) did not settle to an equilibrium, but rather oscillated around a mean value, could possibly be the result of turbulence triggered by the instability of the initial purely poloidal field. To understand whether this turbulence is physical and not caused by numerical effects, it is required to analyse simulation data generated from higher resolution and longer MHD runs.

In this work, we are in a better position to study the effect of turbulence given that our simulations have higher resolution compared to ones presented in Sur et al. (2020). We compute the power spectrum of the specific kinetic energy. The Fourier transform of the 3D velocity vector is given by

$$u^j(\mathbf{k}) = \int u^j(\mathbf{x}) e^{-i\pi \mathbf{k} \cdot \mathbf{x}} d^3 \mathbf{x} \tag{17}$$

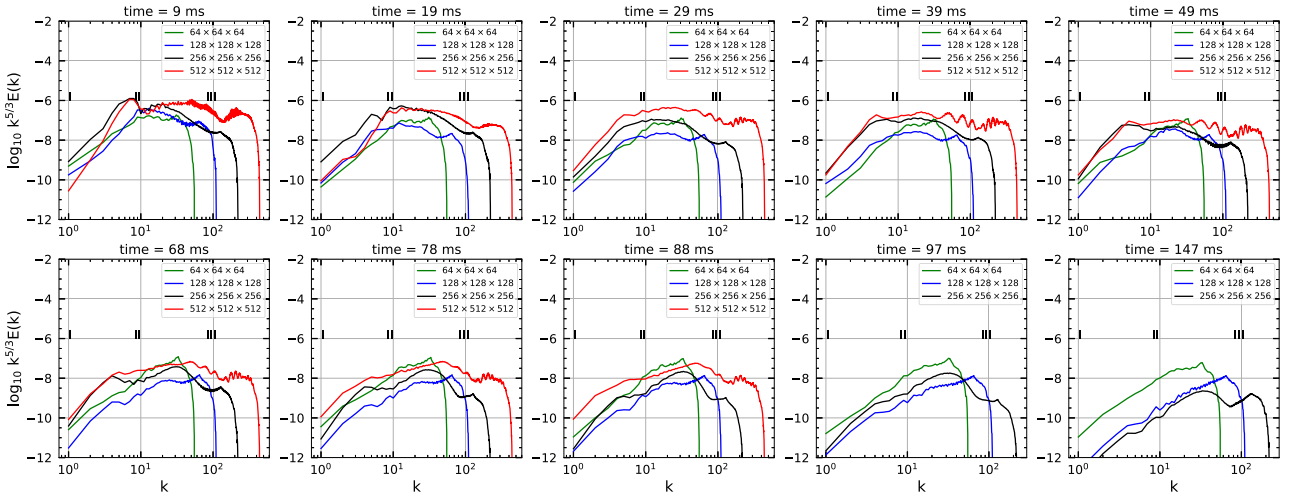[1]In private communication with Andreas Reisenegger.

Figure 7. Spectra of specific kinetic energy $E(k)$ (equation 19) inside the star and multiplied by Kolmogorov scaling $k^{5/3}$ calculated for our different resolution setups (given as figure labels). The different plots represent different times in the evolution of our system (given by the title in each figure).

and the specific kinetic energy is calculated as

$$\varepsilon_k(\boldsymbol{k}) = \frac{1}{2} u^j(\boldsymbol{k}) \cdot u^{j\,\dagger}(\boldsymbol{k}), \qquad (18)$$

where $u^{j\,\dagger}$ is the complex conjugate of u^j. It is then straightforward to calculate the velocity power spectral density as

$$E(k) = \frac{1}{2} \Sigma_{\boldsymbol{k} < |\boldsymbol{k}'| < k + \mathrm{d}k} \varepsilon_k(\boldsymbol{k}'). \qquad (19)$$

We use the numerical algorithm outlined in Navah, de la Llave Plata & Couaillier (2018). We select our computational domain such that it filters out regions only within the stellar surface with a radius of $0.95R$. For this, we use the density value $\rho \geq 10^{14}\ \mathrm{g\,cm^{-3}}$ to select the sphere and discard regions with $\rho < 10^{14}\ \mathrm{g\,cm^{-3}}$. As the strong magnetic field deforms the star, this selection criterion correctly accounts the effect of non-sphericity. Due to the sharp gradients in velocities present close to the surface, we apply an exponential decay window function and make the velocities go to zero when r approaches R. The window function is only applied in post-processing, i.e. while computing the turbulent spectra, and not during the evolution of the magnetic field in our simulations. This windowing is required to make the data segment periodic and prevent any jump discontinuities that may arise while computing the Fourier transform of our velocities. Without the window function, there arise superficial features in the spectra that are unphysical. Fig. 7 shows the specific kinetic energy spectra versus wavenumber ($k = |\boldsymbol{k}|$) for the different resolution setups with varying times. The red, black, green, and blue lines correspond to the setups pS512, pS256, pS128, and pS64, respectively. Since the setup pS512 has an evolution time of 88 ms, we show its spectra until this point. For convenience, we plot the quantity $k^{5/3}E(k)$ to get a flat spectrum when it follows the Kolmogorov scaling. There are three distinct regions characteristic of such a spectrum: the energy-containing range (region I), the inertial subrange (region II), and the dissipative range (region III), as shown in the figures. At $t = 29$ and 39 ms, we see that the spectra in region II become flat, but the Kolmogorov scaling becomes weaker as seen from $t = 68$ ms. The evolution shows us that at largest scales, kinetic energy is gradually lost, while this is not so prominent for our lower resolution setup. The spectra at different times indicate that there is a lack of convergence, as we should expect that at large scales, the spectra should have similar energies regardless of the resolution.

To understand whether this feature is physical, we performed a pure hydrodynamics (HD) simulation for pS128 without evolving the magnetic field. We calculated the spectra for the pure hydro run and compared with the MHD simulation in Fig. 8. The spectra differed at large scales where MHD is seen to drive large-scale flows, while the dynamics for the hydro run at small scales comparatively remains the same at different times caused by atmospheric noise. This was also visible when we plotted the velocity field of our star and observed large spikes at the $y = 0$ axis on the equatorial plane. Thus, most likely at small scales, we are not observing turbulence, but rather a noisy velocity field in our simulations.

4 CONCLUSIONS AND DISCUSSIONS

In this paper, we presented long-term GRMHD evolution in NSs by performing simulations using the code ATHENA++. We studied the energy variations of the poloidal and toroidal magnetic fields, the kinetic energy, and the enthalpy with time for four different resolutions 64^3, 128^3, 256^3, and 512^3 in a Cartesian grid.

We explored two different initial conditions, one purely poloidal and one with dominant toroidal field. We find that in all the different resolution setups, a purely poloidal field is unstable and this gives rise to a toroidal component. The toroidal energy becomes comparable in strength to the poloidal energy during the initial stages of the evolution, but at later times, it decreases significantly and becomes approximately 1 per cent of the total magnetic energy at $t \sim 880$ ms corresponding to 6.5 Alfvén periods. Our setup $pS512$ has an evolution time of $2.5T_A$ at which the toroidal field reaches 20 per cent of the poloidal energy and 10 per cent of the total magnetic energy once the simulation ends. However, our longer simulations such as ps256 do not reach any equilibrium magnetic field configuration and lack convergence at later stages in the evolution. For the toroidally dominated setup, we found the ratios of poloidal and toroidal energies to the total magnetic energy to settle at an equilibrium value of 0.2 and 0.8, respectively.

On comparing the different initial conditions, we address two main issues. The first concerns the different behaviour of the toroidal versus poloidal dominated simulations. The stronger toroidal setup develops a sizeable poloidal component with 20 per cent of the total magnetic energy but does not become the dominant component at the
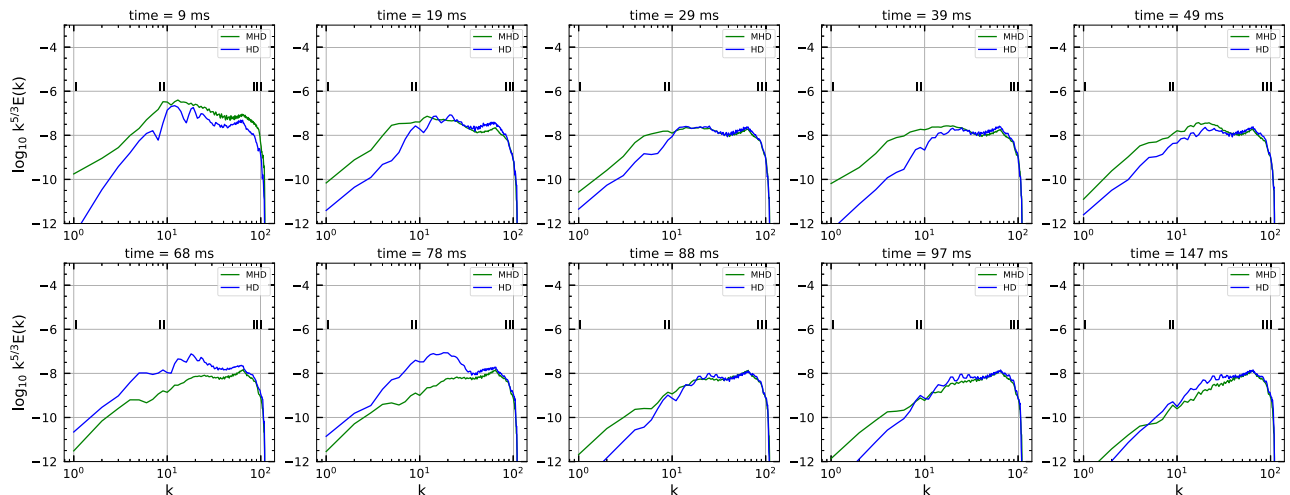
Figure 8. A comparison of the specific kinetic energy spectra for `pS128` between the HD simulation and the MHD simulation.

end of the simulation. On the other hand, the purely poloidal setup does not develop such a large toroidal component, which is likely due to the different boundary conditions implemented in this work when compared to Sur et al. (2020). The second issue concerns the final values of the different energy components. Our simulations are significantly longer than those in Sur et al. (2020).

In Fig. 4, it appears that the ratio between toroidal and poloidal energies, in the case of our higher resolution simulations, is gradually decreasing. Moreover, the higher resolution simulations seem to be losing more magnetic energy compared to the lower ones. This loss in magnetic energy from the star increases the internal energy, while around 10^{44} erg of the magnetic energy is radiated to infinity in the form of electromagnetic radiation. Our models, however, do not have a solid crust or resistivity, two important factors that influence electromagnetic emission in realistic NSs. Some of the most luminous magnetar giant flares can be explained with the release of energy from crustal breaking (Lander et al. 2015).

An important aspect we addressed in our simulations was to study the turbulence in NS MHD simulations. It was seen in Sur et al. (2020) that the magnetic field instability caused the system to experience turbulence, and this may have caused the poloidal and toroidal energies to reach only a quasi-equilibrium. However, due to limited resolution, the spectra were noisy and difficult to establish a power-law scaling according to the Kolmogorov theory. In this work, we analysed data from higher resolution MHD runs and found that this turbulence is not physical but rather caused by noise in the velocity field inside the star. This was confirmed on comparing the spectra between HD and MHD runs. The main difference occurred at large scales where the MHD simulations demonstrated large-scale flows, while the small-scale dynamics remained the same between HD and MHD cases.

Overall, we find consistent results with the previous GR works at early times (e.g. Ciolfi et al. 2011; Ciolfi & Rezzolla 2012 and references therein) while extending the simulations to 880 ms, which is much longer than previously obtained (e.g. 400 ms in Lasky et al. 2011). Our finest grid resolution is 0.1155 km, which is similar to Ciolfi & Rezzolla (2012) but also higher than Lasky et al. (2011) where a grid of ∼0.23 km was used. However, higher resolution and longer simulations are still required to settle the issue of what happens to the late-time evolution of different energy components and the turbulence in studies of magnetic field simulations of NSs.

DATA AVAILABILITY

The data underlying this paper would be available on request to the corresponding author.

REFERENCES

Andersson N., Sidery T., Comer G. L., 2007, MNRAS, 381, 747
Armaza C., Reisenegger A., Valdivia J. A., 2015, ApJ, 802, 121
Beresnyak A., 2019, Living Rev. Comput. Astrophys., 5, 2
Bilous A. V. et al., 2019, ApJ, 887, L23
Boldyrev S., Perez J. C., Borovsky J. E., Podesta J. J., 2011, ApJ, 741, L19
Bonazzola S., Gourgoulhon E., 1996, A&A, 312, 675
Braithwaite J., 2007, A&A, 469, 275
Braithwaite J., Nordlund A., 2006, A&A, 450, 1077
Braithwaite J., Spruit H. C., 2006, A&A, 450, 1097

Burrows A., Dessart L., Livne E., Ott C. D., Murphy J., 2007, ApJ, 664, 416

Chung C. T. Y., Melatos A., 2011a, MNRAS, 411, 2471

Chung C. T. Y., Melatos A., 2011b, MNRAS, 415, 1703

Ciolfi R., 2020, Gen. Relativ. Gravit., 52, 59

Ciolfi R., Kalinani J. V., 2020, ApJ, 900, L35

Ciolfi R., Rezzolla L., 2012, ApJ, 760, 1

Ciolfi R., Rezzolla L., 2013, MNRAS, 435, L43

Ciolfi R., Ferrari V., Gualtieri L., Pons J. A., 2009, MNRAS, 397, 913

Ciolfi R., Ferrari V., Gualtieri L., 2010, MNRAS, 406, 2540

Ciolfi R., Lander S. K., Manca G. M., Rezzolla L., 2011, ApJ, 736, L6

Cumming A., Arras P., Zweibel E., 2004, ApJ, 609, 999

Cutler C., 2002, Phys. Rev. D, 66, 084025

de Lima R. C. R., Coelho J. G., Pereira J. P., Rodrigues C. V., Rueda J. A., 2020, ApJ, 889, 165

Felker K. G., Stone J. M., 2018, J. Comput. Phys., 375, 1365

Flowers E., Ruderman M. A., 1977, ApJ, 215, 302

Frederick S. G., Kuchera M. P., Thompson K. L., 2021, MNRAS, 503, 2764

Frieben J., Rezzolla L., 2012, MNRAS, 427, 3406

Geppert U., Viganò D., 2014, MNRAS, 444, 3198

Gourgouliatos K. N., Cumming A., 2014a, Phys. Rev. Lett., 112, 171101

Gourgouliatos K. N., Cumming A., 2014b, MNRAS, 438, 1618

Gourgouliatos K. N., Cumming A., 2015, MNRAS, 446, 1121

Gourgouliatos K. N., Cumming A., Reisenegger A., Armaza C., Lyutikov M., Valdivia J. A., 2013, MNRAS, 434, 2480

Gourgouliatos K. N., Wood T. S., Hollerbach R., 2016, Proc. Natl. Acad. Sci., 113, 3944

Gusakov M. E., Kantor E. M., Ofengeim D. D., 2017, Phys. Rev. D, 96, 103012

Haskell B., Samuelsson L., Glampedakis K., Andersson N., 2008, MNRAS, 385, 531

Herbrik M., Kokkotas K. D., 2017, MNRAS, 466, 1330

Hollerbach R., Rüdiger G., 2002, MNRAS, 337, 216

Kiuchi K., Yoshida S., 2008, Phys. Rev. D, 78, 044045

Kolmogorov A., 1941, Dokl. Akad. Nauk SSSR, 30, 301

Kraav K. Y., Gusakov M. E., Kantor E. M., 2021, MNRAS, 506, L74

Lander S., Jones D., 2009, MNRAS, 395, 2162

Lander S., Jones D., 2011, MNRAS, 412, 1730

Lander S., Jones D., Passamonti A., 2010, MNRAS, 405, 318

Lander S. K., Andersson N., Antonopoulou D., Watts A. L., 2015, MNRAS, 449, 2047

Lasky P. D., Zink B., Kokkotas K. D., Glampedakis K., 2011, ApJ, 735, L20

Lasky P. D., Zink B., Kokkotas K. D., 2012, preprint (arXiv:1203.3590)

Liu Y. T., Shapiro S. L., Etienne Z. B., Taniguchi K., 2008, Phys. Rev. D, 024012, 78

Mabanta Q. A., Murphy J. W., 2018, ApJ, 856, 22

Markey P., Tayler R. J., 1973, MNRAS, 163, 77

Markey P., Tayler R. J., 1974, MNRAS, 168, 505

Moiseenko S. G., Bisnovatyi-Kogan G. S., Ardeljan N. V., 2006, MNRAS, 370, 501

Mösta P. et al., 2014, ApJ, 785, L29

Navah F., de la Llave Plata M., Couaillier V., 2018, preprint (arXiv:1809.03966)

Noble S. C., Gammie C. F., McKinney J. C., Del Zanna L., 2006, ApJ, 641, 626

Ofengeim D. D., Gusakov M. E., 2018, Phys. Rev. D, 98, 043007

Ostriker J. P., Gunn J. E., 1969, ApJ, 157, 1395

Peralta C., Melatos A., Giacobello M., Ooi A., 2006, ApJ, 651, 1079

Pili A. G., Bucciantini N., Del Zanna L., 2014, MNRAS, 439, 3541

Pili A. G., Bucciantini N., Del Zanna L., 2017, MNRAS, 470, 2469

Pons J. A., Perna R., 2011, ApJ, 741, 123

Schekochihin A. A., 2020, preprint (arXiv:2010.00699)

Shibata M., Liu Y. T., Shapiro S. L., Stephens B. C., 2006, Phys. Rev. D, 74, 104026

Stone J. M., Tomida K., White C. J., Felker K. G., 2020, ApJS, 249, 4

Sur A., Haskell B., 2021, PASA, 38, e043

Sur A., Haskell B., Kuhn E., 2020, MNRAS, 495, 1360

Tayler R. J., 1957, Proc. Phys. Soc. B, 70, 31

Tayler R. J., 1973, MNRAS, 161, 365

Thompson C., Duncan R. C., 1995, MNRAS, 275, 255

White C. J., Stone J. M., Gammie C. F., 2016, ApJS, 225, 22

Wright G. A. E., 1973, MNRAS, 162, 339

Zink B., Stergioulas N., Hawke I., Ott C. D., Schnetter E., Müller E., 2007, Phys. Rev. D, 76, 024019

APPENDIX A:

Let us first note the following definitions, where the normal observer's four-velocity (n_μ) in the coordinate basis t, x_1, x_2, x_3 is given by

$$n_\mu = (-\alpha, 0, 0, 0), \tag{A1}$$

$$\alpha^2 = -1/g^{tt} = -g_{tt}, \tag{A2}$$

$$\gamma = -n_\mu u^\mu, \tag{A3}$$

where γ is the Lorentz boost and α is known as the lapse function. The projection tensors, which project into a space normal to the fluid four-velocity, are given by

$$h_{\mu\nu} = g_{\mu\nu} + u_\mu u_\nu, \tag{A4}$$

$$j_{\mu\nu} = g_{\mu\nu} + n_\mu n_\nu. \tag{A5}$$

We work in isotropic coordinates such that $g_{xx} = g_{yy} = g_{zz}$ and $g_{ij} = 0$ for $i \neq j$. The fluid is described by four-velocity u^μ, rest-mass density ρ_0, and pressure p. The magnetic field four-vector is given by

$$\mathcal{B}^\mu \equiv -n_\nu F^{\mu\nu} \tag{A6}$$

such that $b^\mu = h^\mu_\nu \mathcal{B}^\nu / \gamma$. The stress–energy tensor can be decomposed into a fluid part (subscript F) and a magnetic part (subscript B) as the following:

$$T^{\mu\nu} = T_F^{\mu\nu} + T_B^{\mu\nu}, \tag{A7}$$

where

$$T_F^{\mu\nu} = w u^\mu u^\nu + p g^{\mu\nu}, \tag{A8}$$

$$T_B^{\mu\nu} = b^2 u^\mu u^\nu + b^2 g^{\mu\nu} - b^\mu b^\nu, \tag{A9}$$

where $w = p + \rho_0 + \rho_0 \epsilon$ and $\epsilon = p/(\Gamma - 1)\rho_0$ is the specific internal energy density. We define the fluid and magnetic currents as

$$J_F^\nu = -T_F^{\mu\nu} \partial_\mu^t \tag{A10}$$

$$J_B^\nu = -T_B^{\mu\nu} \partial_\mu^t \tag{A11}$$

such that the total energy current is $J_E^\nu = J_F^\nu + J_B^\nu$ and the total energy is

$$E = \int (-J_E^\nu n_\nu) \sqrt{-g} \, \mathrm{d}^3 \boldsymbol{x}. \tag{A12}$$

Using the relation $g_{\mu\nu} u^\mu u^\nu = -1$, we get $u^t = \alpha \sqrt{1 + g_{xx}(u^1)^2 + g_{yy}(u^2)^2 + g_{zz}(u^3)^2}$. The different energies can be computed as the following:

$$E = \int T_\mu{}^\nu \partial_t^\mu n_\nu \mathrm{d}^3 \boldsymbol{x} \sqrt{-g}, \tag{A13}$$

$$M_{\rm rest} = - \int \rho_0 u^\mu n_\mu {\rm d}^3 \boldsymbol{x} \sqrt{-g},$$
(A14)

$$E_B = \int \left(b^2 u_\mu u^\nu + \frac{b^2}{2} g_\mu{}^\nu - b_\mu b^\nu\right) \partial_t^\mu n_\nu {\rm d}^3 \boldsymbol{x} \sqrt{-g},$$
(A15)

$$E_k = \int (w u_\mu u^\nu + p g_\mu{}^\nu) \partial_t^\mu n_\nu {\rm d}^3 \boldsymbol{x} \sqrt{-g} - M_{\rm rest} - E_H,$$
(A16)

$$E_H = \int (\rho_0 \epsilon_H + p) \gamma {\rm d}^3 \boldsymbol{x} \sqrt{-g},$$
(A17)

where $\sqrt{-g} = g_{xx}^{3/2}$, E is the total energy, E_B, E_k, and E_H are the magnetic, kinetic, and enthalpy, respectively.

This paper has been typeset from a TeX/LaTeX file prepared by the author.

Author contributions statement

Title: "Long-term general relativistic magnetohydrodynamics simulations of magnetic field in isolated neutron stars"

Authors: Ankan Sur, William Cook, David Radice, Brynmor Haskell, Sebastiano Bernuzzi

Publication: Monthly Notices of the Royal Astronomical Society, Volume 511, Issue 3, pp.3983-3993

Contribution by:

Ankan Sur: Performed calculations, produced analysis scripts, figures, entirely written the manuscript, and managed submission. My contribution to this article is 45%.
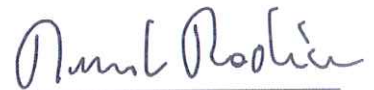
_____
Ankan Sur

William Cook: I have performed all the simulations, produced figures, and contributed to writing the paper. My contribution to this article is 45%.

_____
William Cook

David Radice: interpretation of results, supervision, and proofread the manuscript. My contribution to this article is 4%.

_____
David Radice

Brynmor Haskell: interpretation of results, supervision, and proofread the manuscript. My contribution to this article is 3%.

_____
Brynmor Haksell

Sebastiano Bernuzzi: interpretation of results, supervision, and proofread the manuscript. My contribution to this article is 3%.

_____
Sebastiano Bernuzzi

The impact of superconductivity and Hall effect in models of magnetised neutron stars

"Nature has a great simplicity and therefore a great beauty"
-Richard Feynman

CAMBRIDGE
UNIVERSITY PRESS

Research Paper

The impact of superconductivity and the Hall effect in models of magnetised neutron stars

Ankan Sur* ⬤ and Brynmor Haskell

Nicolaus Copernicus Astronomical Center, Polish Academy of Sciences, Bartycka 18, 00-716 Warsaw, Poland

Abstract

Equilibrium configurations of the internal magnetic field of a pulsar play a key role in modelling astrophysical phenomena from glitches to gravitational wave emission. In this paper, we present a numerical scheme for solving the Grad–Shafranov equation and calculating equilibrium configurations of pulsars, accounting for superconductivity in the core of the neutron star, and for the Hall effect in the crust of the star. Our numerical code uses a finite difference method in which the source term appearing in the Grad–Shafranov equation, which is used to model the magnetic equilibrium is non-linear. We obtain solutions by linearising the source and applying an under-relaxation scheme at each step of computation to improve the solver's convergence. We have developed our code in both C++ and Python, and our numerical algorithm can further be adapted to solve any non-linear PDEs appearing in other areas of computational astrophysics. We produce mixed toroidal–poloidal field configurations, and extend the portion of parameter space that can be investigated with respect to previous studies. We find that in even in the more extreme cases, the magnetic energy in the toroidal component does not exceed approximately 5% of the total. We also find that if the core of the star is superconducting, the toroidal component is entirely confined to the crust of the star, which has important implications for pulsar glitch models which rely on the presence of a strong toroidal field region in the core of the star, where superfluid vortices pin to superconducting fluxtubes.

Keywords: magnetic fields – neutron stars – numerical – pulsars

(Received 30 April 2021; revised 6 July 2021; accepted 29 July 2021)

1. Introduction

The magnetic field in neutron stars (NSs) varies over a very wide range, with strengths ranging from 10^8 G in old recycled pulsars all the way upto 10^{15} G in magnetars. These values of the magnetic field are generally inferred from the observed spindown rate of the star, assuming that it is due to magnetic dipole radiation. This provides information on the exterior field far from the star, however, details about the interior field configuration remain unknown. Observationally, the inferred exterior magnetic field of pulsars is found to be relatively stable on short timescales, except for energetic outbursts and flares in magnetars (Rea & Esposito 2011; Coti Zelati et al. 2018). Nevertheless, the differences in field strengths between different populations, suggest that on long timescales, comparable to the lifetime of the star, the field may evolve, and that different classes of neutron stars may differ not only due to their age, but also to their magnetic field configuration at birth (Kaspi 2010). Any change in the exterior field is expected to be driven by internal phenomena, such as the flow of currents in the crust and superconductivity in the NS core. The dynamical interplay between these two regions is thus crucial to understand also magnetospheric phenomenology (Akgün et al. 2017; Glampedakis et al. 2014; Gourgouliatos et al. 2016; Gusakov et al. 2017a). Understanding the secular evolution of the magnetic field is crucial to connect different evolutionary tracks

and NS classes like millisecond pulsars, rotation-powered pulsars, and magnetars. On dynamical timescales, however, it is of interest to understand the physical conditions that allow to obtain stable equilibria in NSs, in order to use such models as backgrounds to model phenomena such as gravitational wave emission due to oscillations or deformations of the crust (Ushomirsky et al. 2000; Payne & Melatos 2006; Osborne & Jones 2020; Singh et al. 2020).

A number of equilibrium models of magnetised stars have been produced in recent years, and to study their stability and evolution, magnetohydrodynamic (MHD) simulations have been performed, all of which have shown to produce quasi-equilibrium mixed poloidal–toroidal geometry starting from the earlier works of Braithwaite & Spruit (2006); Braithwaite & Nordlund (2006); Ciolfi et al. (2011) and more recently by Sur et al. (2020). Purely poloidal or purely toroidal magnetic field initial conditions are known to be unstable, and analytical and numerical studies have shown to favour an axisymmteric twisted-torus field (Haskell et al. 2008; Lander & Jones 2009; Lasky et al. 2011; Ciolfi & Rezzolla 2012) where the poloidal and the toroidal components stabilises one other. These models, however, consider a 'fluid' star, which makes them relevant only in the first instants of life of the star, when the temperature is too high for the crust to have formed yet. Furthermore in most cases, the equation of state is taken to be barotropic, and the stability of barotropic equilibria has been questioned (Lander & Jones 2012; Mitchell et al. 2015). Rotation may provide partial stabilisation and in particular the boundary conditions play an important role in determining whether the poloidal or the toroidal field is globally dominant (Lander & Jones 2012),

*Author for correspondence: Ankan Sur, E-mail: ankansur@camk.edu.pl

but stratification provided by charged particles of electrons and protons carrying magnetic flux moving through a neutron fluid in particular, may allow for additional degrees of freedom and allow to stabilise the field (Castillo et al. 2017; Castillo et al. 2020). In fact, barotropic axisymmetric equilibrium solutions are unstable under non-axisymmetric perturbations owing to MHD instabilities and stable stratification is likely to be required to prevent complete dissipation of the field (Braithwaite 2009; Reisenegger 2009; Mitchell et al. 2015). Nevertheless, while non-barotropicity may be crucial to understand the stability of the models, the equilibria themselves will not differ significantly from those of bartoropic stars in mature pulsars (Castillo et al. 2020), making barotropic equilibria an important tool to use in calculations that require magnetised background models of NSs.

It is well known that rotation (or more in general non-trivial fluid velocity fields in the stellar interior) may have an impact on the evolution of the magnetic field. First, instabilities due to perturbations developed within the NS are stabilised by rotation. Second, superfluids in deferentially-rotating NS cores experience torque oscillations (Peralta et al. 2005; Melatos & Peralta 2007), which are likely to explain glitches observed in standard pulsars. Third, internal velocity fields and multifluid components could give rise to additional modes of oscillations and alter the properties of modes of non-rotating stars (Akgün & Wasserman 2008). Fourth, on studying magnetothermal evolution with macroscopic flux tube drift velocity, it had been shown that magnetic field may be weakly buried in the outermost layers of the core and not completely expelled, as previously thought, although this is sensitive to the initial conditions (Elfritz et al. 2016). And lastly, the presence of bulk motion in the crust was explored in Kojima et al. (2021) who showed that the magnetic energy is converted into mechanical work and parts of it are dissipated through bursts or flares. A realistic model of NS should consider a solid crust and a fluid core, which are in rotation (and possibly in differential rotation due to hydromagnetic torques). However, in this work, we neglect the effects of rotation as we are mainly interested in the magnetic field configuration in mature pulsars, which are slowly rotating, and in understanding the impact of suprconductivity in the core and of the Hall effect in the crust. It is, nevertheless, important to keep in mind that rotation may play an important role in the evolution of younger, strongly magnetised, NSs, and should be considered to obtain a full picture of the evolution of the field during the lifetime of a NS.

The crust of a NS consists of $\approx 1\%$ of the total mass, but plays an important role for the dynamics and emission properties of the star. The composition of these outer layers depends on the equation of state and the density varies from 10^6 gm cm^{-3} in the outer crust to $\sim 10^{14}$ gm cm^{-3} at which point there is a transition to a fluid outer core of neutrons, protons, electrons and muons, and at higher densities still, in the inner core, one may have an inner core of exotic particles like hyperons, superconducting quark matter and Boson condensates. When the temperature drops below $T \approx 10^9$ K, soon after birth, the crusts begins to solidify, and forms conducting crystal lattice with free electrons soaked in superfluid neutrons where the Lorentz force can be balanced by elastic forces. During the lifetime of a NS, the evolution of the field in the crust is mainly affected by two processes: (a) the Hall effect and (b) Ohmic dissipation, owing to the currents carried by electrons in the crust (Goldreich & Reisenegger 1992; Cumming et al. 2004; Pons & Geppert 2007; Hollerbach & Rüdiger 2002). It is known that Hall effect leads to turbulent cascades but whether it leads to

complete dissipation of the field or relaxes to a stable state is an important question as stationary closed configuration is neutrally stable Lyutikov (2013). Over the Hall timescale, (Gourgouliatos & Cumming 2014) have shown that indeed the field evolves to a state known as the 'Hall attractor' having a dipolar poloidal field and a weak quadrupolar toroidal component. Depending on the steepness of the electron density, this field may dissipate rapidly (Gourgouliatos et al. 2013). As the field relaxes from an MHD (fluid) to a Hall equilibrium, it may drive the expulsion of toroidal loops powering flares from the NS crust (Thompson & Duncan 1995).

When the temperature drops below $\approx 10^9$ K in the core, the protons will be superconducting and the neutrons superfluid (Haskell & Sedrakian 2018), which will have a significant effect on the evolution of the field in the standard pulsar population (Ofengeim & Gusakov 2018; Gusakov et al. 2017b; Gusakov et al. 2020). Superconductivity, in particular, affect the magnetic field, as if it is of type II, as theoretical models suggest, the field will be confined to flux tubes, which can also interact with superfluid neutron vortices (see Haskell & Sedrakian 2018 for a review). In fact, the possibility that neutron vortices may pin in strong toroidal field regions in the superconducting core has been proposed as an explanation for the observed high values for the activity parameter in glitching pulsars such as the Vela (Gügercinoğlu & Alpar 2014; Gügercinoğlu 2017; Gügercinoğlu & Alpar 2020). In the core, Goldreich & Reisenegger (1992) was the first to propose that ambipolar diffusion becomes important where the charged particles like electrons and protons move relative to the neutrons. Glampedakis et al. (2011) showed that this ambipolar diffusion in superconducting/superfluid NSs has negligible effect on the magnetic field evolution. However, this can change if the core temperature is of the order $10^8 - 10^9$ K and the diffusion time scale is comparable to age of the star Passamonti et al. (2017).

A realistic model for the magnetic field structure of a standard pulsar cannot be that of a magnetised fluid star, and thus MHD equilibrium, but should include a superconducting core and a crust. In this paper, we therefore construct equilibrium models for magnetised NS, including type-II superconductivity in the core and the Hall effect in the crust, and compare our models to pure MHD and Hall equilibria.

The equilibrium of the magnetic field is studied by solving the so-called Grad–Shafranov (GS) equation (Shafranov 1966), whose formalism we discuss in the next section. This GS equation appears widely in plasma physics and analytical solutions are often hard to obtain. Nevertheless, when the source term has a simple form, we can use Green's functions to solve the GS equation. However, except for a small number of simple forms for the source function, numerical methods such as finite differences (Johnson et al. 1979), spectral methods (Ling & Jardin 1985), spectral elements (Howell & Sovinec 2014), and linear finite elements (Gruber et al. 1987) should be used. In applications to NSs, numerical solvers such as the HSCF method (Lander & Jones 2009), Gauss–Seidel method (Gourgouliatos et al. 2013) or the generalised Newton's method (Armaza et al. 2015) have been used.

We propose a numerical technique based on finite difference iterative scheme for solving the GS equation. We focus in the astrophysical relevance of the GS equation, in particular, to obtain magnetic equilibrium configurations in neutron stars. Our method is fast, written both in C++ and Python, and easier to implement numerically. We have generated models in regimes where numerical instabilities were faced by previous works. In

order to do this, we have demonstrated how non-linear source terms can be treated numerically for the first time. Our numerical algorithm in general can be applied to any such non-linear PDEs of the similar form, like the *Poisson* equation, appearing ubiquitously in physics.

This article is arranged as following: in Section 2, we derive the GS equation for Hall and MHD equilibrium, in Section 3, we describe the numerical algorithm to solve the discretised GS equation, in Section 4 we show our results for the normal matter star and the superconducting core, while conclusions and discussions are finally presented in Section 5.

2. Mathematical formalism

In general, the magnetic field ($\vec{B}$) in spherical coordinates is expressed in terms of two scalar functions, $\alpha(r, \theta)$ representing the poloidal component, and $\beta(r, \theta)$ representing the toroidal component, as

$$\vec{B} = \vec{\nabla}\alpha \times \vec{\nabla}\phi + \beta\vec{\nabla}\phi, \tag{1}$$

where $\vec{\nabla}\phi = \hat{\phi}/r\sin\theta$. From Faraday's law, we have

$$\frac{\partial\vec{B}}{\partial t} = -c\vec{\nabla} \times \vec{E}, \tag{2}$$

where the electric field is $\vec{E} = -\frac{1}{c}\vec{v} \times \vec{B} + \frac{\vec{j}}{\sigma}$, $\vec{v}$ is the velocity of electrons which is related to the current density as $\vec{v} = -\frac{\vec{j}}{en}$, n is the electron density and σ is the electrical conductivity. Moreover, Ampere's law states that the current density is related to the magnetic field as $\vec{j} = \frac{c}{4\pi}\vec{\nabla} \times \vec{B}$, and substituting these in equation (2) yields the induction equation,

$$\frac{\partial\vec{B}}{\partial t} = -\frac{c}{4\pi e}\vec{\nabla} \times \left(\frac{\vec{\nabla} \times \vec{B}}{n} \times \vec{B}\right) - \frac{c^2}{4\pi}\vec{\nabla} \times \left(\frac{\vec{\nabla} \times \vec{B}}{\sigma}\right). \tag{3}$$

The first term on the right-hand side of the above equation is referred to as the Hall term while the second is the Ohmic dissipation term. The ratio of timescales on which these two terms operate is given by (Goldreich & Reisenegger 1992)

$$\frac{\tau_{\text{Ohm}}}{\tau_{\text{Hall}}} = 4 \times 10^4 \frac{B_{14}}{T_8^2}\left(\frac{\rho}{\rho_{\text{nuc}}}\right)^2, \tag{4}$$

where $B = B/10^{14}$ G and $T_8 = T/10^8$ K. Thus for a suitable choice of the parameters density, magnetic field, and temperature, the Hall effect is faster than the Ohmic term and we can obtain a family of Hall equilibrium solutions. In particular we expect this to be true in the cores of standard pulsars, with $B \approx 10^{12}$ G and internal temperatures of the order of $T \approx 10^7$ K.

The evolution of the magnetic field purely due to Hall effect is given by

$$\frac{\partial\vec{B}}{\partial t} = -\frac{c}{4\pi e}\vec{\nabla} \times \left(\frac{\vec{\nabla} \times \vec{B}}{n} \times \vec{B}\right). \tag{5}$$

To obtain steady-state models, axisymmetric Hall equilibria solutions are calculated by setting equation 5 to zero. Integrating this equation gives

$$\frac{1}{n}(\vec{\nabla} \times \vec{B}) \times \vec{B} = \vec{\nabla}\chi_{\text{Hall}}, \tag{6}$$

where χ_{Hall} is an arbitrary function of the coordinates r and θ, which can be physically interpreted as the magnetic potential since

its gradient gives the magnetic force. Substituting equation 1 gives the toroidal component as

$$\vec{\nabla}\alpha \times \vec{\nabla}\beta = 0, \tag{7}$$

which shows $\beta = \beta(\alpha)$. Moreover, $\vec{\nabla}\alpha \parallel \vec{\nabla}\chi_{\text{Hall}}$ implies $\chi_{\text{Hall}} = \chi_{\text{Hall}}(\alpha)$. This gives rise to the Grad–Shafranov (GS) equation for a two-dimensional plasma, which is a second-order non-linear partial differential equation (PDE) given by:

$$\Delta^\star\alpha = \frac{\partial^2\alpha}{\partial r^2} + \frac{(1-\mu^2)}{r^2}\frac{\partial^2\alpha}{\partial\mu^2} = -\chi'(\alpha)n(r)r^2(1-\mu^2) - \beta'\beta = -\mathcal{S}, \tag{8}$$

where $\Delta^\star$ is the GS operator, $\mu = \cos(\theta)$ and $\mathcal{S}$ is the source term.

The GS equation, however, does not only apply to Hall equilibria. In a barotropic NS, i.e., where the pressure is a function of mass density (ρ) alone, as $P = P(\rho)$, a very similar form of equation 6 is also obtained for MHD equilibria, for which one has:

$$\frac{1}{4\pi\rho}(\vec{\nabla} \times \vec{B}) \times \vec{B} = \frac{\nabla p}{\rho} + \nabla\phi, \tag{9}$$

with ϕ the gravitational potential. For a barotropic equation of state, equation (9) is clearly of the same form as the GS equation, and can thus be written in the same form as (6)

$$\frac{1}{\rho}(\vec{\nabla} \times \vec{B}) \times \vec{B} = \vec{\nabla}\chi_{\text{MHD}}, \tag{10}$$

where, however, the specific terms have different interpretations with respect to Hall equilibria (Gourgouliatos et al. 2013). Specifically in MHD, the mass density plays a similar role as the electron density while χ_{MHD} as χ_{Hall}. The poloidal field evolution takes the same form as equation 8, and thus it is necessary to obtain a numerical solution in either case of Hall or MHD equilibrium. In this study, we neglect any relativistic terms and assume that the conductivity is high enough that we can neglect the contributions of the Ohmic dissipation term, which is a good approximation in NS interiors. However, it should be noted that the Ohmic dissipation term is likely to be present in the crust and the Hall drift enhances it by forming small-scale eddies through which the field dissipates magnetic energy (Goldreich & Reisenegger 1992). Simulations have shown that the Hall drift term quickly saturates and the evolution of the field occurs on a slower Ohmic timescale (Pons & Geppert 2010; Kojima & Kisaka 2012; Viganò et al. 2012). Even if the field evolves rapidly during the initial stages, it approaches one among the family of steady-state Hall equilibrium solutions. Given that diffusivity only depends on radius, the Ohmic term will not affect the angular structure of the magnetic field. Gourgouliatos et al. (2013) showed that the electron fluid in the crust slows down rapidly compared to the Ohmic dissipation rate for a field connecting an external dipole. Further, the Hall term enhances the dissipation rate of higher order Ohmic modes as compared to pure Ohmic decay. To fully investigate the evolution of the field, one must solve the induction equation given in (3) as carried out by Marchant et al. (2014) who showed that starting from either purely poloidal equilibrium or an unstable equilibrium initial condition, the Ohmic dissipation evolved the field towards an attractor state through adjacent stable configurations superimposed by damped oscillations. Considering the effects of Ohmic term in our calculations is beyond the scope of this work, and we assume that as the Ohmic decay occurs on a much larger timescale as compared to the Hall timescale, our equilibria are an adequate approximation to the field configurations in a middle-aged pulsar.

3. Numerical method

In this section, we discuss our finite difference iterative scheme for solving the GS equation in spherical coordinates. We consider a two-dimensional grid on $r - \mu$ plane. There are N_r points in the r direction running from $r = r_{min}$ at $i = 0$ to $r = r_{max}$ at $i = N_r - 1$. The radial values have been normalised by the radius of the star (R) so that $r = 1$ corresponds to the stellar surface. Similarly, in the μ direction, we have N_μ points running from $\mu = -1$ at $j = 0$ and $\mu = +1$ at $j = N_\mu - 1$. The source term (S) is given by

$$S = \begin{cases} \chi'(\alpha)n(r)r^2(1 - \mu^2) + \beta'\beta & \text{if } r < 1 \\ 0 & \text{if } r \geq 1 \end{cases}, \quad (11)$$

where β is the toroidal component and the prime denotes derivative with respect to α. The functional form of β does not allow toroidal currents outside the star and thus makes the toroidal field to be located within the stellar interior. The electron density is assumed to be isotropic within the star, implying $n = n(r)$, and is zero outside due to vacuum. This makes the source term also zero outside the stellar surface. Moreover, this electron density appearing in Hall equilibria states are related to MHD equilibria by $n = \rho Y_e$, where Y_e is the electron number per unit mass which varies from $10^{22} - 10^{28}$ gm^{-1} across the crust.

We apply second-order finite difference scheme for equation 8 on a two-dimensional grid of $(r - \mu)$

$$\frac{\alpha_{i+1,j} + \alpha_{i-1,j} - 2\alpha_{ij}}{dr^2} + \frac{(1 - \mu_j^2)}{r_i^2}\frac{\alpha_{i,j+1} + \alpha_{i,j-1} - 2\alpha_{ij}}{d\mu^2} = -S_{ij} = Q_{ij}, \quad (12)$$

where $dr = (r_{max} - r_{min})/(N_r - 1)$, $d\mu = 2/(N_\mu - 1)$ and Q is the negative value of the source function S. On rearranging the above terms, we can get an expression for α_{ij} at the (k)th step in terms of all its neighbouring points,

$$\alpha_{ij}^k = \frac{(\alpha_{i+1,j}^k + \alpha_{i-1,j}^k)/dr^2}{\omega_{ij}} + \frac{(1 - \mu_j^2)}{r_i^2 d\mu^2}\frac{\alpha_{i,j+1}^k + \alpha_{i,j-1}^k}{\omega_{ij}} + \frac{S_{ij}}{\omega_{ij}}, \quad (13)$$

where $\omega_{ij} = 2/dr^2 + 2(1 - u_j^2)/r_i^2/d\mu^2$. We use updated values of α_{ij} whenever they are available. The boundary conditions were set to $\alpha(r, \mu = -1) = 0$, $\alpha(r, \mu = 1) = 0$, $\alpha(r = r_{min}, \mu) = 0$, and $\alpha(r = r_{max}, \mu) = 0$. Axisymmetry equilibrium requires the azimuthal component of the magnetic field to vanish, which allows us to consider a toroidal component of the form

$$\beta = s[\alpha - \alpha(r = 1, \mu = 0)]^p \Theta(\alpha - \alpha(r = 1, \mu = 0)), \quad (14)$$

where s and p are free parameters (Lander & Jones 2009; Gourgouliatos et al. 2013; Armaza et al. 2015; Fujisawa et al. 2012) and Θ is the heaviside function. This form ensures there are no toroidal currents outside the star. The value of $\alpha(1, 0)$ is self-consistently calculated at each iteration. This form of β also makes the source term non-linear. Solving a PDE with non-linear source terms is a challenging task and we follow the procedure of Mazumdar (2015) to linearise the process. To do so, we expand the source term, namely Q, in Taylor's series

$$Q_{ij}^k = Q_{ij}^{k-1} + \frac{dQ}{d\alpha}\Big|^{k-1}(\alpha_{ij}^k - \alpha_{ij}^{k-1}) + \dots = Q_c + Q_p\alpha_{ij}^k, \quad (15)$$

and neglect the contributions from higher order terms in α. We define

$$Q_c = Q_{ij}^{k-1} - \frac{dQ}{d\alpha}\Big|^{k-1}\alpha_{ij}^{k-1}, \quad (16)$$

$$Q_p = \frac{dQ}{d\alpha}\Big|^{k-1}, \quad (17)$$

and bring $Q_p\alpha_{ij}^k$ on the left-hand side of equation 13, modifying the coefficient ω_{ij} and the source term such that

$$\omega_{ij} = \omega_{ij} - \min(0, Q_p), \quad (18)$$

$$Q_{ij} = Q_c + \max(0, Q_p)\alpha_{ij}^{k-1}. \quad (19)$$

This step does not always guarantee convergence. To improve the performance of our solver, we use an under-relaxation scheme such that

$$\alpha_{ij}^k = \xi\alpha_{ij}^k + (1 - \xi)\alpha_{ij}^{k-1}, \quad (20)$$

where the parameter ξ lies between 0 and 1. The exact value of ξ depends on the problem and generally a smaller value like 0.1 would make the convergence slower but more accurate. We solve equation 13 until a tolerance limit is reached,

$$\frac{\alpha_{ij}^k - \alpha_{ij}^{k-1}}{\alpha_{ij}^{k-1}} \leq \varepsilon = 10^{-8}, \quad (21)$$

where the error at each step is computed as

$$\varepsilon = \sqrt{\frac{\sum_{i,j}(\alpha_{ij}^k - \alpha_{ij}^{k-1})^2}{\sum_{i,j}(\alpha_{ij}^{k-1})^2}}. \quad (22)$$

We have developed Python code[a], which is a widely used programming language known for its easily available numerical and scientific modules for computing. Instead of looping in the $r - \mu$ plane and calculating each α_{ij} term one at a time, we use numpy (Harris et al. 2020) vectorisation allowing for operations on the entire array at once. This speeds up the code by a factor of 100 for a grid of 50×50 and the improvement is more significant for a larger grid size, say 100×100 or 200×200. Additionally, we have the same version in C++ which is faster than Python and can be used for larger grid dimensions required to resolve strong toroidal fields.

4. Results

Given an EOS for a NS, one can solve the Tolman–Oppenheimer–Volkov (TOV) equations to obtain the mass (M), radius (R) and density profile (ρ) of the NS. This information is used as the background model on which we solve the GS equation to obtain the equilibrium magnetic field structure. In this paper, as we are solving Newtonian equations of motion, we use a set of EOSs that are analytically tractable and allow to mimic the the structure of fully relativistic solutions. In particular we produce models with three EOS. First of all, we use two particular exact solutions of the Einstein field equations which are of interest for a NS: the first known as the 'Schwarzschild' solution gives $\rho = \rho_c = $ const and the other obtained by Tolman (1939) gives $\rho(r) = \rho_c(1 - r^2/R^2)$, which is close to the density profile for the polytropic EOS $P(\rho) \sim \rho^2$, and has been used previously in several studied of magnetised neutron stars (Mastrano & Melatos 2012; Mastrano et al. 2013). We verify this explicitly by also producing a third set of equilibrium models for an $n = 1$ polytropic EOS which is obtained
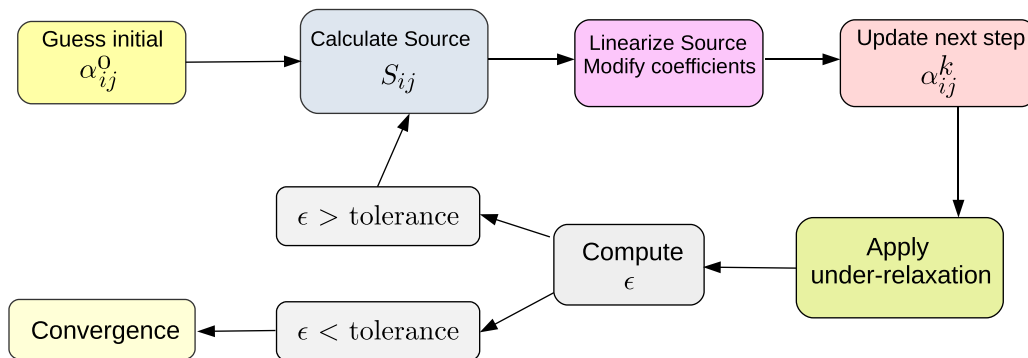
Figure 1. Flowchart of our numerical algorithm.

by solving the Lane–Emden equation giving $\rho = \rho_c \frac{sin(\pi r/R)}{\pi r/R}$. This allows us to maintain a physically plausible density profile, and an analytically tractable model, where we can arbitrarily choose M and R to match the compactness predicted by microscopic EOSs, without the technical difficulties associated with the use of a tabulated EOS in our scheme. Unless otherwise stated, we consider as our standard model a NS made of two different regions, a crust of thickness 1 km and a core of thickness 9 km with the crust–core interface having a density $\rho_{cc} \sim 1.9 \times 10^{14}$ gm cm^{-3} and $\rho_c \approx 10^{15}$ gm cm^{-3}. All the radial values r appearing hereafter have been normalised by the radius of the star R.

The age during which a realistic NS attends Hall/MHD equilibrium depends on its magnetic field strength (B). Typically, in a NS with an age of 10^3–10^5 yrs having $B \geq 10^{14}$ G, the Hall term dominates over the Ohmic dissipation term. However, in a NS with and Ohmic timescale of a billion years, the Hall term can still dominate for weaker field strengths, for example, in pulsars with $B \sim 10^{12}$ G, as the internal temperature is lower and of the order 10^7–10^8 K. Nore that although the Hall term is independent of the internal temperature (T_{in}), the magnetic and thermal evolution of a NS are coupled (Viganò et al. 2013), as the magnetic diffusivity (which we neglect) is strongly dependent on the internal temperature. In practice for the realistic systems we consider, we require $T_{in} \lesssim 10^8$ K, which also ensure the core temperature is well below the critical temperature for proton superconductivity.

In this section, we discuss axisymmetric solutions for the three different models: (a) Normal matter in the crust and the core—this includes both the case of standard MHD equilibria, and Hall equilibria, (b) Hall in the crust and MHD in the core, and the more realistic case, and (c) Hall equilibrium in the crust and a superconducting core.

4.1. Normal matter in crust and core

In this section, we consider a star composed of normally conducting matter in both the crust and the core. We show results for the Hall equilibrium, however these results can be easily extrapolated to MHD equilibrium, by replacing n_e with $\rho = \rho_c(1 - r^2)$, replacing $\chi_{MHD} = Y_e \chi_{Hall}$ and changing the constants given as $\lambda_{MHD} \rho_c R^2 = B_0'$.

In the following we choose $\chi_{Hall}(\alpha) = \lambda_{Hall}\alpha$ and set $\lambda_{Hall} = 10^{-35}$ G cm. This constant λ_{Hall} sets the strength of the magnetic field (B_0). As mentioned before, we present results for the Hall equilibria models with two different electron density profiles, one constant in space $n_1 = n_e$, and the other radially decreasing

profile $n_2(r) = n_e(1 - r^2)$ inside the NS. We also show results for the EOS with matter density following the $n = 1$ polytrope. We solve equation 8 with the α and β normalised by B_0/R^2 and B_0/R, respectively. The normalisation constant n_e of the electron density profile, with typical values $10^{36} - 10^{34}$ cm^{-3} across the crust, appears as $\lambda_{Hall} n_e R^2 = B_0$. For a star with radius $R = 10$ km, we get $B_0 \sim 10^{13}$ G which corresponds to a surface field strength of $\sim 10^{11}$G. The results we obtain are scalable to any field strength B_0 which doesn't influence our magnetic field topology but results in changing the quadrupolar deformation which we calculate later in Section 4.4. The normalised GS equation for the Hall equilibria is given by

$$\Delta^\star \alpha = -\left(\frac{\lambda_{Hall} \, n_e \, R^2}{B_0}\right) r^2 (1 - \mu^2) n(r) - \beta\beta'. \tag{23}$$

We consider now results for the whole star, i.e., $r_{min} = 0$, since it provides simpler analytical expressions.To compare with previous studies we choose $p = 1.1$. A lower value of p, in principle, develops stronger toroidal field. However p cannot be less than 0.5 as it makes the term $\beta'\beta$ infinite in certain regions inside the star (Gourgouliatos et al. 2013). For $n_1 = 1$, a purely poloidal field ($s = 0$) has an analytical solution given by Gourgouliatos et al. (2013)

$$\alpha(r, \mu) = \begin{cases} \frac{(1-\mu^2)}{30}(5r^2 - 3r^4) & \text{if } r < 1 \\ \frac{(1-\mu^2)}{15}\frac{1}{r} & \text{if } r \geq 1. \end{cases} \tag{24}$$

This is represented by the black line while the numerical calculations are shown by the green triangles in Figure 2. In Figure 3, we compare the radial and angular variation of the poloidal field for the two electron density profiles. We show results for different values of $s \in [0, 10, 20, 30, 40, 50, 60, 80, 90]$. First, varying the electron density yields a weaker poloidal field. Second, a higher value of s makes the poloidal field stronger with its maximum value lying at the equator as seen in sub-figures 3b, 3d and 3f. This is in good agreement with the results obtained by Gourgouliatos et al. (2013). However, on increasing $s > 80$, we do not see a further rise in the peak of poloidal field strength. Moreover, the results in Figure 3d show qualitative convergence as we increase the value of s, from which we conclude that models with $s \sim 50$ may be used as a reasonable approximation for the field structure. The geometry of the field lines for these different cases are shown in Figures 4, 5, and 6, for $s \in [0 - 90]$, with the colourscale representing the strength of β which is directly proportional to the toroidal field strength. The toroidal component is concentrated close to
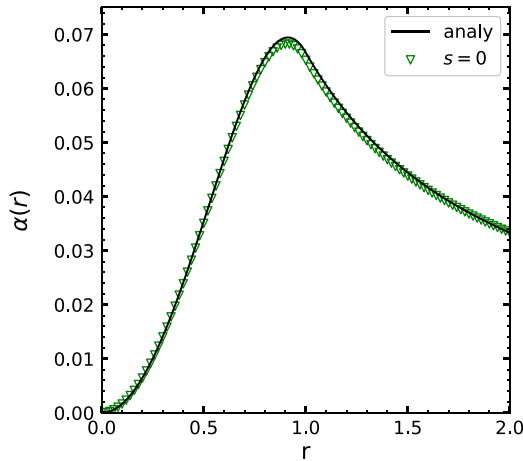
Figure 2. Variation of α (contours of which give the poloidal field lines) at the equator across the radial direction for the constant electron density profile. The black solid line shows the analytical solution.

the stellar equator and lies along the neutral line where the innermost closed poloidal field line is located within the star. This is however not surprising since we chose to have no currents outside the star. These figures also show that increasing s makes the region containing the toroidal field smaller as predicted by previous studies (Lander & Jones 2009; Gourgouliatos et al. 2013; Armaza et al. 2015). The toroidal region is also larger for the radially varying density profile n_2 when compared with the constant profile n_1. We compare our results directly with Gourgouliatos et al. (2013); Armaza et al. (2015) in table 1 where we show the percentage of the toroidal magnetic energy ($\mathcal{E}_{tor}$) to the total magnetic energy ($\mathcal{E}_{mag}$) with a fixed background density. The energies are comparable which shows that our results are consistent.

On comparing Figure 3c and 3e, we see that the maximum value of α across the equatorial region is lower for the density profile $\rho_2(r) \propto \frac{sin(\pi r)}{\pi r}$ when compared to $n_2(r) \propto (1 - r^2)$. This corresponds to a weaker poloidal and toroidal component however on comparing the fraction of toroidal energy with different values of s as seen in Figure 7, we see that the energies are comparable which assures our assumption that both these density profiles resemble each other.

We remark again that as we have assumed that density to be a function of radius only, the pressure and gravity forces are also radial and hence cannot balance the angular component of the magnetic force. In principle these forces will deform the star and lead to an ellipticity, and one should also solve the evolution equation for the density (Lander & Jones 2009). However, for the magnetic fields in regular pulsars, magnetic equilibrium can be treated as a perturbation on the background (Akgün et al. 2013). Deformations of the density profile are of the higher order in B^2, and any back-reaction on the field is even smaller, $O(B^4)$, and hence will only play a role for very strong magnetic fields in magnetars.

We have explored a different twisted-torus geometry with a continuous toroidal field $\beta(\alpha) = \gamma\alpha(\alpha/\bar{\alpha} - 1)\Theta(\alpha/\bar{\alpha} - 1)$ where $\bar{\alpha}$ is the value at the last closed field line and γ is a constant. This entire framework was carried out in general relativity by Ciolfi & Rezzolla (2013)(C&R) which we try to reproduce in the Newtonian limit. Previously, we have seen that with increasing s, the toroidal field becomes stronger and the closed field line region shrinks. To produce a larger closed field line, C&R considered a

functional dependence of $\chi(\alpha) = c_0[(1 - |\alpha/\bar{\alpha}|)^4\Theta(1 - |\alpha/\bar{\alpha}|) - \bar{k}]$, with c_0 and $\bar{k}$ are constants. Furthermore the transformation $\chi(\alpha) = \chi(\alpha) + \bar{\chi}(\alpha)$ was applied, with $\bar{\chi} = X(\alpha)\beta'\beta$, thus minimising the effect of toroidal fields on the poloidal field lines. With $\gamma = 1$, $c_0 = 1$, $\bar{k} = 0.03$, and $X(\alpha) = 1$ we solved the GS equation and get $\mathcal{E}_{tor}/\mathcal{E}_{mag} \sim 0.05$ instead of the very strong toroidal fields $\mathcal{E}_{tor}/\mathcal{E}_{mag} \sim 0.6$ obtained by C&R (Ciolfi & Rezzolla 2013).We do not solve our equations in GR and cannot conclusively say what could give rise to this discrepancy.

4.2. Hall equilibria in crust and MHD in core

As a first step towards more realistic models, we start by considering the case where we have a Hall equilibrium in the crust, and an MHD equilibrium in the core of the star. We follow Fujisawa & Kisaka (2014) who showed that the strength and structure of magnetic field in the core affects that in the crust, and the current sheet at the crust–core interface affects the internal and external field. Similarly, we look into a situation where we impose Hall equilibrium in the crust and MHD equilibrium in the core. Outside the star, we assume vacuum condition, in which case, we solve $\Delta^\star\alpha = 0$ with the zero boundary conditions for α at a far away radial point. One can also impose a dipolar field however the results do not change significantly as seen by Gourgouliatos et al. (2013).

In order to study this case we now have to, unlike in previous examples, explicitly differentiate between Hall and MHD equilibria. The equations we solve are given by

$$\Delta^\star\alpha = -r^2(1 - \mu^2)n(r)\chi'_{\text{Hall}} - \beta\beta' \quad \text{in crust,} \quad (25)$$

$$\Delta^\star\alpha = -r^2(1 - \mu^2)\rho(r)\chi'_{\text{MHD}} - \beta\beta' \quad \text{in core.} \quad (26)$$

At the crust–core interface, the continuity of α is automatically imposed. We also want the magnetic field in the core and the Lorentz force in the crust to balance, which gives

$$\left[\rho_{\text{core}}\, \chi'_{\text{MHD}}\right]^{cc} = \left[n_{\text{crust}}\, \chi'_{\text{Hall}}\right]^{cc}. \quad (27)$$

We set the electron density in the crust to be a constant $n_{\text{crust}} = n_e$ while the density in the core is assumed to follow $\rho_{\text{core}} = \rho_c(1 - r^2)$. With the crust–core boundary at $r = 0.9R$, using equation 27 we get the following relation:

$$\chi'_{\text{MHD}} = 5.1 \times 10^{21}\chi'_{\text{Hall}} \sim 5.1 \times 10^{-14}\,\text{G cm}^{-1}. \quad (28)$$

The magnetic field lines remains unchanged however the strength of the parameter β is significantly higher as seen in Figure 8.

We plot the percentage fraction of toroidal energy for the pure Hall+MHD in Figure 9 and compare this with the pure Hall equilibrium NS. The difference between this setup compared to purely MHD or Hall equilibria is that the toroidal energy density is stronger up to $s \sim 40$, but starts decreasing for higher values. Qualitatively, however, the results are similar and the toroidal energy saturates at a few percent of the total energy.

4.3. Hall equilibrium in crust and Superconducting core

As the NS cools down, neutrons and protons form pairs by reducing their energy owing to the long range attractive part of the residual strong interactions. The thermal energy in this case is much smaller than the pairing energy and the system is gaped,
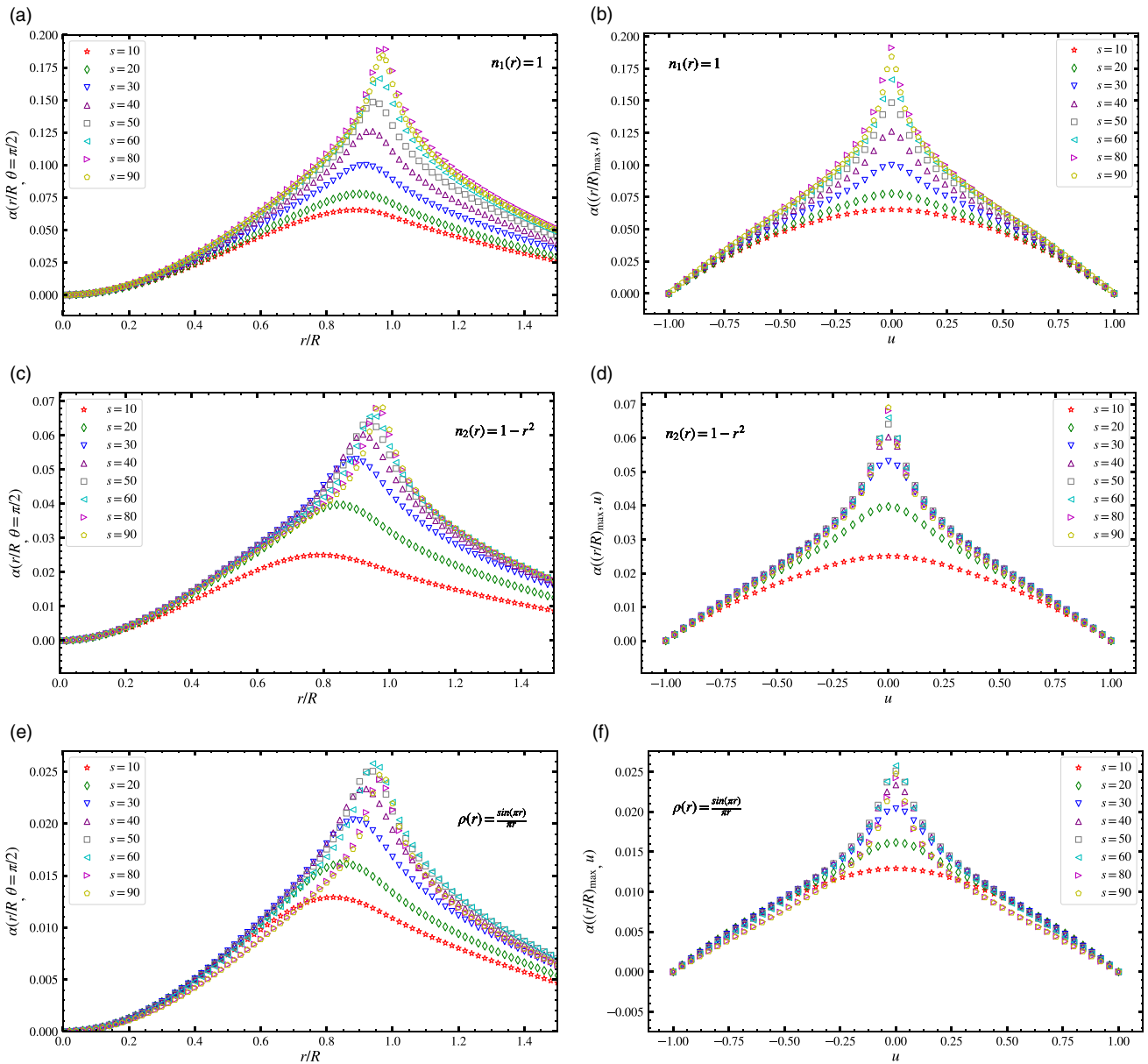
Figure 3. Variation of α (whose contours give the poloidal field lines) at the equator across the radial direction for eight values of the parameter s shown for three different density profiles in (a),(c), and (e). Variation of the maximum value of α across the angular direction with s. The density profiles are given as text in each figure.

which leads to reactions and viscosity being greatly suppressed. As previously mentioned, the transition temperature below which the system behaves as superfluid/superconductor is typically $T_c \sim 10^9 - 10^{10}$ K, and the star thus cools below this rapidly after birth. In the interior of a mature neutron star the geometry of the magnetic field depends on the type of superconductivity, which in turn depends on the size of Cooper pairs and the penetration depth of the magnetic field. This is measured with the Ginzburg–Landau parameter κ_{GL} which for NS cores is greater than $1/\sqrt{2}$ making it a type-II superconductor (for an in depth discussion, see the review article by Haskell & Sedrakian (2018)).

In order to obtain a more realistic model of a pulsar, we thus consider a core of type-II superconducting protons, and study its effect on the magnetic field equilibria, following the setup of Lander (2013, 2014). Therefore, our star is made up of normal matter in Hall equilibrium in the crust and superconducting matter in the core. The crust–core interface lies at $r = 0.9$ as in previous cases. Our models, in this case, are valid for pulsars having a surface field strength of $(1 - 10) \times 10^{11}$ G with typical ages in the range of $10^4 - 10^5$ yrs and internal temperatures of $10^7 - 10^9$ K. The Lorentz force for this type-II superconducting protons in the core is given by (Easson & Pethick 1977; Mendell 1991; Akgün & Wasserman 2008; Glampedakis et al. 2011)

$$\vec{F}_{\text{mag}} = -\frac{1}{4\pi}\left[\vec{B} \times (\vec{\nabla} \times \vec{H}_{cl}) + \rho_p \vec{\nabla}\left(B\frac{\partial H_{c1}}{\partial \rho_p}\right)\right], \qquad (29)$$

where $\vec{H}_{cl}(\rho_p, \rho_n) = H_{c1}\hat{B}$ is the first critical field with $\hat{B}$ is the unit vector tangent to the magnetic field. The norm of this first critical
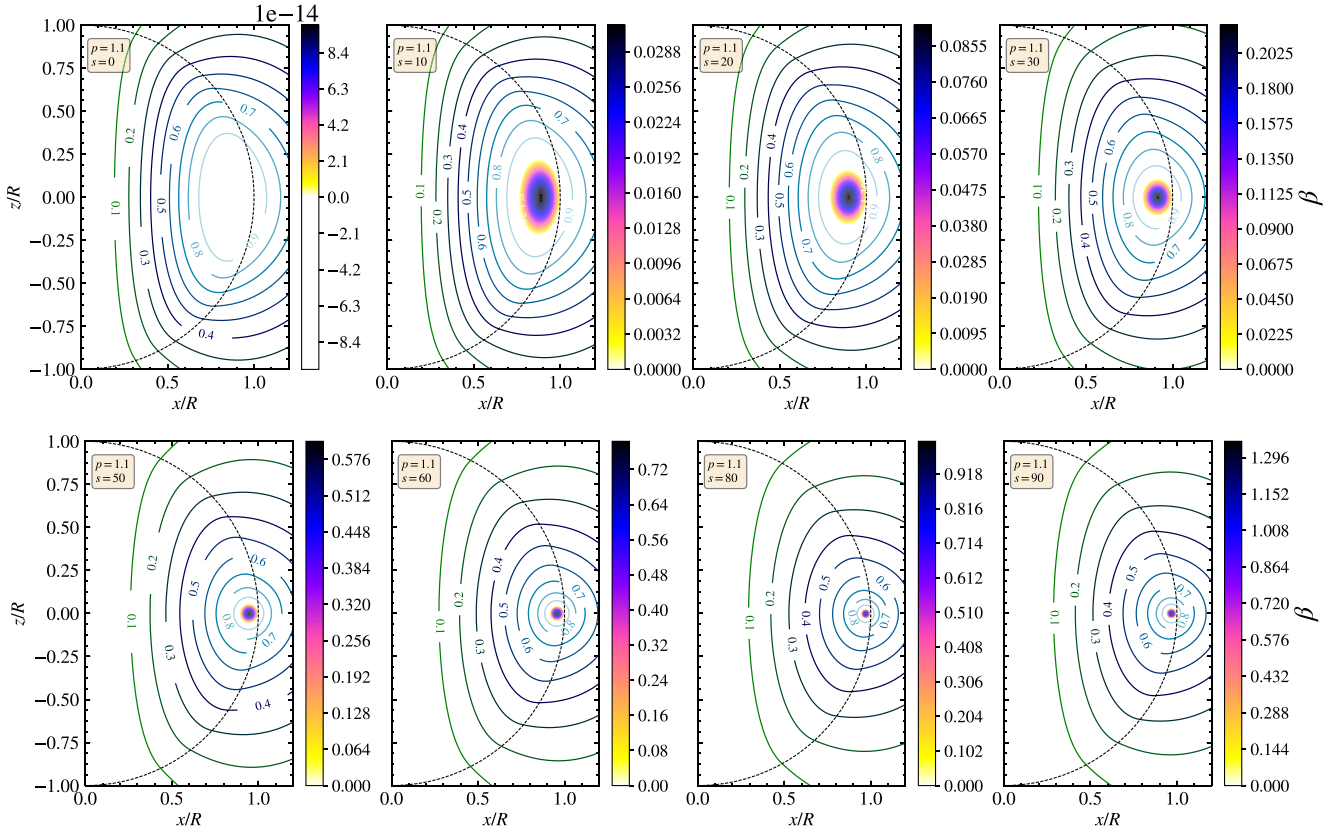
Figure 4. Contours of poloidal field for different values of s (given in the text box in each figure) using the constant electron density profile $n_1 = 1$. The colourbar shows the strength of β. The black dotted line represents the location of stellar radius. We have shown contours of α having values ($0.1\alpha_s, 0.2\alpha_s, 0.3\alpha_s, 0.4\alpha_s, 0.5\alpha_s, 0.6\alpha_s, 0.7\alpha_s, 0.8\alpha_s, 0.9\alpha_s, 1\alpha_s$).

field is given as

$$H_{c1}(\rho_n, \rho_p) = h_c \frac{\rho_p}{\varepsilon_\star}, \qquad (30)$$

where h_c is an arbitrary constant (Glampedakis et al. 2011). We assume that the density of protons ρ_p in the core follows the same profile $\approx (1 - r^2)$ as that by electrons in the crust. The entrainment parameter is given by $\varepsilon_\star = \frac{1 - \varepsilon_p - \varepsilon_n}{1 - \varepsilon_n}$, where $\varepsilon_p = 1 - \frac{m_p^\star}{m_p}$. Here $m_p^\star$ is the effective mass of the protons acquired as a result of entrainment. Similarly, we can define ε_n. We refer the reader to Palapanidis et al. (2015) where the effect of entrainment is discussed extensively. In the following, we simply set $\varepsilon_\star = 1$, which implies that force on neutrons due to coupling is zero which allows us to represent $H_{c1} = H_{c1}(\rho_p)$. The equivalent Grad–Shafranov equation for type-II superconducting core is thus given by

$$\Delta^\star \alpha = \frac{\vec{\nabla} \Pi \cdot \vec{\nabla} \alpha}{\Pi} - r^2 (1 - u^2) \rho_p \Pi \frac{dy}{d\alpha} - \Pi^2 f_{sc} \frac{df_{sc}}{d\alpha}, \qquad (31)$$

where we represent superconducting matter with the subscript sc and the functions f_{sc} and $y(\alpha)$ are defined as

$$y(\alpha) = 4\pi \chi_{sc} + B \frac{h_c}{\varepsilon_\star}, \qquad (32)$$

$$f_{sc}(\alpha) = \frac{\beta}{B} H_{c1}, \qquad (33)$$

where $B = \sqrt{\vec{B} \cdot \vec{B}}$) is the magnitude of the magnetic field and $\Pi = \frac{B}{H_{c1}}$. Equation 31 is valid in the NS core ($r < 0.9R$). For the crust, we consider normal matter in Hall equilibrium while the exterior remains the same as considered before. As previously remarked, we consider mostly the more realistic case of Hall equilibria, but our equations in general can be applied also to MHD equilibrium, in which case the boundary conditions are modified. In particular equation 40 becomes:

$$y(\alpha) = \frac{h_c}{\epsilon_\star} B_{cc}(\alpha) + 4\pi \left[\frac{\rho_p^{crust}}{\rho_p^{core}} \right]_{cc} \chi_{MHD}(\alpha), \qquad (34)$$

4.3.1. Boundary conditions

We treat the boundary conditions as outlined in (Lander 2014). At the surface of the NS, the density of protons vanishes. The magnetic field in the core and the Lorentz force in the crust must balance, which gives

$$\left[\rho_p^{core} \chi_{sc}' \right]^{cc} = \left[n_e^{crust} \chi_{Hall}' \right]^{cc}. \qquad (35)$$

Since *apriori*, we do not know B explicitly as a function of α, we use a polynomial approximation for B at the crust–core interface as given in (Lander 2014)

$$B_{cc}(\alpha) = c_0 + c_1 \alpha + c_2 \alpha (\alpha - \alpha_{cc}^{eq}), \qquad (36)$$
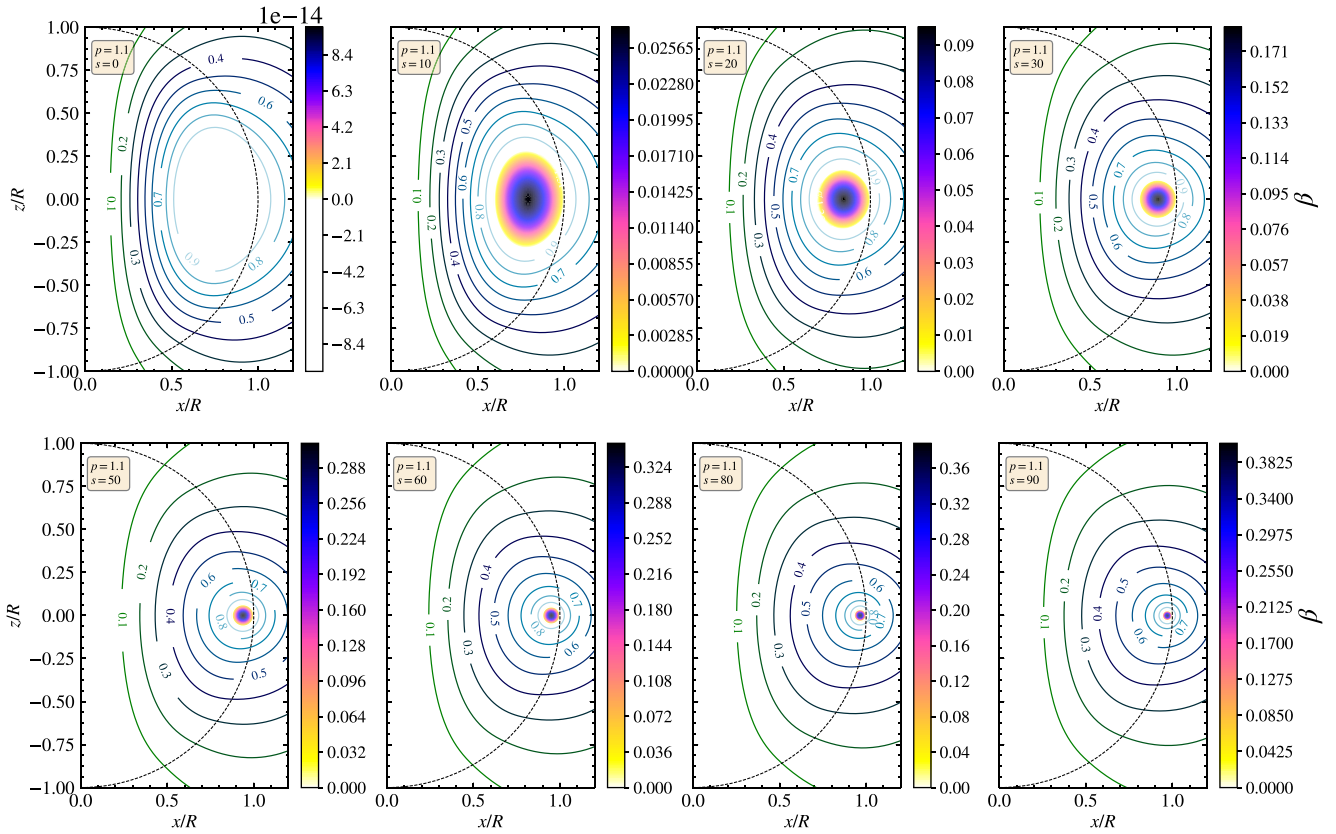
Figure 5. Contours of poloidal field lines (with similar strengths as above), for the electron density profile $n_2 = (1 - r^2)$. The colourbar, again, shows the strength of β and the red dotted line represent $r = R$.

where c_0 are constants and α_{cc}^{eq} is the equatorial value of α on the crust–core boundary. We choose the constant such that

$$c_0 = B_{cc}^{pole}, \tag{37}$$

$$c_1 = \frac{B_{cc}^{eq} - c_0}{\alpha_{cc}^{eq}}, \tag{38}$$

$$c_2 = \frac{B_{cc}^{mid} - c_0 - c_1\alpha_{cc}^{mid}}{\alpha_{cc}^{mid}(\alpha_{cc}^{mid} - \alpha_{cc}^{eq})}, \tag{39}$$

where α_{cc}^{mid} is the value of α at $\theta = \pi/4$ in the crust–core boundary. This gives

$$y(\alpha) = \frac{h_c}{\epsilon_\star} B_{cc}(\alpha) + 4\pi \left[\frac{n_e^{crust}}{\rho_p^{core}} \right]_{cc} \chi_{Hall}(\alpha). \tag{40}$$

The next boundary condition that we must satisfy is the continuity of B_ϕ which is given by

$$f_{sc}(\alpha) = [H_{c1}]_{cc} \frac{\beta(\alpha)}{B_{cc}(\alpha)}. \tag{41}$$

4.3.2. Field lines

The poloidal field contours are shown in Figures 10a and 10b with the colourscale again representing the strength of β. This

corresponds to a maximum toroidal field of magnitude 10^{10} G. In the core, we see that the field lines are convex for the superconducting matter as opposed to the normal matter. The toroidal field is also restricted to the crust and cannot penetrate deep within the star. This can be understood by comparing the ratio of averaged magnetic field strength to the magnitude of H_{c1} at the crust–core interface, i.e., $\langle B^{cc} \rangle / H_{c1}^{cc} < 1$, which is typically the case for pulsars. $\langle B^{cc} \rangle / H_{c1}^{cc} \geq 1$ makes the field lines kink inwards and close inside the core (Lander 2014). This effect is independent of the choice of our function $\chi_{MHD}(\alpha)$. In this study, we typically have H_{c1} 10–50 times stronger than the magnitude of B at the crust–core interface, which increases the magnetic tension towards the z-axis. The toroidal flux is fully expelled to the crust, as also seen by Lander (2014), while magnetothermal evolutions by Elfritz et al. (2016) found on the contrary a toroidal field in the core. We note however that this result depends strongly on the intial conditions for the evolution in the core, and further analysis of their compatibility with the equilibria found here would be needed to obtain a full physical understanding of this discrepancy.

4.4. Magnetic deformation

Finally, let us discuss the magnetic deformation of the star, which plays an important role in estimating the strength of gravitational radiation from NSs (Ushomirsky et al. 2000; Haskell et al. 2008; Mastrano et al. 2013; Lasky 2015; Gao et al. 2017; Sieniawska &
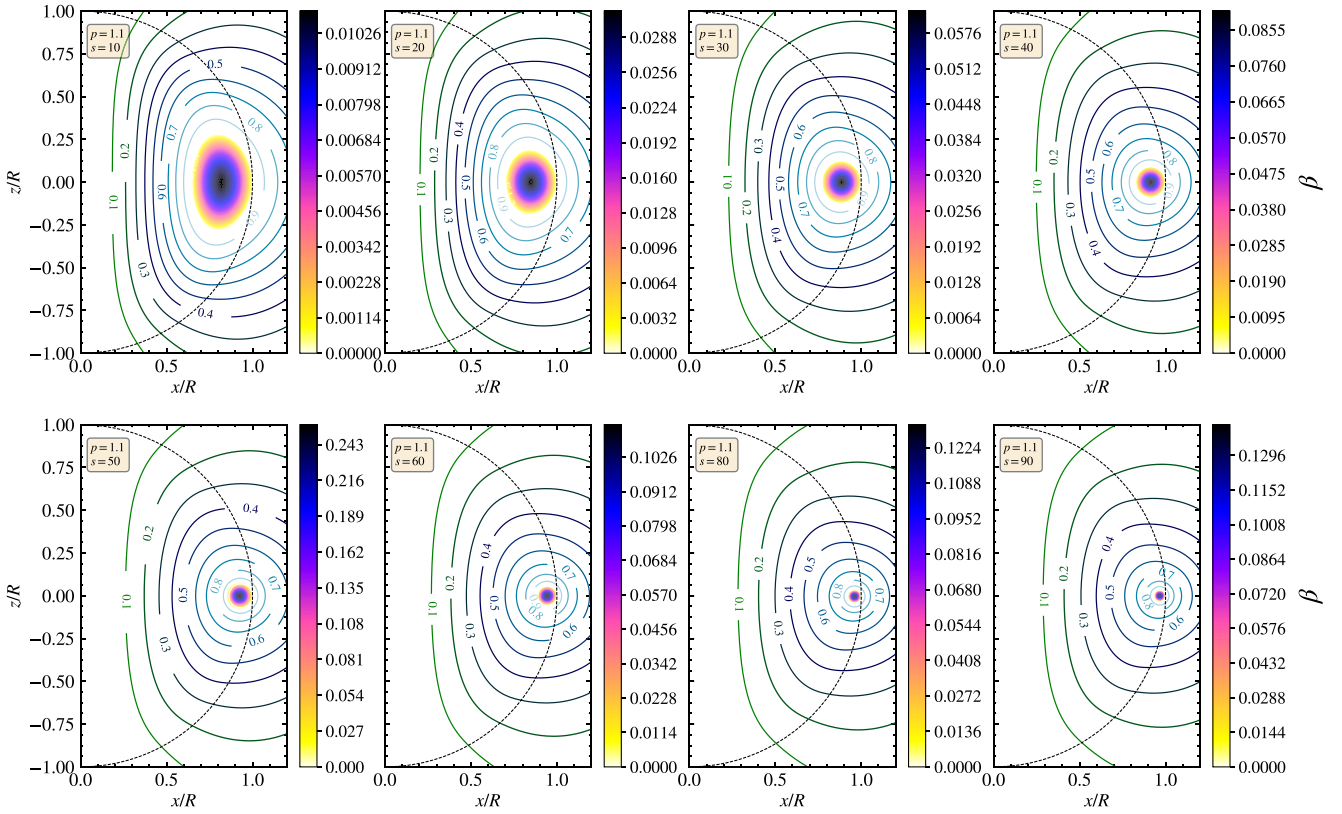
Figure 6. Contours of poloidal field lines with different s values for the $n = 1$ polytropic density profile $\rho = \rho_c \frac{\sin(\pi r/R)}{\pi r/R}$. The colourbar, again, shows the strength of β and the red dotted line represent $r = R$.

Table 1. The percentage of $\mathcal{E}_{tor}/\mathcal{E}_{mag}$ for different parameter values of s for $n_2(r) = (1 - r^2)$. A comparison is also shown with Armaza et al. (2015) and Gourgouliatos et al. (2013).

s	This work	Armaza	Gourgouliatos
0	0	0	0
5	0.12	0.14	0.15
10	0.65	0.57	0.60
20	2.2	2.2	2.3
25	3.1	3.1	3.2
30	3.3	3.7	3.9

Figure 7. Percentage fraction of the toroidal magnetic energy ($\mathcal{E}_{tor}$) to the total magnetic energy $\mathcal{E}_{mag}$) for two different density profiles given in figure labels for the setup given in Subsection 4.1.

Bejger 2019; Chandra et al. 2020). In our setup, as already discussed, this can be treated as a higher order effect in an expansion in $O(B^2)$. The strategy is thus to compute the magnetic field on a spherical background, as we have done in the previous section, and then evaluate the deformations of the density profile at $O(B^4)$. Following Haskell et al. (2008), the theta component of the Lorentz force (L_θ) term is given by

$$(\delta p + \rho \delta \Phi)\frac{dY_2^0}{d\theta} = r\frac{[(\vec{\nabla} \times \vec{B}) \times \vec{B}]_\theta}{4\pi} = \frac{rL_\theta}{4\pi}. \quad (42)$$

where Y_2^0 is the $m = 0$ spherical harmonic. We further impose the Cowling approximation which gives $\delta\Phi = 0$ and on using the EOSs considered in this work, we calculate the quadrupole

moment, following Ushomirsky et al. (2000), as

$$Q_{lm} = \int_0^R \delta\rho_{lm}(r)r^{l+2}dr, \quad (43)$$

which on dividing by the zth component of the moment of inertia (I_{zz}), gives us the ellipticity parameter $\epsilon = Q_{20}/I_{zz}$. Note that our models are axisymmetric, and would not lead to gravitational

Figure 8. Magnetic field lines and the strength of β for the Hall equilibrium in the crust and MHD equilibrium in core.
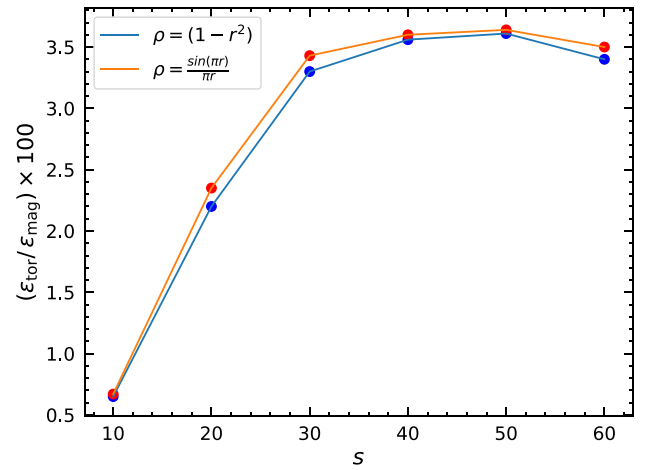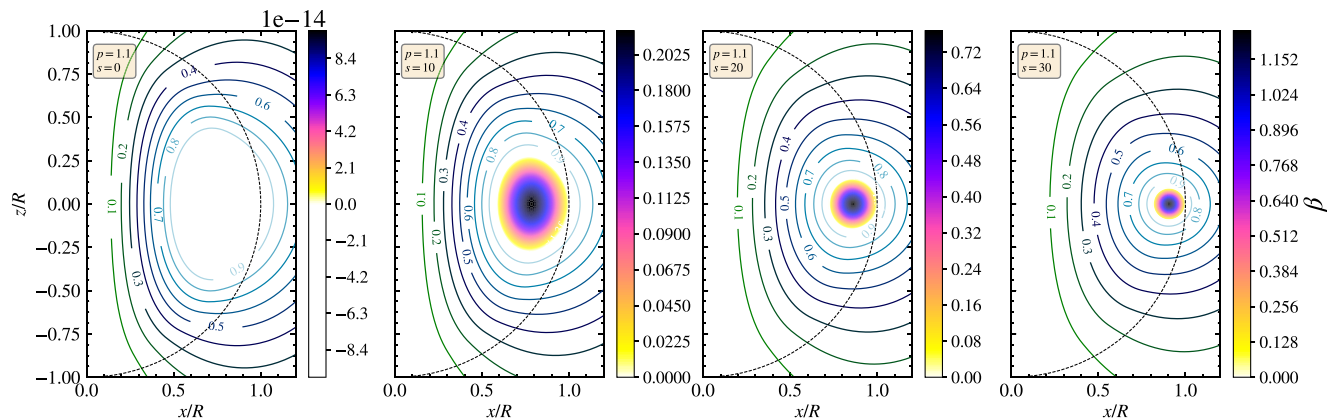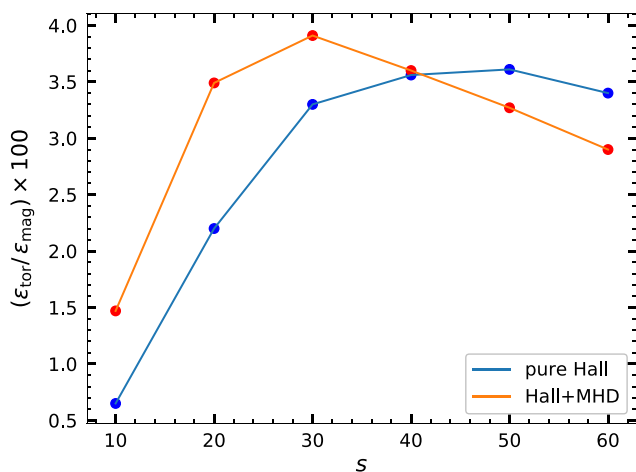

Figure 9. Percentage fraction of the toroidal magnetic energy ($\mathcal{E}_{tor}$) to the total magnetic energy $\mathcal{E}_{mag}$) for the pure Hall (setup in 4.1) and mixed Hall+MHD (setup in 4.2) with varying s.

This is significantly lower than the results obtained by Suvorov et al. (2016) who found $\epsilon \sim 10^{-6}$ from spot-like magnetic field structures present in the crust due to Hall effect causing density perturbations for field strengths higher than $B \geq 10^{14}$ G. This difference is likely to be caused by the interplay between the overall stronger poloidal field in the core of the star and the (locally) strong toroidal field in the crust which compensate each other in our model, while Suvorov et al. (2016) consider fields only in the crust of the star, and non-barotropic equations of state. Nevertheless, a full magnetothermal evolution of the couple crust–core system would be needed to conclusively shed light on the issue.

Note finally that in the MHD model, the toroidal field regions of the star can present locally large deformations of density (up to $\delta\rho/\rho \approx 0.01$), which could be important in older, accreting systems, as if they occur in the crust they could lead to deformed capture layers in the presence of accretion (Singh et al. 2020). However, in our more realistic models with a superconducting core, these deformations are much smaller, and never larger than $\delta\rho/\rho \approx 10^{-6}$.

4.5. Code performance

We compare our two codes in Python and C++. In Figure 11a, we show the number of iterations taken for each code to reach an error (ε) for three different grid sizes for $s = 5$. In Figure 11b, we plot error as a function of number of iterations for two different cases, purely poloidal ($s = 0$) and a mixed poloidal–toroidal ($s = 5$). The grid size chosen was 101×101. Overall we infer that the performance of C++ is better as it takes less number of iterations (and hence time) to reach our final tolerance. However, for the purely poloidal case, we see that our Python code, which uses <monospace>numpy</monospace> vectorisation, is faster when compared to C++. Further we calculated the order of convergence $oc = \ln\left(\frac{f_3 - f_2}{f_2 - f_1}\right)/\ln(r)$, where $f3$, $f2$ and $f1$ are values at a fixed point in the grid with resolutions 128×128, 64×64 and 32×32 respectively. Here r is the refinement ratio chosen to be 2, and we find $oc \sim 2$, showing second-order convergence ($\mathcal{O}(h^2)$).

wave emission, even in the presence of a significant deformation. However, if the magnetic axis is not aligned with the rotational axis, the deformation will not be axisymmetic and there will be components of the quadrupole also with $m \neq 0$, leading to emission at both the rotational frequency and twice the rotational frequency of the star (Bonazzola & Gourgoulhon 1996). In order to obtain an estimate of the ellipticity, we thus make the standard approximation that $Q_{20} \approx Q_{01}$, neglecting geometric factor that depend on the inclination angle.

We can now compare the quadrupoles obtained for our setups with Hall equilibrium in the crust, but with MHD and superconducting cores. The results are very similar for the densities $\rho \sim (1 - r^2)$ and $\rho \sim \sin(\pi/r)/\pi r$, and for $s = 10$, we obtain for the MHD core $\epsilon \approx 2 \times 10^{-12}$, corresponding to an average poloidal field of $B_p = 6 \times 10^{11}$ G (with a surface value of $B_s = 2 \times 10^{11}$ G) and toroidal field of $B_t = 5 \times 10^{10}$ G, which is in line with theoretical expectations. For our setup with a superconducting core we obtain, taking $H_c \sim 10 B_0$, values of $\epsilon \approx 7 \times 10^{-11}$, for $B_p = 4.3 \times 10^{11}$ G, $B_t = 3 \times 10^{10}$ G, and a surface field of $B_s = 3 \times 10^{11}$ G.
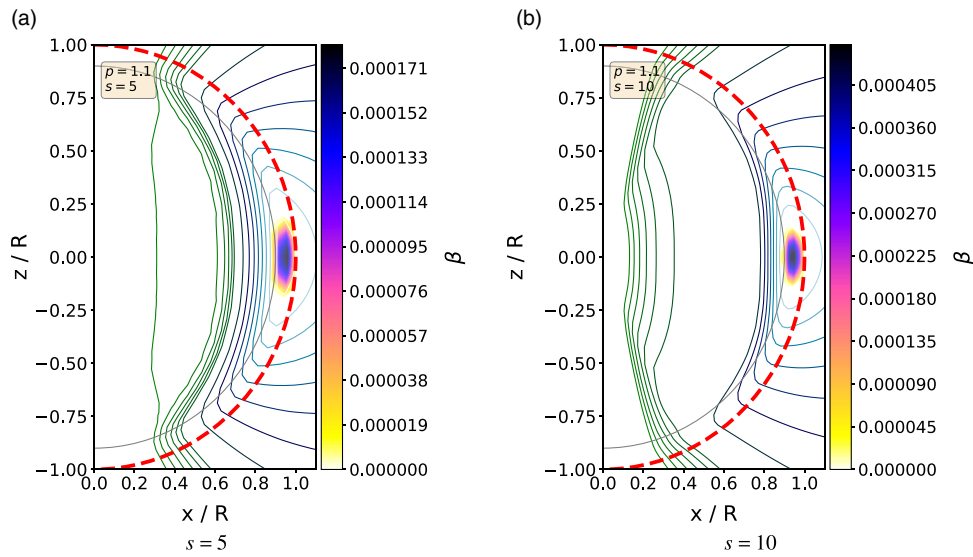
Figure 10. Contours of poloidal field lines for two different values of s in the superconducting core Hall equilibrium crust. The location of the crust–core interface is represented by the solid grey line at $r = 0.9R$, while the red dotted line shows the stellar surface. The colourscale represents the strength of the toroidal field β.
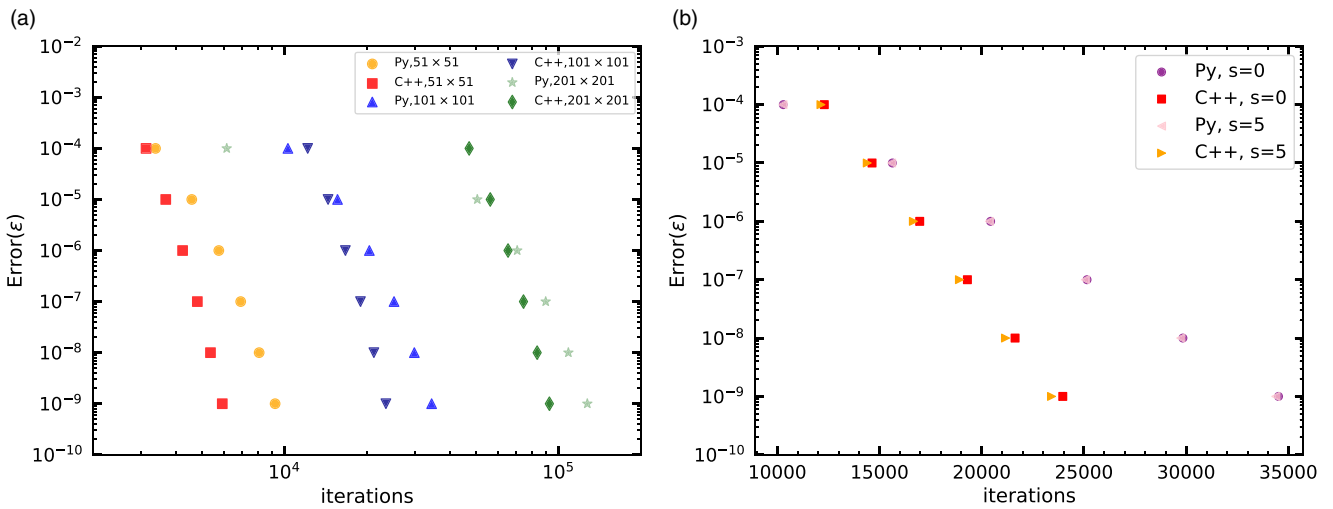

Figure 11. (a) Number of iterations as a function of accuracy for three different grid sizes for the two versions of our code. (b) The number of iterations taken by our solvers to reach a certain accuracy when generating different field geometries, purely poloidal ($s = 0$) and the mixed poloidal–toroidal($s = 5$).

5. Conclusion and discussions

In this paper, we have developed a numerical scheme to rapidly solve the GS equation to obtain axisymmetric magnetic field equilibrium models for mature neutron stars. As a benchmark for our code we first consider first the case of pure MHD equilibria and pure Hall equilibria, then move on to models in which we solve for Hall equilibrium in the crust and MHD equilibtium in the core. Finally, we produce for the first time a model where we consider a type-II superconducting core and Hall equilibrium in the crust, thus producing a more realistic model for a mature pulsar.

We compared our numerical computations with analytical solutions provided by Gourgouliatos et al. (2013) and with the results obtained by Armaza et al. (2015) which shows excellent agreement. Since our source terms have a high-degree of non-linearity, we have implemented a new technique which allows us to linearise our source. This, along with the under-relaxation to update α had significantly improved our solver's performance. We were able to extend calculations for $s > 65$, i.e., regions where previous studies (Armaza et al. 2015; Gourgouliatos et al. 2013) had failed, for the normally conducting fluid. We reach convergence when $s \sim 50$ and the results do not change significantly beyond this value of s. However, our code fails when we increase s beyond 90 for $p = 1.1$ because the toroidal field region became too small to be resolved, causing numerical instabilities. We can do better if p is increased to 2, but this does not produce any difference in the toroidal component. In our calculations we implement both simplified equations of state, such as a constant density profile, in order to compare to previous results, but also more realistic profiles. In particular we implement a parabolic equation of state of the form $\rho \propto (1 - r^2/R^2)$ and compare the results to those obtained with an $n = 1$ polytrope, and find them to be in good agreement.

In this work, we have assumed the star to be always spherical. There are a few limitations of this as our results do not account for the back-reaction of the magnetic force on the fluid, and so we cannot self-consistently calculate ellipticities for strong magnetic fields, such as those of magnetars, where our perturbative approach is no longer valid. To consistently account for the effect of non-sphericity in the presence of strong fields or rotation, it would be necessary to modify our method to calculate simultaneously the density and field structure (Lander & Jones 2009). Nevertheless our method can be confidently applied to the standard pulsar population, in which the magnetic fields are weak enough to enable a perturbative treatment, and rotationally induced deformations can safely be ignored.

We calculate magnetic equilibria solutions for the superconducting core NSs which differed from the normally conducting matter by field strengths and geometry of the poloidal field lines. The most notable change is that the toroidal field is expelled from the core and restricted to the crust in the case of where $\langle B^{cc} \rangle / H_{cl}^{cc} < 1$, which is applicable for the standard pulsar population. Increasing this ratio beyond 1 (as would be the case for magnetars) caused numerical difficulties and we leave it as a scope for improvement in the future. Furthermore for $B >> H_c$ even non-linear effects such as those considered bu Lander & Jones (2009) can be important, and further development of our scheme would thus be required to consistently describe magnetars.

To be precise, our Hall crust-superconducting core models are valid for middle-aged pulsars with ages of around 10^5 years and core temperature of $T \lesssim 10^9$ K. We consider surface values of the magnetic field os order $B_s \leq 10^{12}$ G. This guarantees that we are exploring a population which have a timescale for Hall evolution which is much shorter than the Ohmic dissipation timescale and we can ignore the latter contributions when computing our models.

Our results for superconducting cores and Hall equilibrium in the crust are, therefore, a realistic model for mature pulsars, and are particularly interesting for glitching pulsars. It has, in fact, been suggested that a strong toroidal field region in the core could lead to vortex/flux tube pinning, thus providing a large reservoir of angular momentum to power large glitches such as those observed in the Vela pulsar (Gügercinoğlu 2017; Gügercinoğlu & Alpar 2020), and possibly resolving the tension between the observed activity of the Vela (i.e., the amount of spin-down reversed by glitches during the observing period) and the angular momentum that theoretical models predict to be stored in the crust (Andersson et al. 2012; Chamel 2013). Our model, however, shows that no toroidal field area is present in the core to allow for such pinning, as it is expelled to the 'normal' matter crust. The models we produce can, however, be used as a background for more realistic vortex pinning calculations (Sourie & Chamel 2020a; Sourie & Chamel 2020b), in order to fully investigate the effect of pinning in the core on pulsar glitch phenomenology. Note, however, that for very strong surface magnetic fields (e.g., $B_s > 10^{15}$ G) like those seen in magnetars, the ratio $\langle B^{cc} \rangle / H_{c1}^{cc}$ is greater than unity and the toroidal flux is non-zero inside the core of the star (Lander 2014).

All our computations produced a toroidal field which is less than 5% of the total magnetic energy, and both the structure and strength of the field appear to rapidly converge to a qualitatively stable regime as we increase the degree of non-linearity by increasing the parameter s. This is in line also with the results obtained from numerical MHD evolution by Sur et al. (2020). We have also shown that we can have a stronger toroidal field for a model

with Hall equilibrium in crust and MHD equilibrium in the core of the star, and also tried to implement the formalism presented in Ciolfi & Rezzolla (2013) to generate extremely strong toroidal fields. We do not obtain results with toroidal energies significantly larger than $\simeq 5\%$ of the total magnetic energy of the star, although we do not work in GR and do not consider strong magnetic fields in our setup. This has strong implications as the gravitational wave emission, as the size of a 'mountain', i.e., of the quadrupolar deformation that couples to the gravitational field, strongly depends on the internal magnetic energy of a NS (Haskell et al. 2008).

We study such 'mountains' on the star by calculating the density and pressure perturbation induced at higher order by the field configurations we generate. This allows us to estimate the ellipticity, which in our case is $\in \approx 7 \times 10^{-11}$ in the superconducting case, for a surface field value of $B_s \approx 3 \times 10^{11}$ G, which is in line with theoretical expectations and confirms that if such deformations persist also in older pulsars, for which the crustal field may be buried leading to a lower inferred external dipole, this may explain the observed cutoff observed in the $P - \dot{P}$ diagram for millisecond pulsars by Woan et al. (2018).

We have written two versions of our code, one in C++ and the other in Python. To improve our Python code's performance, we vectorised our arrays to perform operations instead of using loops. The number of grid points play a major role in resolving the toroidal component. We needed finer mesh to obtain the strong toroidal fields wherein our C++ code was efficient. Using our Python code, we could solve the GS equation with parameters ($s = 0$, $p = 1.1$) for 101×101 grid to reach an accuracy of $\epsilon \sim 10^{-8}$ in less than 10 seconds. With the non-linear source, the Python solver took longer time and hence we used our C++ solver.

To summarise, we generated realistic magnetic equilibrium models in NSs with superconductiong cores, which could serve as initial conditions for long-term evolution of the magnetic field. This will bestow our understanding of the global magnetic field structure and its stability over the lifetime of a NS or any barotropic star.

Conflicts of interest. None.

References

Akgün, T., & Wasserman, I., 2008, MNRAS, 383, 1551

Akgün, T., Reisenegger, A., Mastrano, A., & Marchant, P. 2013, MNRAS, 433, 2445

Akgün, T., Cerdá-Durán, P., Miralles, J. A., & Pons, J. A. 2017, MNRAS, 472, 3914

Andersson, N., Glampedakis, K., Ho, W. C. G., & Espinoza, C. M. 2012, Phys. Rev. Lett., 109, 241103

Armaza, C., Reisenegger, A., & Valdivia, J. A. 2015, ApJ, 802, 121

Bonazzola, S., & Gourgoulhon, E. 1996, A&A, 312, 675

Braithwaite, J. 2009, MNRAS, 397, 763

Braithwaite, J., & Nordlund, Å. 2006, A&A, 450, 1077

Braithwaite, J., & Spruit, H. C. 2006, A&A, 450, 1097

Castillo, F., Reisenegger, A., & Valdivia, J. A. 2017, MNRAS, 471, 507

Castillo, F., Reisenegger, A., & Valdivia, J. A. 2020, MNRAS, 498, 3000

Chamel, N. 2013, Phys. Rev. Lett., 110, 011101

Chandra, P. V. S. P., Korwar, M., & Thalapillil, A. M. 2020, Phys. Rev. D, 101, 075028

Ciolfi, R., & Rezzolla, L. 2012, ApJ, 760, 1

Ciolfi, R., & Rezzolla, L. 2013, MNRAS, 435, L43

Ciolfi, R., Lander, S. K., Manca, G. M., & Rezzolla, L. 2011, ApJ, 736, L6

Coti Zelati, F., Rea, N., Pons, J. A., Campana, S., & Esposito, P. 2018, MNRAS, 474, 961

Cumming, A., Arras, P., & Zweibel, E. 2004, ApJ, 609, 999

Easson, I., & Pethick, C. J. 1977, Phys. Rev. D, 16, 275

Elfritz, J. G., Pons, J. A., Rea, N., Glampedakis, K., & Viganò, D. 2016, MNRAS, 456, 4461

Fujisawa, K., & Kisaka, S. 2014, MNRAS, 445, 2777

Fujisawa, K., Yoshida, S., & Eriguchi, Y. 2012, MNRAS, 422, 434

Gao, H., Cao, Z., & Zhang, B. 2017, ApJ, 844, 112

Glampedakis, K., Andersson, N., & Samuelsson, L. 2011, MNRAS, 410, 805

Glampedakis, K., Lander, S. K., & Andersson, N. 2014, MNRAS, 437, 2

Goldreich, P., & Reisenegger, A. 1992, ApJ, 395, 250

Gourgouliatos, K. N., & Cumming, A. 2014, Phys. Rev. Lett., 112, 171101

Gourgouliatos, K. N., Cumming, A., Reisenegger, A., Armaza, C., Lyutikov, M., & Valdivia, J. A. 2013, MNRAS, 434, 2480

Gourgouliatos, K. N., Wood, T. S., & Hollerbach, R. 2016, Proc. Nat. Acad. Sci., 113, 3944

Gruber, R., Iacono, R., & Troyon, F. 1987, J. Computat. Phys., 73, 168

Gügercinoğlu, E. 2017, MNRAS, 469, 2313

Gügercinoğlu, E., & Alpar, M. A. 2014, ApJ, 788, L11

Gügercinoğlu, E., & Alpar, M. A. 2020, MNRAS, 496, 2506

Gusakov, M. E., Kantor, E. M., & Ofengeim, D. D. 2017a, PhRvD, 96, 103012

Gusakov, M. E., Kantor, E. M., & Ofengeim, D. D. 2017b, Phys. Rev. D, 96, 103012

Gusakov M. E., Kantor E. M., & Ofengeim, D. D. 2020, MNRAS, 499, 4561

Harris, C. R., et al. 2020, arXiv e-prints, p. arXiv:2006.10256

Haskell, B., & Sedrakian, A. 2018, Superfluidity and Superconductivity in Neutron Stars, 401, doi: 10.1007/978-3-319-97616-7_8

Haskell, B., Samuelsson, L., Glampedakis, K., & Andersson, N. 2008, MNRAS, 385, 531

Hollerbach, R., & Rüdiger, G. 2002, MNRAS, 337, 216

Howell, E., & Sovinec, C. 2014, Comput. Phys. Commun., 185, 1415

Johnson, J., et al. 1979, J. Computat. Phys., 32, 212

Kaspi, V. M. 2010, Proc. Nat. Acad. Sci., 107, 7147

Kojima, Y., & Kisaka, S. 2012, MNRAS, 421, 2722

Kojima, Y., Kisaka, S., & Fujisawa, K. 2021, MNRAS, 502, 2097

Lander, S. K. 2013, Phys. Rev. Lett.,, 110, 071101

Lander, S. K. 2014, MNRAS, 437, 424

Lander, S. K., & Jones, D. I. 2009, MNRAS, 395, 2162

Lander, S. K., & Jones, D. I. 2012, MNRAS, 424, 482

Lasky, P. D. 2015, PASA, 32, e034

Lasky, P. D., Zink, B., Kokkotas, K. D., & Glampedakis, K. 2011, ApJ, 735, L20

Ling, K. M., & Jardin, S. C. 1985, J. Computat. Phys., 58, 300

Lyutikov, M. 2013, arXiv e-prints, p. arXiv:1306.4544

Marchant, P., Reisenegger, A., Valdivia, J. A., & Hoyos, J. H. 2014, ApJ, 796, 94

Mastrano, A., & Melatos, A. 2012, MNRAS, 421, 760

Mastrano, A., Lasky, P. D., & Melatos, A. 2013, MNRAS, 434, 1658

Mazumdar, S. 2015, Numerical Methods for Partial Differential Equations 1st Edition, Finite Difference and Finite Volume Methods. Academic Press, London

Melatos, A., & Peralta, C. 2007, ApJ, 662, L99

Mendell, G. 1991, ApJ, 380, 530

Mitchell, J. P., Braithwaite, J., Reisenegger, A., Spruit, H., Valdivia, J. A., & Langer, N. 2015, MNRAS, 447, 1213

Ofengeim, D. D., & Gusakov, M. E. 2018, Phys. Rev. D, 98, 043007

Osborne, E. L., & Jones, D. I. 2020, MNRAS, 494, 2839

Palapanidis, K., Stergioulas, N., & Lander, S. K. 2015, MNRAS, 452, 3246

Passamonti, A., Akgün, T., Pons, J. A., & Miralles, J. A. 2017, MNRAS, 465, 3416

Payne, D. J. B., & Melatos, A. 2006, ApJ, 641, 471

Peralta, C., Melatos, A., Giacobello, M., & Ooi, A. 2005, Astrophys. J., 635, 1224

Pons, J. A., & Geppert, U., 2007, A&A, 470, 303

Pons, J. A., & Geppert, U. 2010, A&A, 513, L12

Rea, N., & Esposito, P. 2011, Astrophys. Space Sci. Proc., 21, 247

Reisenegger, A. 2009, A&A, 499, 557

Shafranov, V. D. 1966, Rev. Plasma Phys., 2, 103

Sieniawska, M., & Bejger, M. 2019, Universe, 5, 217

Singh, N., Haskell, B., Mukherjee, D., & Bulik, T. 2020, MNRAS, 493, 3866

Sourie, A., & Chamel, N. 2020a, MNRAS, 493, 382

Sourie, A., & Chamel, N. 2020b, MNRAS, 493, L98

Sur, A., Haskell, B., & Kuhn, E. 2020, MNRAS, 495, 1360

Suvorov, A. G., Mastrano, A., & Geppert, U. 2016, MNRAS, 459, 3407

Thompson, C., & Duncan, R. C. 1995, MNRAS, 275, 255

Tolman, R. C. 1939, PhRv, 55, 364

Ushomirsky, G., Cutler, C., & Bildsten, L. 2000, MNRAS, 319, 902

Viganò, D., Pons, J. A., & Miralles, J. A. 2012, Comput. Phys. Commun., 183, 2042

Viganò, D., Rea, N., Pons, J. A., Perna, R., Aguilera, D. N., & Miralles, J. A. 2013, MNRAS, 434, 123

Woan, G., Pitkin, M. D., Haskell, B., Jones, D. I., & Lasky, P. D. 2018, ApJ, 863, L40

Author contributions statements

Title: "The impact of superconductivity and the Hall effect in models of magnetised neutron stars"

Authors: Ankan Sur and Brynmor Haskell

Publication: Publications of the Astronomical Society of Australia, Volume 38, article id. e043

Contributions:

Ankan Sur: Developed the numerical algorithm, performed all calculations, produced figures, and contributed to writing the manuscript. My total contribution to this article is 80%.

_____
Ankan Sur

Brynmor Haskell: developed ideas, supervised the project, and contributed to writing the paper. My contribution to this article is 20%.

_____
Brynmor Haskell

Gravitational waves from mountains in newly born millisecond magnetars

"The true sign of intelligence is not knowledge but imagination."

-Albert Einstein

Gravitational waves from mountains in newly born millisecond magnetars

Ankan Sur ⬤★ and Brynmor Haskell

Nicolaus Copernicus Astronomical Center, Polish Academy of Sciences, Bartycka 18, PL-00716 Warsaw, Poland

ABSTRACT

In this paper, we study the spin-evolution and gravitational-wave luminosity of a newly born millisecond magnetar, formed either after the collapse of a massive star or after the merger of two neutron stars. In both cases, we consider the effect of fallback accretion; and consider the evolution of the system due to the different torques acting on the star, namely the spin-up torque due to accretion and spin-down torques due to magnetic dipole radiation, neutrino emission, and gravitational-wave emission linked to the formation of a 'mountain' on the accretion poles. Initially, the spin period is mostly affected by the dipole radiation, but at later times, accretion spin the star up rapidly. We find that a magnetar formed after the collapse of a massive star can accrete up to $1\,M_\odot$, and survive on the order of 50 s before collapsing to a black hole. The gravitational-wave strain, for an object located at 1 Mpc, is $h_c \sim 10^{-23}$ at kHz frequencies, making this a potential target for next-generation ground-based detectors. A magnetar formed after a binary neutron star merger, on the other hand, accretes at the most $0.2\,M_\odot$ and emits gravitational waves with a lower maximum strain of the order of $h_c \sim 10^{-24}$, but also survives for much longer times, and may possibly be associated with the X-ray plateau observed in the light curve of a number of short gamma-ray burst.

Key words: gravitational waves – methods: analytical – methods: numerical – stars: magnetars – stars: neutron.

1 INTRODUCTION

Millisecond magnetars are suggested to be rapidly rotating neutron stars (NSs) with strong magnetic field strengths $B \geq 10^{15}$ G (Duncan & Thompson 1992; Thompson & Duncan 1993; Dai & Lu 1998). What leads to the formation of such magnetars is an open astrophysical question, but several channels have been proposed such as the mergers of binary NSs (BNSs; Giacomazzo & Perna 2013) or binary white dwarfs (Tauris et al. 2013; Schwab, Quataert & Bildsten 2015), core-collapse supernova associated with long gamma-ray bursts (LGRBs; Usov 1992; Wheeler et al. 2000; Bucciantini et al. 2008, 2009), and accretion-induced collapse of white dwarfs (WDs; Tauris et al. 2013). Although not yet 'seen' directly, there are hints from the X-ray plateau of gamma-ray bursts (GRBs) that the central engine could likely be a rapidly rotating magnetar (Rowlinson et al. 2010, 2013; Lasky et al. 2014, 2017; Sarin, Lasky & Ashton 2019). Moreover, millisecond magnetars could explain the possible physics behind the observed plateaux in X-ray light curves of short gamma-ray bursts (SGRBs; Strang & Melatos 2019). In all cases, the magnetar is born in an environment rich in matter, which facilitates accretion on to the star influencing its overall evolution. Such an object has a high rotational energy, which allows for the magnetar to be 'supramassive', i.e. to support a higher maximum mass than a non-rotating star. As the star spins down due to gravitational wave (GW) and electromagnetic torques, this reduces centrifugal support and, unless the total mass of the system is low enough for the NS to be stable, eventually leads to collapse to a black hole (BH), as is generally expected for most binary NS merger remnants (Ravi & Lasky 2014). However, in a matter-rich environment,

fallback accretion can play a leading role in the evolution of the system, as it provides a spin-up torque which increases centrifugal support, but ultimately, pushes the star closer to collapse to a BH by increasing its mass. This is particularly true if the magnetar is formed by the collapse of a massive star, in which case, a massive disc of up to $\approx 1\,M_\odot$ may be formed, leading to a hyperaccretion disc and powering part the emission observed in LGRBs (Mészáros 2006). A similar situation may occur after a binary merger, but the expelled mass that is subsequently re-accreted is expected to be lower and not exceed $\approx 0.2\,M_\odot$ (Bernuzzi 2020). In all cases, however, a transient source of GWs is expected; and it is essential to understand the early evolution of the system, and the impact of accretion, to determine the astrophysical relevance of these scenarios as targets for current and future GW detectors (Murase & Bartos 2019). There have also been strong evidence based on the distribution of collapse times of millisecond magnetars that they spin-down through GWs among other things (Sarin, Lasky & Ashton 2020).

After the first detection of GWs (Abbott et al. 2016), the increasing rate of observing events – compact binary coalescence including binary BHs, BHNS, or BNSs – by Advanced LIGO (aLIGO) and Advanced Virgo have opened new ways to look into the universe (Abbott et al. 2019a, 2020c,b). GWs from isolated systems such as pulsars, newly born magnetars or core-collapsed supernova still remain unobserved (Abbott et al. 2010, 2019d,b,e,f, 2020a) demanding better theoretical models and improved sensitivity of the detectors. The distinctive signature of the GW strain and the rate of such events carry invaluable information about the properties of NSs such as its mass and radius (Abbott et al. 2018).

A number of mechanisms have been proposed by which an isolated NS can emit GWs (Lasky 2015; Haskell et al. 2015a). First, all modes of oscillation can couple to the gravitational field, leading to GW emission. Following the birth of the star, the f-mode is the prime
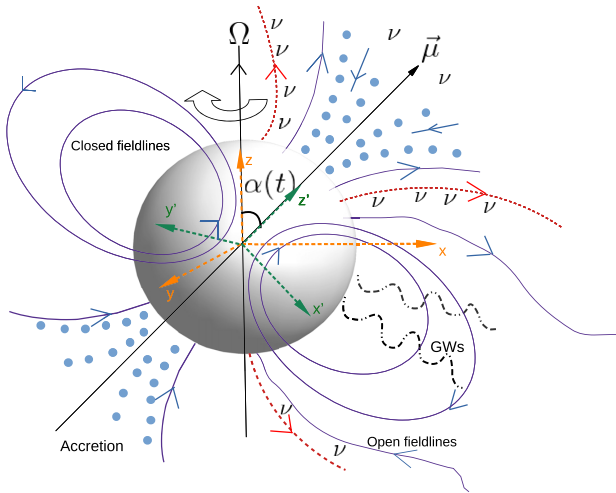
★ E-mail: ankansur@camk.edu.pl

Figure 1. Pictorial description of the millisecond magnetar. There are two coordinate systems, one having the rotation axis (Ω) and another having the magnetic moment ($\vec{\mu}$) axis. These axes are inclined at an angle $\alpha(t)$. The blue dots show matter falling on the two polar caps and forming two accreting columns. As the star rotates, it radiates energy in dipolar radiation and GWs. The red dotted lines represent the escaping neutrinos which carry away heat and angular momentum in the form of a wind.

candidate to be excited and emit observable GWs (Ciolfi et al. 2011), however, the r-mode oscillations in the NS core may be unstable if the star is born rapidly rotating, and contribute to its GW emission (Owen et al. 1998; Andersson & Kokkotas 2001; Bondarescu, Teukolsky & Wasserman 2007; Haskell, Andersson & Passamonti 2009; Alford & Schwenzer 2014; Haskell 2015).

Secondly, a strong toroidal magnetic field could deform the shape of the star to a prolate-spheroid (Cutler 2002) leading to unstable free precession and becoming an orthogonal rotator. Dall'Osso, Stella & Palomba (2018) have shown that such an object with a spin period $\simeq 2$ ms and an optimal ellipticity $\varepsilon \sim (1 - 5) \times 10^{-3}$ are potential candidates for aLIGO and future GW detectors. Additionally, in accreting NSs, the flow of matter on to the surface could lead to crustal asymmetries (Ushomirsky, Cutler & Bildsten 2000) and create so-called 'mountains' when matter gets submerged deep within the crust (Haskell et al. 2015b; Gittins, Andersson & Jones 2020; Singh et al. 2020). The flow of matter also compresses the magnetic field both globally and locally which gives rise to a sizable mountain (Payne & Melatos 2004; Melatos & Payne 2005).

In this paper, we consider a newly born magnetar (Fig. 1) rotating with millisecond period, formed in an environment where the matter around it could not reach its escape velocity and thus falls back. When the corotation radius exceeds the magnetospheric Alfvén radius, matter flows along the magnetic field lines and gives up angular momentum to the star. As the flow continues, two accreting columns are formed at the poles. In these regions, the freely falling material and the outflow reaches hydrostatic equilibrium (Basko & Sunyaev 1976) and neutrinos carry away heat and part of the gravitational binding energy. In these conditions, the accretion rate ($\dot{M}$) in high, leading to super-Eddington accretion and significant accumulation of matter at the base of the columns, allowing the star to possess a time-varying quadrupole and emit GWs (Piro & Thrane 2012; Zhong, Dai & Li 2019). In this paper, we study the spin evolution of the star, due to the different torques acting upon it, and calculate the characteristic GW strain.

We improve upon the static model proposed in Zhong et al. (2019) by considering time-varying quantities such as the accretion rate, spin period, magnetic field, and mass and radius, obtained from relativistic rotating stellar models, thus, making the model truly *dynamical*. We also consider an additional torque due to the neutrino-driven wind of charged particles and show that it doesn't significantly spin-down the star. To further simplify our model, we do not consider additional GW torques beyond those due to our 'mountain' (e.g. due to unstable modes or hydromagnetic instabilities as in Melatos & Priymak 2014) nor do we consider viscosity in the stellar interior, as we shall see that this would impact the evolution of the system on time-scales much longer than those of interest for our model. With all these considerations, we show that accretion causes the star to spin faster radiating energy in GWs detectable by future observatories.

This article is arranged as follows: we discuss the process of accretion leading to the formation of the massive NS and the mechanism by which it emits GW in Sections 2 and 3, respectively. In Section 4, we show our results for the spin evolution and GW strain for different initial conditions, while summary and conclusions are presented in Section 5.

2 ACCRETION

Two important radii that govern the flow of matter around a rotating NS are the magnetospheric Alfvén radius (r_m) and the corotation radius (r_c) defined as

$$r_m = \left(\frac{B^4 R^{12}}{GM\dot{M}^2} \right)^{1/7}, \quad r_c = \left(\frac{GM}{\Omega^2} \right)^{1/3}, \tag{1}$$

where R, M, and Ω are the radius, total mass, and angular frequency of the magnetar. When $r_m > r_c$, matter spins at super-Keplerian speed and co-rotates with the star. When $r_m < r_c$, the flow of matter gets channeled by the magnetic field lines and accreted on to the two polar caps of the NS, before spreading on the surface. We consider an early-type mass accretion rate $\dot{M} = 10^{-3} \eta t^{1/2}$ $M_\odot \text{s}^{-1}$ which is obtained from fits following numerical simulations of supernova fallback accretion (MacFadyen, Woosley & Heger 2001; Zhang & Dai 2008). Here, η is a constant that depends on the supernova explosion process. Although the uncertainties remain large and the exact scaling may be different than $t^{1/2}$, given the fact that the star accretes at a rate of $0.001 - 0.01 \, M_\odot \text{s}^{-1}$, this will not change significantly the survival time of the NS before collapsing to a BH. The total baryonic mass of the star as function of time (measured in seconds) is

$$M_b(t) = M_0 + \int_0^t \dot{M} \mathrm{d}t \tag{2}$$

$$= M_0 + \int_0^t \eta 10^{-3} t^{1/2} \mathrm{d}t \tag{3}$$

$$= M_0 + \frac{2}{3} \eta 10^{-3} t^{3/2}, \tag{4}$$

where M_0 is its initial mass. In practice, to study the accretion torques, we will need the gravitational mass, which we denote with M. To obtain this, we calculate, for each time-step, a relativistic rotating model for the star, using the code RNS (Stergioulas & Friedman 1995), and extract the gravitational mass, and moment of inertia of the star, as we shall describe in the following. As the magnetar gains mass (when $r_m < r_c$), its radius changes depending on the equation of state (EOS) of the NS. This requires detailed modelling of the accreted crust (Haensel, Potekhin & Yakovlev 2007; Haensel & Zdunik 2008; Gusakov & Chugunov 2020). Since we are interested in the approximate behaviour of how the radius changes with mass,
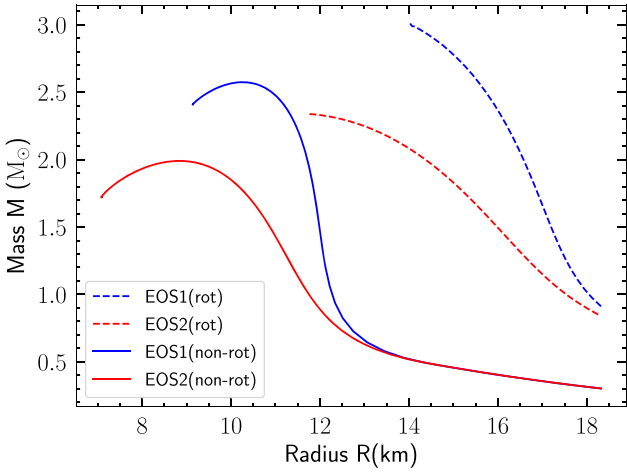
Figure 2. Mass-radius relation for our magnetar model using the two different EOS given in Table 1, i.e. blue solid line gives $M_{max} = 2.57\,M_\odot$ while the red solid line gives $M_{max} = 2.0\,M_\odot$. These refer to the non-rotating models and are obtained by solving the TOV equation. For a star rotating at Keplerian frequency, the gravitational mass and the equatorial radius are obtained with the RNS code, and plotted for the two different EOSs: higher maximum mass (blue dotted line) and the lower maximum mass (red dotted line).

Table 1. Summary of the parameters considered for the two different EOSs for a non-rotating NS.

Equation of state	γ_1	γ_2	$\rho_c (\mathrm{gm\,cm^{-3}})$	$M_{max}^{non-rot}(M_\odot)$
EOS1	1.663	3.4	4.5×10^{14}	2.57
EOS2	1.663	2.65	4.5×10^{14}	2.0

we adopt a simple EOS of the form

$$P(\rho) = \begin{cases} k\rho^{\gamma_1} & \text{if } \rho < \rho_c \\ k'\rho^{\gamma_2} & \text{if } \rho \geq \rho_c \end{cases}, \tag{5}$$

where $\gamma_1 = 1.663$ considering non-relativistic neutrons in the outer layers (leaving the inner layers unaffected), $\gamma_2 = 3.4$, and $\rho_c = 4.5 \times 10^{14}\,\mathrm{gm\,cm^{-3}}$. We fixed $k = 3^{2/3}\pi^{4/3}h^2/5m_n^{8/3}$, where m_n is the mass of a neutron while the constant k' was calculated imposing continuity of pressure at the critical density ρ_c. This particular EOS was adopted since it models the physics of the outer layers of the star, which are affected by the accretion and determine the change in radius, but allows us to obtain a $1.4\,M_\odot$ star with radius $R = 12$ km for the non-rotating model, is consistent with more realistic estimates obtained from micro-physically motivated equations of state (Haensel et al. 2007). The mass radius relation for this EoS, both in the case of a non-rotating star, obtained by solving the Tolman–Oppenheimer–Volkoff (TOV) equation, and for a model rotating at the Keplarian breakup frequency (obtained using RNS) are shown in Fig. 2. The maximum mass obtained for the non-rotating case is $2.57\,M_\odot$, interestingly close to the recent observation by LIGO of a possibly heavy NS (Abbott et al. 2020c). We assume that the star collapses to a BH when this mass limit is exceeded. Additionally, as can be seen in Fig. 2, we explored an EOS by using the same γ_1 and ρ_c but changing $\gamma_2 = 2.65$, yielding a maximum mass $M_{max} = 2\,M_\odot$, which is consistent with the maximum observed mass of an NS to date (Demorest et al. 2010; Cromartie et al. 2020). Table 1 shows the summary of the parameters and the maximum non-rotating mass for both the EOS considered in our analysis. The accretion column

forms when $r_m < r_c$, implying a critical accretion rate

$$\dot{M} > \dot{M}_{crit} = 1.8 \times 10^{-2} M_{1.4}^{-5/3} B_{15}^2 R_{12}^6 P_1^{-7/3} M_\odot\,s^{-1}, \tag{6}$$

showing a strong scaling with the radius and spin period of the star.

3 GRAVITATIONAL WAVES

Let us consider the magnetar to be a rigid-body rotating with an angular velocity Ω about the z-axis (see Fig. 1). The magnetic axis points along z' axis, inclined at an angle $\alpha(t)$ with respect to the rotation axis.

We can express the moment of inertia of a spherical star, as $I = \tilde{I}MR^2$, where the behaviour of $\tilde{I}$ depends on the EOS, but at least in slow rotation is generally a function of compactness (Lattimer & Schutz 2005; Breu & Rezzolla 2016).

As our star is not spherical, but deformed by the presence of the accretion mound, let us denote the moment of inertia along the coordinate axes (x', y', z') as I_1, I_2, and I_3. The system will not be exactly biaxial as the rotational bulge is associated with the x, y, z coordinate system, whereas the accretion mountain is associated with the x', y', z' coordinate system. Given the many other approximations of our analysis, we will however ignore this small effect and take $I_1 \sim I_2$. The GWs emitted by such an object have an amplitude

$$h_0 = \frac{4G}{c^2} \frac{(I_1 - I_3)\Omega^2 \sin^2\alpha}{d}, \tag{7}$$

where d is the distance to the source. If we imagine the accreted matter to be two cylindrical bodies with radius r at the poles, the moment of inertia along the x', z' axes follows as

$$I_1 = \tilde{I}MR^2 + 2M_{acc}R^2, \tag{8}$$

$$I_3 = \tilde{I}MR^2 + 2 \times \tfrac{1}{2}M_{acc}r^2, \tag{9}$$

where M_{acc} is the mass accreted at each pole. The difference in moment of inertia along the two directions can be approximated as

$$I_1 - I_3 = 2M_{acc}R^2 - 2 \times \tfrac{1}{2}M_{acc}r^2 \tag{10}$$

$$\approx 2M_{acc}R^2, \quad R \gg r. \tag{11}$$

Thus, the GW amplitude becomes

$$h_0 = \frac{8G}{c^2} \frac{M_{acc}R^2\Omega^2 \sin^2\alpha}{d} \tag{12}$$

and the characteristics GW strain is approximately given by (Corsi & Mészáros 2009)

$$h_c = fh_0\sqrt{\frac{dt_{sur}}{df}} \approx h_0\sqrt{ft_{sur}}, \tag{13}$$

where t_{sur} is the survival time-scale for the magnetar before its collapse, $f = \Omega/\pi$ is the dominant frequency at which GWs are emitted for $\alpha = 90°$. The body does not emit any GWs when α either becomes 0 or π radians. The GW luminosity in such a process goes as

$$L_{GW} = -\tfrac{2}{5}\frac{G}{c^5}(I_1 - I_3)^2\Omega^6\sin^2\alpha(16\sin^2\alpha + \cos^2\alpha) \tag{14}$$

$$= -\tfrac{8}{5}\frac{G}{c^5}M_{acc}^2 R^4\Omega^6\sin^2\alpha(16\sin^2\alpha + \cos^2\alpha). \tag{15}$$

4 SPIN AND INCLINATION

The spin evolution is affected by the torques acting due to accretion, the emission of GWs, the escaping neutrinos, and the dipolar

magnetic field radiation. The rate at which angular momentum is lost due to the GWs is

$$N_{\text{GW}} = \frac{L_{\text{GW}}}{\Omega}. \tag{16}$$

For the torque due to the external dipolar magnetic field, we use the expression deduced by Spitkovsky (2006) from numerical simulations of the magnetosphere in plasma

$$N_{\text{dip}} = \frac{B^2 R^6 \Omega^3}{c^3}(1 + \sin^2 \alpha). \tag{17}$$

The accretion torque acting on the magnetar is given by

$$N_{\text{acc}} = n(\omega)(GMr_m)^{1/2}\dot{M}, \tag{18}$$

where we adopt $n(\omega) = (1 - \omega)$ as considered by Piro & Ott (2011), Zhong et al. (2019). This torque can either be positive or negative depending on the fastness parameter $\omega = (r_m/r_c)^{3/2}$. The star enters the so-called 'propeller phase' for $n(\omega) < 0$ where it experiences a negative torque and spins down by expelling matter from the super-Keplerian magnetosphere. In fact, Ekşi, Hernquist & Narayan (2005) showed that in most cases of fallback accretion, the disc will pass through this propeller phase and such systems could appear as Ultra-Luminous X-ray Sources when the disc is fed by supercritical mass accretion rates (Erkut, Ekşi & Alpar 2019). For a detailed discussion, see Zhang & Dai (2008), Piro & Ott (2011), and Dai & Liu (2012).

The neutrino-driven wind is expected to interact with the strong magnetic field of the star, leading to co-rotation of charged particles in the magnetosphere and a loss of angular momentum (Thompson, Chang & Quataert 2004). This emission, in fact, follows the open magnetic field lines and is thus not isotropic. The luminosity and the energy of neutrinos in this process are given by (Lander & Jones 2020)

$$\frac{L_\nu(t)}{10^{52}\,\text{erg s}^{-1}} = 0.7 \exp\left(-\frac{t}{1.5\text{s}}\right) + 0.3\left(1 - \frac{t}{50\text{s}}\right)^4, \tag{19}$$

$$\frac{E_\nu(t)}{10\,\text{MeV}} = 0.3 \exp\left(-\frac{t}{4\text{s}}\right) + \left(1 - \frac{t}{60\text{s}}\right). \tag{20}$$

These fits have been obtained from the simulations by Pons et al. (1999), Metzger et al. (2011), and are valid upto 40 s. Although these expressions are valid for slow-rotation, Lander & Jones (2020) makes improvements by considering centrifugal enhancement for which we use the limiting values. Based on our reference model, with the uncertainties, we may expect different behaviour due to also different temperatures in the cases of core-collapsed supernovae and BNS post-mergers. But given that we confirm this torque is generally negligible for our problem, we do not investigate the effect of temperature further. The mass-loss rate due to the neutrinos is given by

$$\dot{M}_\nu = 6.8 \times 10^{-5}\,\text{M}_\odot\text{s}^{-1}\left(\frac{L_\nu}{10^{52}\,\text{erg s}^{-1}}\right)^{5/3}\left(\frac{E_\nu}{10\,\text{MeV}}\right)^{10/3}. \tag{21}$$

The rate of change of electromagnetic energy carried away by the neutrinos is given by (Lander & Jones 2020)

$$\dot{E}_{\text{EM}} = \begin{cases} c^2\dot{M}_\nu\sigma_0^{2/3} & \text{if } \sigma_0 < 1 \\ \frac{2}{3}c^2\dot{M}_\nu\sigma_0 & \text{if } \sigma_0 \geq 1 \end{cases}, \tag{22}$$

where σ_0 is called the wind magnetization parameter (Metzger et al. 2011) given by

$$\sigma_0 = \frac{B^2 R^4 \Omega^2}{\dot{M}_\nu c^3}, \tag{23}$$

that accounts for asymptotic partition between the kinetic and magnetic energy in the wind. Further, $\sigma_0 \leq 1$ implies a non-relativistic

wind as compared to $\sigma_0 > 1$ for a relativistic wind (Metzger et al. 2011). Neglecting the small change in moment of inertia of the star due to neutrino mass-loss, the spin evolution purely due to the loss of neutrinos is given by

$$\frac{d\Omega}{dt} = -\frac{\dot{E}_{\text{EM}}}{I\Omega} = -\frac{L_\nu}{I\Omega}. \tag{24}$$

Thus, the exact scaling with which Ω varies with time is proportional to $\Omega^{1/3}$ for $\sigma_0 < 1$ while Ω for $\sigma_0 > 1$. As in past studies, which have suggested that neutrinos are inefficient in spinning down a protoneutron star (Baumgarte & Shapiro 1998), we find that magnetic dipole radiation is a dominant effect as found by Lasky et al. (2017) leading to a braking index of $n = 3$ obtained from fits of X-ray plateaus in SGRBs, although it's precise observational determination remains challenging (Melatos 1997; Archibald et al. 2016).

The net rate of change of angular momentum due to the different torques acting on our star is

$$\frac{d}{dt}(I_3\Omega) = -N_{\text{GW}} - N_{\text{dip}} - N_\nu + N_{\text{acc}} = N^{\text{net}}, \tag{25}$$

$I_3 \approx \tilde{I}MR^2$ (neglecting the contribution from the cylindrical column of matter). We drop the notation I_3 and simply represent it as I. This gives us an evolution equation for the spin

$$\frac{d\Omega}{dt} = (-N_{\text{GW}} - N_{\text{dip}} - N_\nu + N_{\text{acc}})/I - \frac{\Omega}{I}\frac{dI}{dt} \tag{26}$$

and

$$\frac{1}{I}\frac{dI}{dt} = \frac{\dot{M}}{M} + 2\frac{\dot{R}}{R} + \frac{\dot{\tilde{I}}}{\tilde{I}}, \tag{27}$$

where $\dot{M} = \dot{M}_{acc} - \dot{M}_\nu$ and the dot represents derivative with respect to time. The mass-loss due to neutrinos allows us to calculate the evolution of inclination angle (for a more sophisticated treatment including the effect of internal dissipation due to viscosity, see Lander & Jones 2020) as follows

$$\frac{d\alpha}{dt} = \frac{\dot{E}_{\text{EM}}\sin\alpha\cos\alpha}{I\Omega^2}. \tag{28}$$

Viscosity plays an important role in affecting the inclination angle of NSs (Jones 1976; Dall'Osso & Perna 2017). The compelling effects due to viscous dissipation and external torques tend to make the magnetic axis orthogonal to the rotational axis soon after birth which gradually starts aligning over hundreds of years (Lander & Jones 2020). Since we are interested in shorter time-scales during which the star survives, we ignore the evolution of $\alpha(t)$ due to bulk viscosity and dissipation from the internal fluid motions.

5 RESULTS

5.1 Core-collapsed supernovae (CCSNe)

We present our results after the birth of the magnetar with EOS1. The value of η plays an important role in the lifetime before the magnetar collapses to a BH. Simulation shows that typical values of η lie between $0.1 - 10$ (Piro & Ott 2011). A lower η implies a more powerful supernova explosion and varying this for the magnetar, we expect a change in t_{sur}, the rate at which it gains mass and the duration of the GW signal. However, this should not affect the overall shape of the waveform.

We chose $\eta = 10$ making the magnetar (with $M_0 = 1.4\,\text{M}_\odot$ and $P_0 = 1.1$ ms) to survive a total of $t_{\text{sur}} \sim 49$ s. The choice of these parameters has several implications, first being the time at which accretion columns are formed as one requires $\dot{M} > \dot{M}_{\text{cric}}$ (Zhong et al. 2019). This condition is achieved at a threshold time $t_{\text{th}} \sim 2.0$ s.

Second, $n(\omega) < 0$ for $t < t_{\text{th}}$ and the star experiences a negative torque. Third, there are no GWs emitted during this phase. The spin evolution is only affected by the dipolar radiation, angular momentum loss due to neutrinos and the co-rotating matter. After $t > t_{\text{th}}$, two accretion columns are formed, the star experiences a positive torque and the GWs carry away angular momentum. Since it is easier for us to work in normalized units, we express different quantities of the star such as mass, radius, magnetic field, and the mass accretion rate as

$$R_{15} = \frac{R}{15\,\text{km}}, \; M_{1.4} = \frac{M}{1.4 M_\odot}, \; B_{15} = \frac{B}{10^{15} G}, \; \dot{M}_{-2} = \frac{\dot{M}}{10^{-2} M_\odot \text{s}^{-1}}. \tag{29}$$

We further work with spin period ($P = 2\pi/\Omega$) which is normalized as $P_1 = P/1\,\text{ms}$. To calculate the amount of column mass that is accreted on to the poles, we use the relation obtained by Zhong et al. (2019)

$$M_{\text{acc}} = 1.7 \times 10^{-7} M_\odot M_{1.4}^{-25/56} \dot{M}_2^{3/28} B_{15}^{-5/7} R_{15}^{125/56}. \tag{30}$$

This estimate is model dependent, however different estimates, e.g. considering magnetically confined matter (Brown & Bildsten 1998; Singh et al. 2020), produce similar estimates for the mass. The scalings with the different parameters (i.e. $M_{1.4}$, $\dot{M}_{-2}$, B_{15}, etc.) will be different and may affect our model. However, the strongest driver of the evolution is the scaling of the GW torque with spin period, which will remain unaffected, as will the electromagnetic torques. We, thus, do not expect these uncertainties to affect our qualitative conclusions. We assume that the accretion column reduces the magnetic dipole moment as $|\mu| = |\mu_i|(1 - M_{\text{acc}}/M_c)$, with $M_c = 1.2 \times 10^{-6} M_\odot \text{s}^{-1}$ (Payne & Melatos 2004). This makes the magnetic field strength to vary as

$$B_{15} = B_{15,i} \frac{R_{15,i}^3}{R_{15}^3} \left(1 - \frac{M_{\text{acc}}}{M_c}\right), \tag{31}$$

where i denote the initial value of each quantity. The accreted material drags the magnetic field lines by flux freezing as it moves from the polar caps towards the equator. A detailed calculation of the magnetic field structure and density of the mountain requires us to solve the Grad–Shafranov equation for magnetic equilibria, which is beyond the scope of this paper, but is outlined in the work by Melatos & Priymak (2014). The field burial further facilitates the formation of BHs by shutting the propeller effect and allowing fallback accretion. The evolution of inclination angle can be calculated using equation (22). Fig. 3 shows that for any random initial choice of α, the magnetic axis always becomes perpendicular to the rotation axis in about 10 ms. The kinks present at early times are an artefact of grid resoluton. We choose the initial value of $\alpha = 5°.7$ and our evolution at later stages is independent of this choice. By the time GWs are emitted, α becomes 90° and emission reaches its peak value. However, it is expected that in the first day of the magnetar, the inclination angle decreases rapidly making the rotation and magnetic axis aligned to each other (Şaşmaz Muş et al. 2019; Çıkıntoğlu, Şaşmaz Muş & Ekşi 2020). Using the definitions in equation (29), we find expression for the GW luminosity

$$L_{\text{gw}} = 1.1 \times 10^{42} \text{erg s}^{-1} M_{1.4}^{-25/28} \dot{M}_2^{3/14} B_{15}^{-10/7} R_{15}^{237/28} P_1^{-6}, \tag{32}$$

which changes with time as the magnetar's spin evolves due to the various processes. We calculate the evolution of the system accretes and calculate sequences of fixed baryon mass models with RNS, to obtain at each time-step the gravitational mass, radius and moment of inertia of the star. We investigate a range of models with initial spin period above the Keplerian breakup period corresponding to the initial mass, which we calculate with the RNS code, and take as our
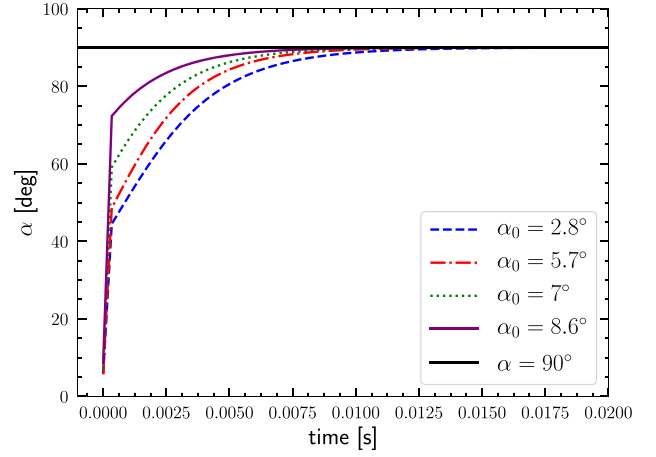

Figure 3. Evolution of the inclination angle $\alpha(t)$ for the magnetar formed after CCSNe for initial values $\alpha_0 \in (2°.8, 5°.7, 7°.0, 8°.6)$. The black solid line denotes $\alpha = 90°$. Given any initial choice, $\alpha \to 90°$ in $t \leq 10$ ms.
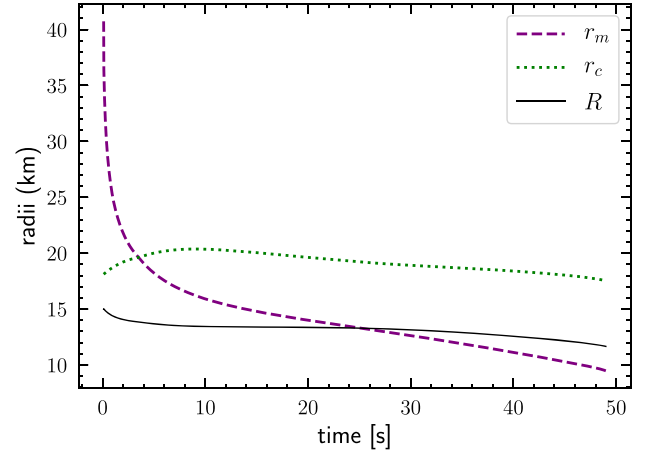

Figure 4. The location of magnetospheric radius (r_m), corotation radius (r_c), and the radius of the star (R) as a function of time for the magnetar formed after CCSNe with initial mass $M_0 = 1.4\,M_\odot$ and $P_0 = 1.1$ ms. When r_m becomes less than R, we set $r_m = R$ in our simulation.

reference model a magnetar with initial spin period $P_0 = 1.1$ ms, as in Ott et al. (2006).

Fig. 5 shows the evolution of spin due to the various torques. We see that the magnetic dipole radiation carry away most of the angular momentum as compared to the neutrino wind and GWs, which results in an initial increase in the spin period. After $t > t_{\text{th}}$, the torque on the star due to accretion is positive and dominates over other processes. At this stage, the condition $r_c > r_m$ also remains true. However, when r_m becomes less than the radius of the star, we set $r_m = R$. The evolution of these various radii is shown in Fig. 4, while in Fig. 5, we plot the contributions of the different torques to the spin evolution of the star. Similar results are also presented in Melatos & Priymak (2014) where the evolution of angular frequency versus time is calculated for accretion mountain with and without GWs due to hydromagnetic instabilities. In Fig. 6, we show the GW luminosity and the characteristic strain for two different choices P_0. There is an initial decrease in both quantities, which then gradually start increasing with time. Moreover, a higher initial spin simply makes the star to emit GWs at a lower luminosity
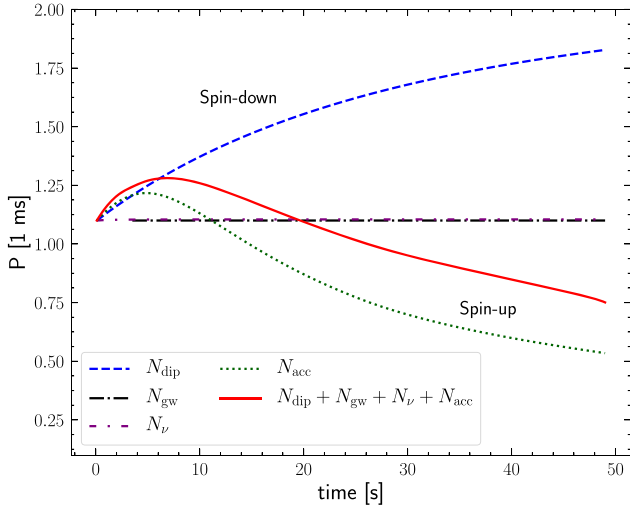
Figure 5. The spin evolution of the magnetar formed after CCSNe due to the various individual torques and the overall behaviour represented by solid red line. The period initially increases and then starts decreasing with time as accretion wins over the combined effects of neutrino luminosity, dipolar radiation, and the GW luminosity. At the end, the star collapses to a BH.
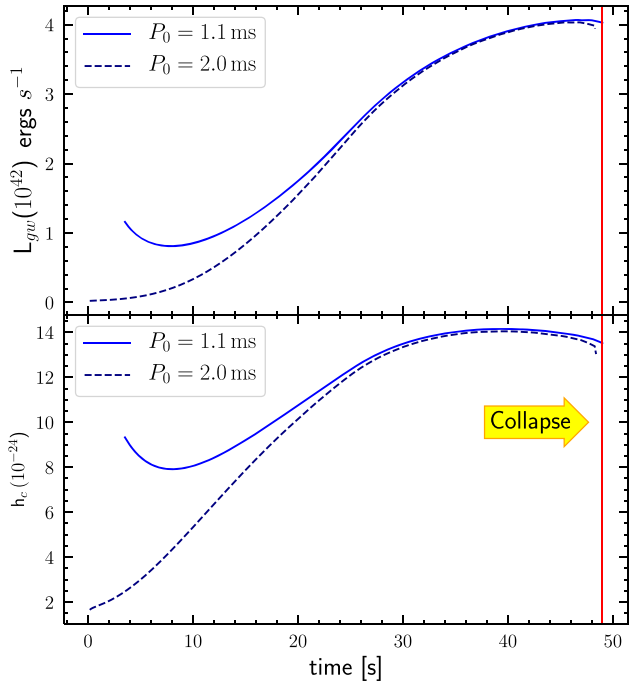

Figure 6. The GW luminosity (top panel) and characteristic GW strain (bottom panel) as a function of time for two different initial spin periods of the magnetar formed from CCSNe. The red line shows the time at which the magnetar collapses to a BH and the GW signal truncates.

before the collapse. Note that this behaviour is obtained considering that the spin period and frequency are time-dependent unlike the results given in Zhong et al. (2019) which shows a rise in h_c and L_{gw} till 4.3 s and a fall afterwards with time. We stress that our model includes a fully relativistic rotating stellar model and full time evolution of the system's parameters. Our model is, thus, more realistic and accurately represents the GW signal expected from this source, shown by the black line at around $\sim 10^3$ Hz in Fig. 7. On
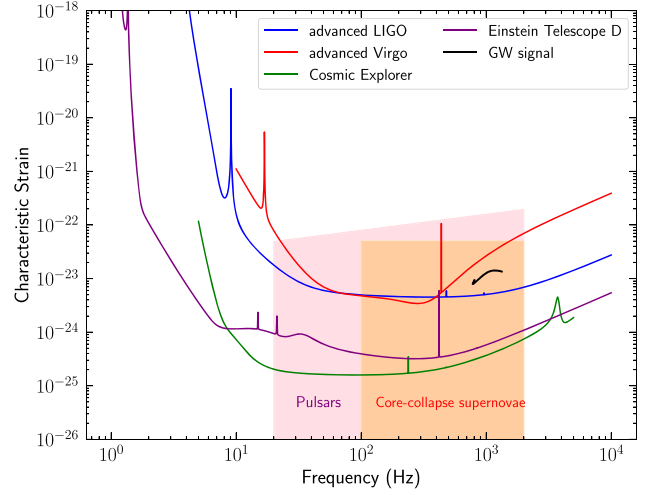

Figure 7. Design sensitivities for the second and third generation GW detectors to the characteristic strain. The purple, green, blue, and the red lines represent the Einstein Telescope, Cosmic Explorer, advanced LIGO, and advanced Virgo, respectively. The black line represent our GW signal from the magnetar before its collapse to a BH. Also shown are populations of pulsars (pink) and core-collapse supernovae (orange) with their spin frequencies.
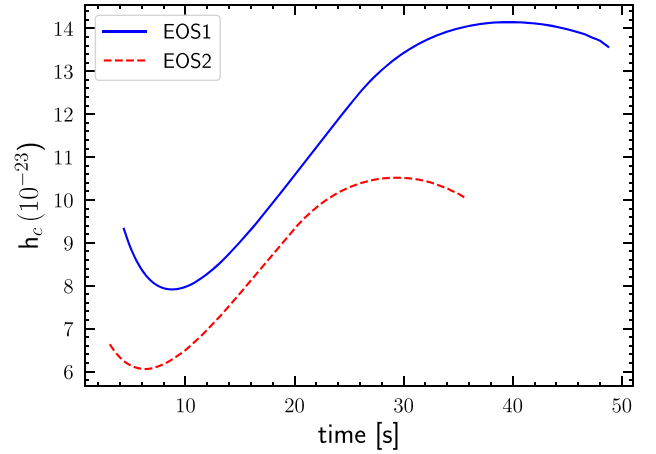
Figure 8. Characteristic GW strain for the two different equation of states (EOSs) in the case of CCSNe magnetar. Qualitatively, the behaviour is same apart from the total duration of the signal and its peak value.

performing the same analysis for a NS with $M_{max} = 2\,M_\odot$, we find a survival time of 35 s and no qualitative change in our results, see for example the behaviour of the GW strain in Fig. 8. Furthermore, we have varied the initial mass of the NS from $1.25 - 1.8\,M_\odot$. From Fig. 9, we can see that lowering the mass produces a higher peak of h_c and a longer signal.

5.2 Remnant of BNS mergers

We have assumed so far that following the collapse of the progenitor, there is enough mass available for accretion which increases the total mass until the magnetar collapses to a BH. Let us now look into a scenario in which the magnetar is created in a binary NS merger, and the mass available for accretion, e.g. remnant mass ejected in the merger, is only $0.2\,M_\odot$ (Radice et al. 2018; Bernuzzi 2020; Bernuzzi et al. 2020; Radice, Bernuzzi & Perego 2020). Although

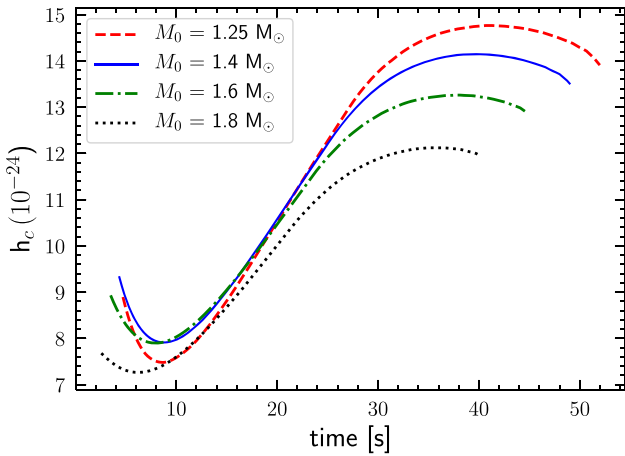**Figure 9.** Characteristic strain for different remnant masses of the magnetar (formed from CCSNe), $M_0 = (1.25, 1, 4, 1.6, 1.8)\,\mathrm{M_\odot}$. A lower mass progenitor emits GW strain at a higher strength before its collapse and has longer duration signal.
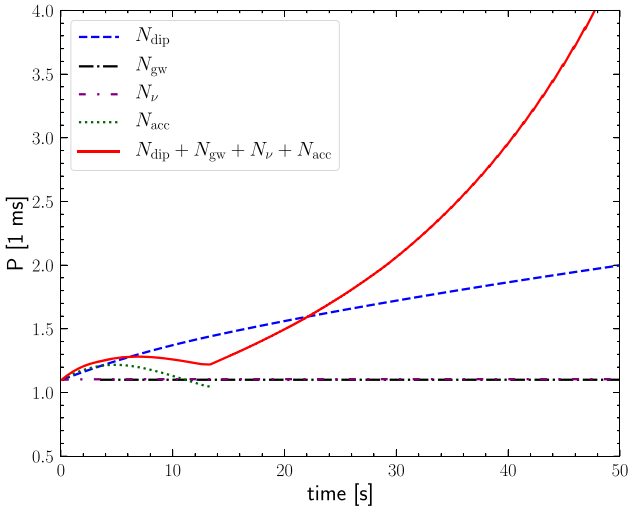

Figure 10. Spin evolution of the magnetar formed after the merger of a BNS (for a model with $\eta = 10$) when the total mass available for accretion is $0.2\,\mathrm{M_\odot}$. The different lines represent the spin due to the various individual torques while the red solid line shows the overall effect on the spin. The accretion torque stops at 14 s when the star starts to spin-down due to angular momentum carried away by the neutrino-wind, magnetic dipole radiation, and emission of GWs.

our mass accretion rate $\dot{M} = 10^{-3}\eta t^{1/2}\,\mathrm{M_\odot s^{-1}}$ refers to supernova disc accretion, none the less, we assume this form for BNS mergers, despite tidal tails formed in a post-merger remnant will accrete back on to the star at a different rate than that through relatively long-term disc accretion. Since in this case, the mass available for accretion is lower compared to the the supernovae disc-accretion, the evolution is different because the accretion stops soon after the entire mass is accreted and the magnetar spins down. The rate of accretion, in principle, is also not known,[1] which allows us to make a study by varying the parameter η to explore a range of values in $\dot{M}$ (Ruiz & Shapiro 2017). The spin evolution for $\eta = 10$ is shown in Fig. 10.

---

[1]In private communication with Dr. Tim Dietrich.

Initially, the star loses angular momentum through the neutrino wind and magnetic dipolar radiation until 7 s after which the accretion torque makes it spin faster. In about 14 s, the total mass in the disc gets accreted and the torque due to accretion becomes zero. At this point, there is no positive torque on the magnetar and the star continues to spin-down. The GW torque is weak compared to the other torques and hence, does not influence the overall spin-period, nevertheless, the emission is expected to continue, as the mountain is likely to be stable on the dynamical time-scales we are studying here, although it is likely to be disrupted on longer time-scales as the buried magnetic field re-emerges (Vigelius & Melatos 2009a,b). We show results upto 50 s, although the star survives for longer period of time. The evolution of the spin and GW signal are also shown in Figs 11(a) and (b), respectively for $\eta = 10$ (dashed line) and compared with two other values, $\eta = 5$ (dash–dotted line) and $\eta = 1$ (solid line). We conclude that the spin is mostly dominated by the dipole radiation and the duration of accretion is prolonged on lowering η as expected, while GW strain decreases when lowering η. The shape of the signal can be understood by how the star spins, as an increase in the spin period (decrease in frequency) causes the GW strain to decrease and vice-versa. This signal also remains weaker when compared to the previous case of core-collapsed supernova in which the magnetar spins-up due to accretion.

Although we have assumed an upper limit of the mass available for accretion by a remnant of BNS merger, it is possible that the mass available is few orders of magnitude lower (i.e. $0.001 - 0.01\,\mathrm{M_\odot}$). In this case, assuming the same $\dot{M}$, the magnetar would survive longer until its spin frequency decreases significantly due to dipole radiation and it cannot hold upto its own mass before collapsing to a BH.

6 SUMMARY AND CONCLUSIONS

In this paper, we have studied the evolution and GW emission of a newly born millisecond magnetar having a high-accretion rate of $\mathcal{O}(10^{-2})\mathrm{M_\odot s^{-1}}$ due to fall back accretion. We assume that accreted matter is confined at the poles and creates a 'mountain' that leads to a time varying quadrupole and GW emission (Zhong et al. 2019). If the magnetar is formed due to the collapse of a massive star, depending on its initial mass and rotation rate, survives for a time-scale of order $t \approx 50$ s before collapsing to a BH. If, on the other hand, it is formed after the merger of a binary NS system, the magnetar will survive much longer (although as it spins down, it can eventually collapse to a BH; Ravi & Lasky 2014), but its GW emission will be weaker.

The magnetar experiences different torques shortly after birth. In particular, we include for the first time the angular momentum carried away by magnetic dipole radiation and find it to be the main spin-down mechanism at early times, while neutrino-wind and GWs do not affect the spin period significantly, in comparison. We also include the effect of magnetic field burial and of the evolution of the inclination angle between the field and rotation axis. We find also that the magnetic moment axis becomes orthogonal to the rotation axis immediately after the star is born. Generally, a long-lived surviving magnetar is expected to have a very small inclination angle (Lander & Jones 2020). Note however that this can be due to secular evolution of the inclination angle on much longer time-scales and the millisecond magnetars that we examine in this paper are unlikely to be the progenitors of the galactic magnetars, as in most cases our systems collapse to a BH. Finally, we use precises relativistic and rapidly rotating models of the magnetar, obtained with the numerical code RNS (Stergioulas & Friedman 1995) to calculate the evolution of the
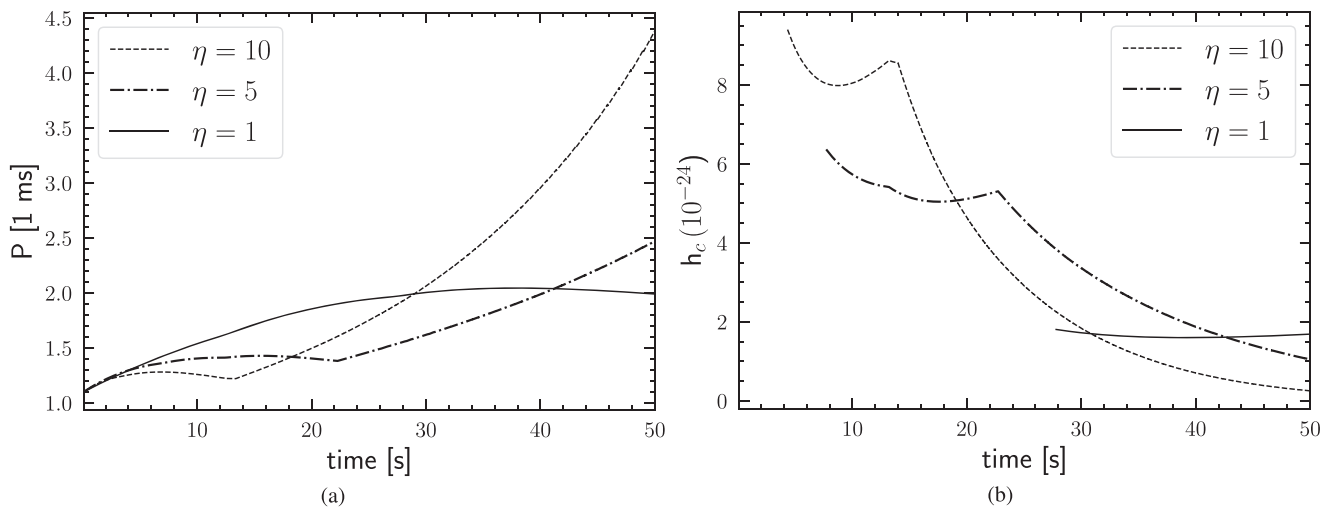
Figure 11. (a) Spin evolution and (b) GW strains for three different values of η for our fiducial magnetar model, formed as a remnant of BNS merger, when the total mass available for accretion is $0.2\,M_\odot$. The initial spin-period is $P_0 = 1.1$ ms. We show results upto 50 s when the magnetar survives and not yet collapsed to a BH.

gravitational mass, radius and moment of inertia of the star as it accretes matter from the surrounding disc.

Overall, we find that if the magnetar is formed after the collapse of a massive star, there is enough mass in the torus that the accretion torque dominates, spinning up the star. As matter is accreted, the GW strain increases with time (mainly due to the increasing frequency of the star), until the star exceeds the maximum mass for its EoS and collapses to a BH. We expect a 'burst' signal with an estimated GW strain $h_c \sim 10^{-24}$–10^{-23} for objects at a distance of 1 Mpc, making them potential targets for the third-generation detectors such as the Einstein Telescope and the Cosmic Explorer, although they may be detected by Advanced LIGO and Virgo at design sensitivity should they occur at a distance of a few hundred *kpc* (Abbott et al. 2019c). Sensitivity curves to the characteristic strain for these detectors are shown in Fig. 7. We have further investigated the scenario in which the magnetar is formed as the remnant of a BNS merger. In this case, the mass available for accretion is likely to not exceed $0.2\,M_\odot$ (Bernuzzi 2020). We have shown that, in this case, the combined effects of different processes slows down the spin period also causing the GW strain to decrease with time. In this case, the star does not collapse immediately and is likely to survive for 10^2–10^3 s before it collapses to a BH, if its initial mass exceeds the maximum mass for a non-rotating star (Ravi & Lasky 2014), leading to a signal that may be visible after the merger by next-generation detectors (Abbott et al. 2017). Sarin et al. (2018) also derived waveform model for millisecond magnetars and showed that the X-ray afterglow can be used to improve search sensitivity by up to 50 per cent and derived horizon distances. The birth-rate of millisecond magnetars associated with superluminous supernovae is $40\,\text{Gpc}^{-3}\text{yr}^{-1}$ while those with LGRBs is $140\,\text{Gpc}^{-3}\text{yr}^{-1}$ (Nicholl et al. 2017). BNS merger rates lie between $110 - 3840\,\text{Gpc}^{-3}\text{yr}^{-1}$ (Abbott et al. 2019a). An estimate that 10 per cent of BNS mergers give birth to millisecond magnetars and the given uncertainties in the formation channels, an average rate of $10 - 100\,\text{Gpc}^{-3}\text{yr}^{-1}$ was reported by Nicholl et al. (2017). Considering a volume of 1Mpc^{-3}, the event rate for this type of GW radiation is less compared to binary NS or binary BH mergers. Finally, we reiterate that the results presented in this paper are model-dependent and carry with them many uncertainties. More work is, thus, needed to explore the different model assumptions that drive the evolution of the system and produce more robust numerical results.

DATA AVAILABILITY

The data underlying this article will be shared on reasonable request to the corresponding author.

REFERENCES

Abbott B. et al., 2010, ApJ, 713, 671
Abbott B. et al., 2016, Phys. Rev. Lett., 116, 061102
Abbott B. et al., 2018, Phys. Rev. Lett., 121, 161101
Abbott B. et al., 2019a, Phys. Rev. X, 9, 031040
Abbott B. et al., 2019b, Phys. Rev. D, 99, 104033
Abbott B. et al., 2019d, Phys. Rev. D, 100, 024004
Abbott B. et al., 2019e, Phys. Rev. D, 100, 024017
Abbott B. et al., 2019f, ApJ, 886, 75
Abbott B. et al., 2020b, ApJ, 892, L3
Abbott R. et al., 2020c, ApJ, 896, L44
Abbott B. P. et al., 2017, ApJ, 851, L16
Abbott B. P. et al., 2019c, Phys. Rev. D, 99, 104033
Abbott B. P. et al., 2020a, Class. Quant. Grav., 37, 055002
Alford M. G., Schwenzer K., 2014, ApJ, 781, 26
Andersson N., Kokkotas K. D., 2001, Int. J. Mod. Phys. D, 10, 381
Archibald R. F. et al., 2016, ApJ, 819, L16
Basko M. M., Sunyaev R. A., 1976, MNRAS, 175, 395
Baumgarte T. W., Shapiro S. L., 1998, ApJ, 504, 431
Bernuzzi S. et al., 2020, MNRAS, 497, 1488

Bernuzzi S., 2020, Gen. Relativ. Gravit., 52, 40

Bondarescu R., Teukolsky S. A., Wasserman I., 2007, Phys. Rev. D, 76, 064019

Breu C., Rezzolla L., 2016, MNRAS, 459, 646

Brown E. F., Bildsten L., 1998, ApJ, 496, 915

Bucciantini N., Quataert E., Arons J., Metzger B. D., Thompson T. A., 2008, MNRAS, 383, L25

Bucciantini N., Quataert E., Metzger B. D., Thompson T. A., Arons J., Del Zanna L., 2009, MNRAS, 396, 2038

Çıkıntoğlu S., Şaşmaz Muş S., Ekşi K. Y., 2020, MNRAS, 496, 2183

Ciolfi R., Lander S. K., Manca G. M., Rezzolla L., 2011, ApJ, 736, L6

Corsi A., Mészáros P., 2009, ApJ, 702, 1171

Cromartie H. T. et al., 2020, Nature Astron., 4, 72

Cutler C., 2002, Phys. Rev. D, 66, 084025

Dai Z. G., Liu R.-Y., 2012, ApJ, 759, 58

Dai Z. G., Lu T., 1998, Phys. Rev. Lett., 81, 4301

Dall'Osso S., Perna R., 2017, MNRAS, 472, 2142

Dall'Osso S., Stella L., Palomba C., 2018, MNRAS, 480, 1353

Demorest P. B., Pennucci T., Ransom S. M., Roberts M. S. E., Hessels J. W. T., 2010, Nature, 467, 1081

Duncan R. C., Thompson C., 1992, ApJ, 392, L9

Ekşi K. Y., Hernquist L., Narayan R., 2005, ApJ, 623, L41

Erkut M. H., Ekşi K. Y., Alpar M. A., 2019, ApJ, 873, 105

Giacomazzo B., Perna R., 2013, ApJ, 771, L26

Gittins F., Andersson N., Jones D. I., 2020, MNRAS, 500, 13

Gusakov M. E., Chugunov A. I., 2020, Phys. Rev. Lett., 124, 191101

Haensel P., Zdunik J. L., 2008, A&A, 480, 459

Haensel P., Potekhin A. Y., Yakovlev D. G., 2007, Neutron Stars 1: Equation of State and Structure. Springer, New York

Haskell B. et al., 2015a, Gravitational Waves from Rapidly Rotating Neutron Stars. Springer, Switzerland, p. 85

Haskell B., 2015, Int. J. Mod. Phys. E, 24, 1541007

Haskell B., Andersson N., Passamonti A., 2009, MNRAS, 397, 1464

Haskell B., Priymak M., Patruno A., Oppenoorth M., Melatos A., Lasky P. D., 2015b, MNRAS, 450, 2393

Jones P. B., 1976, Ap&SS, 45, 369

Lander S. K., Jones D. I., 2020, MNRAS, 494, 4838

Lasky P. D., 2015, Publ. Astron. Soc. Austral., 32, e034

Lasky P. D., Haskell B., Ravi V., Howell E. J., Coward D. M., 2014, Phys. Rev. D, 89, 047302

Lasky P. D., Leris C., Rowlinson A., Glampedakis K., 2017, ApJ, 843, L1

Lattimer J. M., Schutz B. F., 2005, ApJ, 629, 979

MacFadyen A. I., Woosley S. E., Heger A., 2001, ApJ, 550, 410

Melatos A., 1997, MNRAS, 288, 1049

Melatos A., Payne D. J. B., 2005, ApJ, 623, 1044

Melatos A., Priymak M., 2014, ApJ, 794, 170

Mészáros P., 2006, Rep. Prog. Phys., 69, 2259

Metzger B. D., Giannios D., Thompson T. A., Bucciantini N., Quataert E., 2011, MNRAS, 413, 2031

Murase K., Bartos I., 2019, Ann. Rev. Nucl. Part. Sci., 69, 477

Nicholl M., Williams P. K. G., Berger E., Villar V. A., Alexander K. D., Eftekhari T., Metzger B. D., 2017, ApJ, 843, 84

Ott C. D., Burrows A., Thompson T. A., Livne E., Walder R., 2006, ApJS, 164, 130

Owen B. J., Lindblom L., Cutler C., Schutz B. F., Vecchio A., Andersson N., 1998, Phys. Rev. D, 58, 084020

Payne D. J. B., Melatos A., 2004, MNRAS, 351, 569

Piro A. L., Ott C. D., 2011, ApJ, 736, 108

Piro A. L., Thrane E., 2012, ApJ, 761, 63

Pons J. A., Reddy S., Prakash M., Lattimer J. M., Miralles J. A., 1999, ApJ, 513, 780

Radice D., Perego A., Hotokezaka K., Fromm S. A., Bernuzzi S., Roberts L. F., 2018, ApJ, 869, 130

Radice D., Bernuzzi S., Perego A., 2020, Ann. Rev. Nucl. Part. Sci., 70, 95

Ravi V., Lasky P. D., 2014, MNRAS, 441, 2433

Rowlinson A. et al., 2010, MNRAS, 409, 531

Rowlinson A., O'Brien P. T., Metzger B. D., Tanvir N. R., Levan A. J., 2013, MNRAS, 430, 1061

Ruiz M., Shapiro S. L., 2017, Phys. Rev. D, 96, 084063

Sarin N., Lasky P. D., Sammut L., Ashton G., 2018, Phys. Rev. D, 98, 043011

Sarin N., Lasky P. D., Ashton G., 2019, ApJ, 872, 114

Sarin N., Lasky P. D., Ashton G., 2020, Phys. Rev. D, 101, 063021

Schwab J., Quataert E., Bildsten L., 2015, MNRAS, 453, 1910

Şaşmaz Muş S., Çıkıntoğlu S., Aygün U., Andaç I. C., Ekşi K. Y., 2019, ApJ, 886, 5

Singh N., Haskell B., Mukherjee D., Bulik T., 2020, MNRAS, 493, 3866

Spitkovsky A., 2006, ApJ, 648, L51

Stergioulas N., Friedman J. L., 1995, ApJ, 444, 306

Strang L. C., Melatos A., 2019, MNRAS, 487, 5010

Tauris T. M., Sanyal D., Yoon S. C., Langer N., 2013, A&A, 558, A39

Thompson C., Duncan R. C., 1993, ApJ, 408, 194

Thompson T. A., Chang P., Quataert E., 2004, ApJ, 611, 380

Ushomirsky G., Cutler C., Bildsten L., 2000, MNRAS, 319, 902

Usov V. V., 1992, Nature, 357, 472

Vigelius M., Melatos A., 2009a, MNRAS, 395, 1972

Vigelius M., Melatos A., 2009b, MNRAS, 395, 1985

Wheeler J. C., Yi I., Höflich P., Wang L., 2000, ApJ, 537, 810

Zhang D., Dai Z. G., 2008, ApJ, 683, 329

Zhong S.-Q., Dai Z.-G., Li X.-D., 2019, Phys. Rev. D, 100, 123014

This paper has been typeset from a TEX/LATEX file prepared by the author.

Author contributions statements

Title: "Gravitational waves from mountains in newly born millisecond magnetars"
Authors: Ankan Sur and Brynmor Haskell
Publication: Monthly Notices of the Royal Astronomical Society, Volume 502, Issue 4, pp.4680-4688

Contributions:

Ankan Sur: Developed the idea, performed all calculations, produced figures, and contributed to writing the paper. My total contribution to this article is 80%.

_____
Ankan Sur

Brynmor Haskell: evolved the neutron star models, supervised the project, and contributed to writing the paper. My contribution to this article is 20%.

_____
Brynmor Haskell

Conclusions and Future directions

"However difficult life may seem, there is always something you can do, and succeed at. It matter that you don't just give up"
-Stephen Hawking

Magnetic fields in isolated NSs are responsible for an array of activity from flares on the surface to gamma-ray bursts and fast radio bursts. This thesis examines several magnetic field configurations in isolated NSs and their impact on their evolution.

Chapter 2 investigated the strength of the toroidal field within the star using nonlinear MHD simulations. Two different initial conditions were explored: first, a purely poloidal field; and second, a mixed poloidal-toroidal field with a stronger toroidal component initially. Our fiducial NS was modeled with a barotropic equation of state where $P \propto \rho^2$. We observed that a purely poloidal initial field is unstable and our final magnetic field, after 40 ms of evolution, emerged in pseudo-equilibrium forming a 'twisted torus' geometry with the toroidal component having a small fraction of the total magnetic energy. The stronger toroidal field setup after 40 ms settled to a configuration contributing 10-20% to the total magnetic energy. These configurations, however, were not in strict-equilibrium, since the instability caused turbulence, which led to the development of an inverse cascade of magnetic helicity. Therefore, the final field configuration was determined by the non-linear saturation of the instability, rather than being stationary. The average energy of the poloidal and toroidal components remained relatively stable in our simulations, and a complex multipolar structure emerged at the NS surface, while the magnetic field at the outer boundary is dipolar.

To better understand the field geometry at late times, long-term GRMHD simulations were performed in chapter 3 using the code Athena++ evolving the magnetic field up to 880 ms with increased computational resolution. Two main issues were addressed in this study when comparing different initial conditions in chapter 2. First, the toroidal vs poloidal dominated simulations behaved differently. The stronger toroidal setup developed a significant poloidal component with 20% energy, but this poloidal field did not become the dominant component at the end of the simulation. On the other hand, the purely poloidal setup did not develop such a large toroidal component. No evidence of equilibrium was found in the final field configuration and the toroidal field was reduced to 1 % of the total magnetic energy. This is likely due to the outflow boundary conditions implemented in this work when compared to a fixed boundary in chapter 2. In the interior of the star, more than 90% of the magnetic energy was converted to heat. Our models consisted of a fluid star without the presence of solid crystalline crust. Even though some magnetic flux escapes as Poything flux and is radiated away, a more realistic model is needed to better understand electromagnetic emission from NSs. The growth times of various azimuthal oscillation modes were also calculated. They have important implications for astroseismology and the study of GW radiation from isolated NSs. Additionally, based on our MHD simulations in chapter 2, the hypothesis that turbulence plays a significant role in quasi equilibrium was explored. An analysis of the spectra in our higher resolution setups revealed that in most cases we do not see turbulence at small scales, but rather a noisy velocity field inside the star. However, this needs to be studied in greater detail to fully understand whether turbulence plays an important role in the evolution of magnetic field to its quasi-stationary

state.

Our results on the magnetic field are only applicable to a period just after the birth of NSs. In the initial collapse of a massive star, the core is opaque to neutrinos and is not in chemical equilibrium. As the star cools, however, all the neutrinos escape and the star essentially loses all its entropy and reaches equilibrium. It will be interesting to perform simulations at times when the crust has formed and include the effects of stratification, and find out how it influences the evolution of the toroidal field which otherwise has the effect of floating within the star because of buoyancy. This would require an understanding of when, after the birth of the PNS, stratification becomes relevant. It is also important to observe the effects of rotation on the magnetic field which may affect the growth of internal modes and the toroidal field. Further, an investigation of whether dynamos operate following the birth of PNSs will be intriguing.

While the aforementioned results come from time-evolving systems, equilibrium solutions from the Grad-Shafranov equation were obtained for a normal matter crust in Hall/MHD equilibrium and a superconducting core NS. A new algorithm was presented in in chapter 4 to solve the nonlinear Grad-Shafranov equation based on the Gauss-Siedel method and linearizing the source term which improved stability and convergence of our solutions. Our results indicated that the toroidal field is confined in the crust, accounting for 5% of the total magnetic energy. These models are applicable for the standard pulsar population in which we can use them as a background for more realistic vortex pinning calculations and understand pulsar glitch phenomenona. Magnetic deformations in the NS crust were also measured by calculating the ellipticity, which turned out to be 10^{-11} for an average B field strength of 10^{12} G. A higher ellipticity corresponds to a stronger GW amplitude emitted by a rotating NS. Thus, we conclude that an axisymmetric magnetic field in equilibrium does not deform the NS sufficiently for the current generation of detectors to observe GWs from pulsars.

Lastly, chapter 5 presented a scenario in which a newly born millisecond magnetar forms accretion columns at its magnetic poles. This allows the magnetar to possess a large quadrupole moment and emit GWs. We examined the spin evolution of the magnetar under the influence of accretion torque, dipole radiation, neutrino wind, and GWs. In the early stages, the spin period is mostly affected by dipole radiation, but later on, accretion causes the star to spin up rapidly. A magnetar formed after the collapse of a massive star can accrete up to 1 $M_\odot$ before collapsing to a black hole on the order of 50 s. For an object at 1 Mpc, the GW strain is $h_c \sim 10^{-23}$ at kHz frequencies, which makes it a good candidate for next-generation ground-based detectors. On the other hand, a magnetar formed by a binary neutron star merger accretes at most 0.2 $M_\odot$ and emits GWs with a strain of $h_c \sim 10^{-24}$. Such a magnetar may survive for much longer times, and may possibly be associated with the X-ray plateau that has been observed in the light curves of short gamma-ray bursts.

Calculating braking indices (n) of radio pulsars is an important tool to conclude whether

the external field is growing ($n < 3$) or decaying ($n > 3$). There are few sources observed, for e.g. PSR 1734-3333 and PSR B0540-69 with $n \sim 0.9$ which would likely move up the $P - \dot{P}$ diagram and end up in the magnetar regime. On a timescale of $10^3 \sim 10^4$ years, fallback accretion is capable of burying NS magnetic fields which then starts diffusing out. Due to this process, the star's external magnetic field can increase and it may start to operate as a radio-pulsar. Due the typical behavior of these sources, it will be interesting to study how the external magnetic field grows and whether fall-back accretion plays a role.

Studying the evolution of the magnetic field requires precise measurements of the current field structure and value. By modeling pulse profiles of magnetars and millisecond pulsars, information about the field topology can be obtained; in rare cases, phase-resolved spectroscopy can provide this information. [CM11a; CM11b] used Stokes tomography to constrain the magnetic field of ordinary pulsars that subsequently turned out to be dipolar. A useful tool for probing the structure of NS magnetospheres are polarisation measurements. In this regard, the rotating vector model (RVM) [RC69] plays a pivotal role in pulsar theory. It gives the position angle (PA) of the electric field as a function of the pulse phase (ϕ) and shows that the plane of linear polarization sweeps a characteristic S-shaped swing over a single pulse period. This is a characteristic of dipolar magnetic field in the external magnetosphere of ordinary pulsars. Although the RVM model successfully explains pulse profiles of many pulsars qualitatively (e.g. [MTH75]), observations of millisecond pulsars show flat, distorted, or even random PA profiles hinting towards non-dipolar configurations [Gen+18]. Thus, accurately modeling the radio polarisation with a multipolar magnetic field, e.g. for the pulsar PSR J0031, can constrain its magnetic field geometry.

Along with Yajie Yuan and Alexander Philippov, I have obtained preliminary results on reproducing the polarisation of the millisecond pulsar PSR J0030 with a multipolar force-free magnetospheric solution. It allowed us to constrain the height from which the radio emission is produced. This work is still under progress and is not part of this thesis.

Algorithm for numerically solving the TOV equation

```python
import numpy as np
import pylab
from scipy.integrate import odeint
from matplotlib import pyplot as plt
from scipy.constants import pi, G, c, hbar, m_n

#define various constants
Msun = 1.98892e30 #solar mass
gamma = 1.663#power law index 1#1.663
#gamma = np.linspace(1.5,1.68,10)
K = (3.0*pi**2)**(2.0/3.0)*hbar**2/(5.0*m_n**(8.0/3.0)) #constant K in eos
gamma1 = [3.4] #power law index 2 #3.4
#gamma1 = [2.65] #power law index 2 #3.4
#gamma1 = np.linspace(2.,3.,5)
rho1 = 4.5e17 #critical density #4.5e17
#rho1 = np.linspace(1e17,1e18,10)
Rmax = 20000
n = 10000


#get pressure from density using EOS
def eos(rho, rho1, gamma, gamma1):
    p1 = K*rho1**gamma
    K1 = p1/rho1**gamma1
    if rho < rho1: return K*rho**gamma
    else: return K1*rho**gamma1

#get density from pressure inverting EOS
def inveos(p, rho1, gamma, gamma1):
    p1 = K*rho1**gamma
    K1 = p1/rho1**gamma1
    if p < p1: return (p/K)**(1.0/gamma)
    else: return (p/K1)**(1./gamma1)

def tov_p(p,m,r,rho):
    dpdr = -G*(rho + p/c**2)*(m + 4.0*pi*r**3*p/c**2)
    dpdr = dpdr/(r*(r-2.0*G*m/c**2))
    return dpdr

def tov_m(r, rho):
    dmdr =   4.0*pi*r**2*rho
    return dmdr

#solve the TOV equation using Euler forward method
def tovsolve_eul1(rho_c, r, m, p, rho1, gamma, gamma1):
    i = 0
    m[0] = 4.0*pi*r[0]**3*rho_c/3.
```

```
    p[0] = eos(rho_c, rho1, gamma, gamma1)
    while p[i] > 0.0 and i < len(r)-1:
        dr = r[i+1]-r[i]
        rho = inveos(p[i], rho1, gamma, gamma1)
        dpdr = -G*(rho + p[i]/c**2)*(m[i] + 4.0*pi*r[i]**3*p[i]/c**2)
        dpdr = dpdr/(r[i]*(r[i]-2.0*G*m[i]/c**2))
        dmdr = 4.0*pi*r[i]**2*rho
        p[i+1] = p[i] + dr*dpdr
        m[i+1] = m[i] + dr*dmdr
        i = i+1
    return m, p, r

#solve the TOV equation Runge-Kutta 2 method
def tovsolve_rk2(rho_c, r, m, p, rho1, gamma, gamma1):
    i = 0
    m[0] = 4.0*pi*r[0]**3*rho_c/3.
    p[0] = eos(rho_c, rho1, gamma, gamma1)
    rho_r = []
    while p[i] > 0.0 and i < len(r)-1:
        dr = r[i+1]-r[i]
        rho = inveos(p[i], rho1, gamma, gamma1)
        rho_r.append(rho)
        dpdr = tov_p(p[i],m[i],r[i],rho)
        dmdr = tov_m(r[i],rho)
        p_b = p[i] + dr*dpdr
        m_b = m[i] + dr*dmdr
        p[i+1] = p[i] + dr*(dpdr + tov_p(p_b, m[i], r[i+1],rho))/2.
        m[i+1] = m[i] + dr*(dmdr + tov_m(r[i+1],rho))/2.
        i = i+1
    return m, p, r, np.array(rho_r)


#function to plot the MASS_RADIUS Curve
def plots(rho1, gamma, gamma1):
    I_r = []
    rhoc = pylab.logspace(17.0,20.,1000) # logspace range of central densities
    for j in range(len(gamma1)):
        M, R = [], []
        for i in range(len(rhoc)):
            r = np.linspace(10.0,Rmax,n)
            m = np.zeros(n)
            p = np.zeros(n)
            mass, press, rad, den = tovsolve_rk2(rhoc[i], r, m, p, rho1, gamma, gamma1[j])
            #mass, press, rad = tovsolve_eul1(rhoc[i], r, m, p, rho1, gamma, gamma1[j])
            indx = np.where(press>0)
            mass = mass[indx]
            rad = rad[indx]
            den = den[indx]
```

```
            M. append ( mass [ −1]/Msun)
            R. append ( rad [ −1]/1000.)
            #if  i >30:
            I_r . append (np. trapz ( rad ∗∗4∗den , x=rad )∗8∗np. pi /3.0/ mass[ −1]/ rad [ −1]∗∗2)
        plt . plot (R, M,  label ="$\Gamma_0=$"+ s t r ( round (gamma , 2 ) )  + \
        " ,$\Gamma_1=$"+ s t r ( round (gamma1[ j ] , 2 ) ) )
    np. savetxt ( ' Mass_test . txt ' ,M)
    np. savetxt ( ' Rad_test . txt ' ,R)
    #np. savetxt ( ' txt ' )
    plt . xlabel ( ' Radius R(km) ' ,  size =15)
    plt . ylabel ( r 'Mass M($\rm M_\odot$ ) ' ,  size =15)
    plt . axhline (1.4 ,  c= 'black ' ,  linestyle = '−−')
    plt . legend ( loc = 'best ' )
    plt . grid ()
    plt . show ()
    return  np. array ( I_r )

Ir  =  plots ( rho1 ,  gamma ,  gamma1)
```

Bibliography

[Abb+17a]   B. P. Abbott et al. "A gravitational-wave standard siren measurement of the Hubble constant". In: *Nature* 551.7678 (2017), pp. 85–88. DOI: 10.1038/nature24471. arXiv: 1710.05835 [astro-ph.CO].

[Abb+17b]   B. P. Abbott et al. "Estimating the Contribution of Dynamical Ejecta in the Kilonova Associated with GW170817". In: *Astrophys. J. Lett.* 850.2 (2017), p. L39. DOI: 10.3847/2041-8213/aa9478. arXiv: 1710.05836 [astro-ph.HE].

[Abb+21a]   B. P. Abbott et al. "A Gravitational-wave Measurement of the Hubble Constant Following the Second Observing Run of Advanced LIGO and Virgo". In: *Astrophys. J.* 909.2 (2021). [Erratum: Astrophys.J. 923, 279 (2021)], p. 218. DOI: 10.3847/1538-4357/abdcb7. arXiv: 1908.06060 [astro-ph.CO].

[Abb+21b]   R. Abbott et al. "All-sky search in early O3 LIGO data for continuous gravitational-wave signals from unknown neutron stars in binary systems". In: *Phys. Rev. D* 103.6 (2021), p. 064017. DOI: 10.1103/PhysRevD.103.064017. arXiv: 2012.12128 [gr-qc].

[Abb+21c]   R. Abbott et al. "Diving below the spin-down limit: Constraints on gravitational waves from the energetic young pulsar PSR J0537-6910". In: *Astrophys. J.* 913 (2021), p. L27. DOI: 10.3847/2041-8213/abffcd. arXiv: 2012.12926 [astro-ph.HE].

[Abb+21d]   R. Abbott et al. "Population Properties of Compact Objects from the Second LIGO-Virgo Gravitational-Wave Transient Catalog". In: *Astrophys. J. Lett.* 913.1 (2021), p. L7. DOI: 10.3847/2041-8213/abe949. arXiv: 2010.14533 [astro-ph.HE].

[Abb+21e]   R. Abbott et al. "Search for continuous gravitational waves from 20 accreting millisecond X-ray pulsars in O3 LIGO data". In: (Sept. 2021). arXiv: 2109.09255 [astro-ph.HE].

[Abb+21f]   R. Abbott et al. "Search of the Early O3 LIGO Data for Continuous Gravitational Waves from the Cassiopeia A and Vela Jr. Supernova Remnants". In: (Nov. 2021). arXiv: 2111.15116 [gr-qc].

[Abb+21g]   R. Abbott et al. "Searches for Continuous Gravitational Waves from Young Super-nova Remnants in the Early Third Observing Run of Advanced LIGO and Virgo". In: *Astrophys. J.* 921.1 (2021), p. 80. DOI: 10.3847/1538-4357/ac17ea. arXiv: 2105. 11641 [astro-ph.HE].

[Abb+21h]   R. Abbott et al. "Tests of General Relativity with GWTC-3". In: (Dec. 2021). arXiv: 2112.06861 [gr-qc].

[Abb+22]   R. Abbott et al. "All-sky search for continuous gravitational waves from isolated neutron stars using Advanced LIGO and Advanced Virgo O3 data". In: (Jan. 2022). arXiv: 2201.00697 [gr-qc].

[Akg+13]   T. Akgün et al. "Stability of magnetic fields in non-barotropic stars: an analytic treatment". In: 433.3 (Aug. 2013), pp. 2445–2466. DOI: 10.1093/mnras/stt913. arXiv: 1302.0273 [astro-ph.SR].

[Ant+06]   Luis Antón et al. "Numerical 3+1 General Relativistic Magnetohydrodynamics: A Local Characteristic Approach". In: 637.1 (Jan. 2006), pp. 296–312. DOI: 10.1086/498238. arXiv: astro-ph/0506063 [astro-ph].

[Ant+13]   John Antoniadis et al. "A Massive Pulsar in a Compact Relativistic Binary". In: *Science* 340.6131 (Apr. 2013), p. 448. DOI: 10.1126/science.1233232. arXiv: 1304. 6875 [astro-ph.HE].

[Arc+16]   R. F. Archibald et al. "A High Braking Index for a Pulsar". In: 819.1, L16 (Mar. 2016), p. L16. DOI: 10.3847/2041-8205/819/1/L16. arXiv: 1603.00305 [astro-ph.HE].

[Aro98]   J. Arons. "General Relativistic Polar Particle Acceleration and Pulsar Death". In: *Neutron Stars and Pulsars: Thirty Years after the Discovery*. Ed. by N. Shibazaki. Jan. 1998, p. 339. arXiv: astro-ph/9802198 [astro-ph].

[Aru+18]   Prakash Arumugasamy et al. "Possible Phase-dependent Absorption Feature in the X-Ray Spectrum of the Middle-aged PSR J0659+1414". In: 869.2, 97 (Dec. 2018), p. 97. DOI: 10.3847/1538-4357/aaec69. arXiv: 1810.11814 [astro-ph.HE].

[BG96]   S. Bonazzola and E. Gourgoulhon. "Gravitational waves from pulsars: emission by the magnetic-field-induced distortion." In: 312 (Aug. 1996), pp. 675–690. arXiv: astro-ph/9602107 [astro-ph].

[Bha+05]   Sudip Bhattacharyya et al. "Constraints on Neutron Star Parameters from Burst Oscillation Light Curves of the Accreting Millisecond Pulsar XTE J1814-338". In: 619.1 (Jan. 2005), pp. 483–491. DOI: 10.1086/426383. arXiv: astro-ph/0402534 [astro-ph].

[Bil+19]   A. V. Bilous et al. "A NICER View of PSR J0030+0451: Evidence for a Global-scale Multipolar Magnetic Field". In: 887.1, L23 (2019), p. L23. DOI: 10.3847/2041-8213/ab53e7. arXiv: 1912.05704 [astro-ph.HE].

[Bil98]   Lars Bildsten. "Gravitational Radiation and Rotation of Accreting Neutron Stars". In: 501.1 (July 1998), pp. L89–L93. DOI: 10.1086/311440. arXiv: astro-ph/9804325 [astro-ph].

[Bog13]   Slavko Bogdanov. "The Nearest Millisecond Pulsar Revisited with XMM-Newton: Improved Mass-radius Constraints for PSR J0437-4715". In: 762.2, 96 (Jan. 2013), p. 96. DOI: 10.1088/0004-637X/762/2/96. arXiv: 1211.6113 [astro-ph.HE].

[BPP69]   Gordon Baym, Christopher Pethick, and David Pines. "Superfluidity in Neutron Stars". In: 224.5220 (Nov. 1969), pp. 673–674. DOI: 10.1038/224673a0.

[Bra07]   J. Braithwaite. "The stability of poloidal magnetic fields in rotating stars". In: *Astron. Astrophys.* 469 (2007), p. 275. DOI: 10.1051/0004-6361:20065903. arXiv: 0705.0185 [astro-ph].

[Bra08]   Jonathan Braithwaite. "On non-axisymmetric magnetic equilibria in stars". In: 386.4 (2008), pp. 1947–1958. DOI: 10.1111/j.1365-2966.2008.13218.x. arXiv: 0803.1661 [astro-ph].

[Bra09]   Jonathan Braithwaite. "Axisymmetric magnetic fields in stars: relative strengths of poloidal and toroidal components". In: 397.2 (Aug. 2009), pp. 763–774. DOI: 10.1111/j.1365-2966.2008.14034.x. arXiv: 0810.1049 [astro-ph].

[BS06]   Jonathan Braithwaite and H. C. Spruit. "Evolution of the magnetic field in magnetars". In: *Astron. Astrophys.* 450 (2006), p. 1097. DOI: 10.1051/0004-6361:20041981. arXiv: astro-ph/0510287 [astro-ph].

[Bv91]   D. Bhattacharya and E. P. J. van den Heuvel. "Formation and evolution of binary and millisecond radio pulsars". In: 203.1-2 (Jan. 1991), pp. 1–124. DOI: 10.1016/0370-1573(91)90064-S.

[Cac+08]   Edward M. Cackett et al. "Cooling of the Crust in the Neutron Star Low-Mass X-Ray Binary MXB 1659-29". In: 687.2 (Nov. 2008), p. L87. DOI: 10.1086/593703. arXiv: 0806.1166 [astro-ph].

[CF53]   S. Chandrasekhar and E. Fermi. "Problems of Gravitational Stability in the Presence of a Magnetic Field." In: 118 (July 1953), p. 116. DOI: 10.1086/145732.

[CFG10]   R. Ciolfi, V. Ferrari, and L. Gualtieri. "Structure and deformations of strongly magnetized neutron stars with twisted torus configurations". In: *Mon. Not. Roy. Astron. Soc.* 406 (2010), pp. 2540–2548. DOI: 10.1111/j.1365-2966.2010.16847.x. arXiv: 1003.2148 [astro-ph.SR].

[Cha56]   S. Chandrasekhar. "Axisymmetric Magnetic Fields and Fluid Motions." In: 124 (July 1956), p. 232. DOI: 10.1086/146217.

[Cio+09]   R. Ciolfi et al. "Relativistic models of magnetars: the twisted torus magnetic field configuration". In: 397.2 (Aug. 2009), pp. 913–924. DOI: 10.1111/j.1365-2966.2009.14990.x. arXiv: 0903.0556 [astro-ph.SR].

[Cio+11]   Riccardo Ciolfi et al. "Instability-driven evolution of poloidal magnetic fields in relativistic stars". In: *Astrophys. J.* 736 (2011), p. L6. DOI: 10.1088/2041-8205/736/1/L6. arXiv: 1105.3971 [gr-qc].

[CM11a]   C. T. Y. Chung and A. Melatos. "Stokes tomography of radio pulsar magneto-spheres - I. Linear polarization". In: 411.4 (2011), pp. 2471–2529. DOI: 10.1111/j.1365-2966.2010.17858.x. arXiv: 1010.2816 [astro-ph.SR].

[CM11b]   C. T. Y. Chung and A. Melatos. "Stokes tomography of radio pulsar magneto-spheres - II. Millisecond pulsars". In: 415.2 (2011), pp. 1703–1737. DOI: 10.1111/j.1365-2966.2011.18815.x. arXiv: 1104.1016 [astro-ph.SR].

[CR12]   Riccardo Ciolfi and Luciano Rezzolla. "Poloidal-field Instability in Magnetized Relativistic Stars". In: 760.1, 1 (2012), p. 1. DOI: 10.1088/0004-637X/760/1/1. arXiv: 1206.6604 [astro-ph.SR].

[Cro+20] H. T. Cromartie et al. "Relativistic Shapiro delay measurements of an extremely massive millisecond pulsar". In: *Nature Astronomy* 4 (Jan. 2020), pp. 72–76. DOI: 10.1038/s41550-019-0880-2. arXiv: 1904.06759 [astro-ph.HE].

[CVF21]   Hsin-Yu Chen, Salvatore Vitale, and Francois Foucart. "The Relative Contribution to Heavy Metals Production from Binary Neutron Star Mergers and Neutron Star-Black Hole Mergers". In: 920.1, L3 (Oct. 2021), p. L3. DOI: 10.3847/2041-8213/ac26c6. arXiv: 2107.02714 [astro-ph.HE].

[Dem+10] P. B. Demorest et al. "A two-solar-mass neutron star measured using Shapiro delay". In: 467.7319 (Oct. 2010), pp. 1081–1083. DOI: 10.1038/nature09466. arXiv: 1010.5788 [astro-ph.HE].

[DT92]   Robert C. Duncan and Christopher Thompson. "Formation of Very Strongly Magnetized Neutron Stars: Implications for Gamma-Ray Bursts". In: 392 (June 1992), p. L9. DOI: 10.1086/186413.

[GA11]   Kostas Glampedakis and Nils Andersson. "Magneto-rotational Neutron Star Evolution: The Role of Core Vortex Pinning". In: 740.2, L35 (Oct. 2011), p. L35. DOI: 10.1088/2041-8205/740/2/L35. arXiv: 1106.5997 [astro-ph.SR].

[GAS11]   Kostas Glampedakis, Nils Andersson, and Lars Samuelsson. "Magnetohydrodynamics of superfluid and superconducting neutron star cores". In: 410.2 (Jan. 2011), pp. 805–829. DOI: 10.1111/j.1365-2966.2010.17484.x. arXiv: 1001.4046 [astro-ph.SR].

[GC14a]   K. N. Gourgouliatos and A. Cumming. "Hall effect in neutron star crusts: evolution, endpoint and dependence on initial conditions". In: 438.2 (2014), pp. 1618–1629. DOI: 10.1093/mnras/stt2300. arXiv: 1311.7004 [astro-ph.SR].

[GC14b]   Konstantinos N. Gourgouliatos and Andrew Cumming. "Hall Attractor in Axially Symmetric Magnetic Fields in Neutron Star Crusts". In: 112.17, 171101 (May 2014), p. 171101. DOI: 10.1103/PhysRevLett.112.171101. arXiv: 1311.7345 [astro-ph.SR].

[GDI22]   Konstantinos N. Gourgouliatos, Davide De Grandis, and Andrei Igoshev. "Magnetic Field Evolution in Neutron Star Crusts: Beyond the Hall Effect". In: *Symmetry* 14.1 (Jan. 2022), p. 130. DOI: 10.3390/sym14010130. arXiv: 2201.08345 [astro-ph.HE].

[Gen+18]   Peter A. Gentile et al. "The NANOGrav 11 yr Data Set: Arecibo Observatory Polarimetry and Pulse Microcomponents". In: 862.1, 47 (July 2018), p. 47. DOI: 10.3847/1538-4357/aac9c9. arXiv: 1807.00708 [astro-ph.HE].

[GMG03]   J. Gil, G. I. Melikidze, and U. Geppert. "Drifting subpulses and inner accelerationregions in radio pulsars". In: 407 (Aug. 2003), pp. 315–324. DOI: 10.1051/0004-6361:20030854. arXiv: astro-ph/0305463 [astro-ph].

[GMT03]   Charles F. Gammie, Jonathan C. McKinney, and Gábor Tóth. "HARM: A Numerical Scheme for General Relativistic Magnetohydrodynamics". In: 589.1 (May 2003), pp. 444–457. DOI: 10.1086/374594. arXiv: astro-ph/0301509 [astro-ph].

[Gou+13]   K. N. Gourgouliatos et al. "Hall equilibria with toroidal and poloidal fields: application to neutron stars". In: 434.3 (Sept. 2013), pp. 2480–2490. DOI: 10.1093/mnras/stt1195. arXiv: 1305.6269 [astro-ph.SR].

[GP19]   K. N. Gourgouliatos and José A. Pons. "Nonaxisymmetric Hall instability: A key to understanding magnetars". In: *Physical Review Research* 1.3, 032049 (Dec. 2019), p. 032049. DOI: 10.1103/PhysRevResearch.1.032049.

[GR02]   U. Geppert and M. Rheinhardt. "Non-linear magnetic field decay in neutron stars. Theory and observations". In: 392 (Sept. 2002), pp. 1015–1024. DOI: 10.1051/0004-6361:20020978. arXiv: astro-ph/0207065 [astro-ph].

[GR92]   Peter Goldreich and Andreas Reisenegger. "Magnetic Field Decay in Isolated Neutron Stars". In: 395 (Aug. 1992), p. 250. DOI: 10.1086/171646.

[Gra+15]   Vanessa Graber et al. "Magnetic field evolution in superconducting neutron stars". In: 453.1 (Oct. 2015), pp. 671–681. DOI: 10.1093/mnras/stv1648. arXiv: 1505.00124 [astro-ph.SR].

[GU94]   U. Geppert and V. Urpin. "Accretion-driven magnetic field decay in neutron stars". In: 271 (Nov. 1994), p. 490. DOI: 10.1093/mnras/271.2.490.

[Har+97]   J. W. Hartman et al. "A study of the evolution of radio pulsars through improved population synthesis." In: 322 (June 1997), pp. 477–488.

[Has+08]   B. Haskell et al. "Modelling magnetically deformed neutron stars". In: 385.1 (Mar. 2008), pp. 531–542. DOI: 10.1111/j.1365-2966.2008.12861.x. arXiv: 0705.1780 [astro-ph].

[Heg+03]   Alexander Heger et al. "Massive Star Evolution Through the Ages". In: *From Twilight to Highlight: The Physics of Supernovae*. Ed. by Wolfgang Hillebrandt and Bruno Leibundgut. Jan. 2003, p. 3. DOI: 10.1007/10828549_1. arXiv: astro-ph/0211062 [astro-ph].

[HL06]   Alice K. Harding and Dong Lai. "Physics of strongly magnetized neutron stars". In: *Reports on Progress in Physics* 69.9 (Sept. 2006), pp. 2631–2708. DOI: 10.1088/0034-4885/69/9/R03. arXiv: astro-ph/0606674 [astro-ph].

[HM01]   Alice K. Harding and Alexander G. Muslimov. "Pulsar Polar Cap Heating and Surface Thermal X-Ray Emission. I. Curvature Radiation Pair Fronts". In: 556.2 (Aug. 2001), pp. 987–1001. DOI: 10.1086/321589. arXiv: astro-ph/0104146 [astro-ph].

[HM15]   Brynmor Haskell and Andrew Melatos. "Models of pulsar glitches". In: *International Journal of Modern Physics D* 24.3, 1530008 (Jan. 2015), p. 1530008. DOI: 10.1142/S0218271815300086. arXiv: 1502.07062 [astro-ph.SR].

[Ho+14]   Wynn C. G. Ho et al. "Equilibrium spin pulsars unite neutron star populations". In: *Monthly Notices of the Royal Astronomical Society* 437 (2014), pp. 3664–3669.

[HPY07]   P. Haensel, A. Y. Potekhin, and D. G. Yakovlev. *Neutron Stars 1 : Equation of State and Structure*. Vol. 326. 2007.

[HS18]   Brynmor Haskell and Armen Sedrakian. "Superfluidity and Superconductivity in Neutron Stars". In: *Astrophysics and Space Science Library*. Ed. by Luciano Rezzolla et al. Vol. 457. 2018, p. 401. DOI: 10.1007/978-3-319-97616-7_8.

[in'+02]   J. J. M. in't Zand et al. "Discovery of the neutron star nature of SLX 1737-282". In: 389 (July 2002), pp. L43–L46. DOI: 10.1051/0004-6361:20020631. arXiv: astro-ph/0204433 [astro-ph].

[IPH21]   Andrei P. Igoshev, Sergei B. Popov, and Rainer Hollerbach. "Evolution of Neutron Star Magnetic Fields". In: *Universe* 7.9 (Sept. 2021), p. 351. DOI: 10.3390/universe7090351. arXiv: 2109.05584 [astro-ph.HE].

[JG99]   Simon Johnston and David Galloway. "Pulsar braking indices revisited". In: 306.4 (July 1999), pp. L50–L54. DOI: 10.1046/j.1365-8711.1999.02737.x. arXiv: astro-ph/9905058 [astro-ph].

[Jon80]   P. B. Jones. "Pair formation and electric field boundary conditions at neutron star magnetic poles". In: 192 (Sept. 1980), pp. 847–860. DOI: 10.1093/mnras/192.4.847.

[KB97]   Sushan Konar and Dipankar Bhattacharya. "Magnetic field evolution of accreting neutron stars". In: 284.2 (Jan. 1997), pp. 311–317. DOI: 10.1093/mnras/284.2.311.

[KB99]   Sushan Konar and Dipankar Bhattacharya. "Magnetic field evolution of accreting neutron stars - II". In: 303.3 (Mar. 1999), pp. 588–594. DOI: 10.1046/j.1365-8711.1999.02287.x. arXiv: astro-ph/9808119 [astro-ph].

[KG01]   D. Konenkov and U. Geppert. "The evolution of the core and surface magnetic fields in isolated neutron stars". In: 325.1 (July 2001), pp. 426–434. DOI: 10.1046/j.1365-8711.2001.04469.x. arXiv: astro-ph/0103060 [astro-ph].

[KK12]   Yasufumi Kojima and Shota Kisaka. "Magnetic field decay with Hall drift in neutron star crusts". In: 421.3 (Apr. 2012), pp. 2722–2730. DOI: 10.1111/j.1365-2966.2012.20509.x. arXiv: 1201.1346 [astro-ph.HE].

[Kom05] S. S. Komissarov. "Observations of the Blandford-Znajek process and the magnetohydrodynamic Penrose process in computer simulations of black hole magnetospheres". In: 359.3 (May 2005), pp. 801–808. DOI: 10.1111/j.1365-2966.2005.08974.x. arXiv: astro-ph/0501599 [astro-ph].

[KSK99] Shinji Koide, Kazunari Shibata, and Takahiro Kudoh. "Relativistic Jet Formation from Black Hole Magnetized Accretion Disks: Method, Tests, and Applications of a General RelativisticMagnetohydrodynamic Numerical Code". In: 522.2 (Sept. 1999), pp. 727–752. DOI: 10.1086/307667.

[Las+11] Paul D. Lasky et al. "Hydromagnetic Instabilities in Neutron Stars". In: *Astrophys. J.* 735 (2011), p. L20. DOI: 10.1088/2041-8205/735/1/L20. arXiv: 1105.1895 [astro-ph.SR].

[Las15] Paul D. Lasky. "Gravitational Waves from Neutron Stars: A Review". In: 32, e034 (Sept. 2015), e034. DOI: 10.1017/pasa.2015.35. arXiv: 1508.06643 [astro-ph.HE].

[Leg08] Anthony James Leggett. *Quantum Liquids: Bose condensation and Cooper pairing in condensed-matter systems*. English (US). Vol. 9780198526438. Publisher Copyright: © Oxford University Press, 2014. United Kingdom: Oxford University Press, Jan. 2008. ISBN: 9780198526438. DOI: 10.1093/acprof:oso/9780198526438.001.0001.

[Lyn+15] A. G. Lyne et al. "45 years of rotation of the Crab pulsar". In: 446.1 (Jan. 2015), pp. 857–864. DOI: 10.1093/mnras/stu2118. arXiv: 1410.0886 [astro-ph.HE].

[Lyn+96] A. G. Lyne et al. "Very low braking index for the Vela pulsar". In: 381.6582 (June 1996), pp. 497–498. DOI: 10.1038/381497a0.

[Man+05] R. N. Manchester et al. "The Australia Telescope National Facility Pulsar Catalogue". In: 129.4 (Apr. 2005), pp. 1993–2006. DOI: 10.1086/428488. arXiv: astro-ph/0412641 [astro-ph].

[Mar+14] Pablo Marchant et al. "Stability of Hall Equilibria in Neutron Star Crusts". In: 796.2, 94 (Dec. 2014), p. 94. DOI: 10.1088/0004-637X/796/2/94. arXiv: 1410.5833 [astro-ph.HE].

[Mas+11] A. Mastrano et al. "Gravitational wave emission from a magnetically deformed non-barotropic neutron star". In: 417.3 (Nov. 2011), pp. 2288–2299. DOI: 10.1111/j.1365-2966.2011.19410.x. arXiv: 1108.0219 [astro-ph.HE].

[Mil+19] M. C. Miller et al. "PSR J0030+0451 Mass and Radius from NICER Data and Implications for the Properties of Neutron Star Matter". In: 887.1, L24 (2019), p. L24. DOI: 10.3847/2041-8213/ab50c5. arXiv: 1912.05705 [astro-ph.HE].

[MM17] Ben Margalit and Brian D. Metzger. "Constraining the Maximum Mass of Neutron Stars from Multi-messenger Observations of GW170817". In: 850.2, L19 (Dec. 2017), p. L19. DOI: 10.3847/2041-8213/aa991c. arXiv: 1710.05938 [astro-ph.HE].

[MTH75] R. N. Manchester, J. H. Taylor, and G. R. Huguenin. "Observations of pulsar radio emission. II. Polarization of individual pulses." In: 196 (Feb. 1975), pp. 83–102. DOI: 10.1086/153395.

[New13]   William G. Newton. "Neutron stars: A taste of pasta?" In: *Nature Physics* 9.7 (July 2013), pp. 396–397. DOI: 10.1038/nphys2663.

[Oer+17]   M. Oertel et al. "Equations of state for supernovae and compact stars". In: *Reviews of Modern Physics* 89.1, 015007 (Jan. 2017), p. 015007. DOI: 10.1103/RevModPhys.89.015007. arXiv: 1610.03361 [astro-ph.HE].

[PCC19]   A. Y. Potekhin, A. I. Chugunov, and G. Chabrier. "Thermal evolution and quiescent emission of transiently accreting neutron stars". In: 629, A88 (Sept. 2019), A88. DOI: 10.1051/0004-6361/201936003. arXiv: 1907.08299 [astro-ph.HE].

[PG07]   J. A. Pons and U. Geppert. "Magnetic field dissipation in neutron star crusts: from magnetars to isolated neutron stars". In: 470.1 (July 2007), pp. 303–315. DOI: 10.1051/0004-6361:20077456. arXiv: astro-ph/0703267 [astro-ph].

[PG10]   J. A. Pons and U. Geppert. "Confirmation of the occurrence of the Hall instability in the non-linear regime". In: 513, L12 (Apr. 2010), p. L12. DOI: 10.1051/0004-6361/201014197. arXiv: 1004.1054 [astro-ph.SR].

[Pon+07]   José A. Pons et al. "Evidence for Heating of Neutron Stars by Magnetic-Field Decay". In: 98.7, 071101 (Feb. 2007), p. 071101. DOI: 10.1103/PhysRevLett.98.071101. arXiv: astro-ph/0607583 [astro-ph].

[Raa+21]   G. Raaijmakers et al. "Constraints on the Dense Matter Equation of State and Neutron Star Properties from NICER's Mass-Radius Estimate of PSR J0740+6620 and Multimessenger Observations". In: 918.2, L29 (Sept. 2021), p. L29. DOI: 10.3847/2041-8213/ac089a. arXiv: 2105.06981 [astro-ph.HE].

[RC69]   V. Radhakrishnan and D. J. Cooke. "Magnetic Poles and the Polarization Structure of Pulsar Radiation". In: 3 (Jan. 1969), p. 225.

[Rei+07]   A. Reisenegger et al. "Hall drift of axisymmetric magnetic fields in solid neutron-star matter". In: 472.1 (Sept. 2007), pp. 233–240. DOI: 10.1051/0004-6361:20077874. arXiv: 0705.1901 [astro-ph].

[Rei14]   Andreas Reisenegger. "Hydromagnetic Equilibria and their Evolution in Neutron Stars". In: *Magnetic Fields throughout Stellar Evolution*. Ed. by Pascal Petit, Moira Jardine, and Hendrik C. Spruit. Vol. 302. Aug. 2014, pp. 404–414. DOI: 10.1017/S1743921314002622.

[Ril+19]   T. E. Riley et al. "A NICER View of PSR J0030+0451: Millisecond Pulsar Parameter Estimation". In: 887.1, L21 (2019), p. L21. DOI: 10.3847/2041-8213/ab481c. arXiv: 1912.05702 [astro-ph.HE].

[RMW18]   Luciano Rezzolla, Elias R. Most, and Lukas R. Weih. "Using Gravitational-wave Observations and Quasi-universal Relations to Constrain the Maximum Mass of Neutron Stars". In: 852.2, L25 (Jan. 2018), p. L25. DOI: 10.3847/2041-8213/aaa401. arXiv: 1711.00314 [astro-ph.HE].

[SB19] Magdalena Sieniawska and Michał Bejger. "Continuous Gravitational Waves from Neutron Stars: Current Status and Prospects". In: *Universe* 5.11 (Oct. 2019), p. 217. DOI: 10.3390/universe5110217. arXiv: 1909.12600 [astro-ph.HE].

[Spi06] Anatoly Spitkovsky. "Time-dependent force-free pulsar magnetospheres: axisymmetric and oblique rotators". In: *Astrophys. J. Lett.* 648 (2006), pp. L51–L54. DOI: 10.1086/507518. arXiv: astro-ph/0603147.

[ST86] Stuart L. Shapiro and Saul A. Teukolsky. *Black Holes, White Dwarfs and Neutron Stars: The Physics of Compact Objects*. 1986.

[TD93] Christopher Thompson and Robert C. Duncan. "Neutron Star Dynamos and the Origins of Pulsar Magnetism". In: 408 (1993), p. 194. DOI: 10.1086/172580.

[TD95] Christopher Thompson and Robert C. Duncan. "The soft gamma repeaters as very strongly magnetized neutron stars - I. Radiative mechanism for outbursts". In: 275.2 (July 1995), pp. 255–300. DOI: 10.1093/mnras/275.2.255.

[UCB00] Greg Ushomirsky, Curt Cutler, and Lars Bildsten. "Deformations of accreting neutron star crusts and gravitational wave emission". In: 319.3 (Dec. 2000), pp. 902–932. DOI: 10.1046/j.1365-8711.2000.03938.x. arXiv: astro-ph/0001136 [astro-ph].

[WH09] C. J. Wareing and R. Hollerbach. "Hall cascades versus instabilities in neutron star magnetic fields". In: 508.3 (Dec. 2009), pp. L39–L42. DOI: 10.1051/0004-6361/200913452. arXiv: 0912.2656 [astro-ph.HE].

[WT06] P. M. Woods and C. Thompson. "Soft gamma repeaters and anomalous X-ray pulsars: magnetar candidates". In: *Compact stellar X-ray sources*. Vol. 39. 2006, pp. 547–586.